NASA/CR—1998-208679

Nonlinear Interaction of Detuned Instability Waves in Boundary–Layer Transition

Amplitude Equations

Sang Soo Lee
Dynacs Engineering Company, Inc., Brook Park, Ohio

October 1998

The NASA STI Program Office . . . in Profile

Since its founding, NASA has been dedicated to the advancement of aeronautics and space science. The NASA Scientific and Technical Information (STI) Program Office plays a key part in helping NASA maintain this important role.

The NASA STI Program Office is operated by Langley Research Center, the Lead Center for NASA's scientific and technical information. The NASA STI Program Office provides access to the NASA STI Database, the largest collection of aeronautical and space science STI in the world. The Program Office is also NASA's institutional mechanism for disseminating the results of its research and development activities. These results are published by NASA in the NASA STI Report Series, which includes the following report types:

- TECHNICAL PUBLICATION. Reports of completed research or a major significant phase of research that present the results of NASA programs and include extensive data or theoretical analysis. Includes compilations of significant scientific and technical data and information deemed to be of continuing reference value. NASA's counterpart of peer-reviewed formal professional papers but has less stringent limitations on manuscript length and extent of graphic presentations.

- TECHNICAL MEMORANDUM. Scientific and technical findings that are preliminary or of specialized interest, e.g., quick release reports, working papers, and bibliographies that contain minimal annotation. Does not contain extensive analysis.

- CONTRACTOR REPORT. Scientific and technical findings by NASA-sponsored contractors and grantees.

- CONFERENCE PUBLICATION. Collected papers from scientific and technical conferences, symposia, seminars, or other meetings sponsored or cosponsored by NASA.

- SPECIAL PUBLICATION. Scientific, technical, or historical information from NASA programs, projects, and missions, often concerned with subjects having substantial public interest.

- TECHNICAL TRANSLATION. English-language translations of foreign scientific and technical material pertinent to NASA's mission.

Specialized services that complement the STI Program Office's diverse offerings include creating custom thesauri, building customized data bases, organizing and publishing research results . . . even providing videos.

For more information about the NASA STI Program Office, see the following:

- Access the NASA STI Program Home Page at ***http://www.sti.nasa.gov***

- E-mail your question via the Internet to help@sti.nasa.gov

- Fax your question to the NASA Access Help Desk at (301) 621-0134

- Telephone the NASA Access Help Desk at (301) 621-0390

- Write to:
  NASA Access Help Desk
  NASA Center for AeroSpace Information
  7121 Standard Drive
  Hanover, MD 21076

NASA/CR—1998-208679

Nonlinear Interaction of Detuned Instability Waves in Boundary–Layer Transition

Amplitude Equations

Sang Soo Lee
Dynacs Engineering Company, Inc., Brook Park, Ohio

Prepared under Contract NAS3–98008

National Aeronautics and
Space Administration

Lewis Research Center

October 1998

Available from

NASA Center for Aerospace Information
7121 Standard Drive
Hanover, MD 21076
Price Code: A05

National Technical Information Service
5285 Port Royal Road
Springfield, VA 22100
Price Code: A05

NONLINEAR INTERACTION OF DETUNED INSTABILITY WAVES IN BOUNDARY-LAYER TRANSITION: 2. AMPLITUDE EQUATIONS

Sang Soo Lee

Dynacs Engineering Co., Inc., NASA Lewis Research Center Group

2001 Aerospace Parkway, Brook Park, OH 44142

Abstract

The non-equilibrium critical-layer analysis of a system of frequency-detuned resonant-triads is presented. In this part of the analysis, the system of partial differential critical-layer equations derived in Part 1 is solved analytically to yield the amplitude equations which are analyzed using a combination of asymptotic and numerical methods. Numerical solutions of the inviscid non-equilibrium oblique-mode amplitude equations show that the frequency-detuned self-interaction enhances the growth of the lower-frequency oblique modes more than the higher-frequency ones. All amplitudes become singular at the same finite downstream position. The frequency detuning delays the occurrence of the singularity. The spanwise-periodic mean-flow distortion and low-frequency nonlinear modes are generated by the critical-layer interaction between frequency-detuned oblique modes. The nonlinear mean flow and higher harmonics as well as the primary instabilities become as large as the base mean flow in the inviscid wall layer in the downstream region where the distance from the singularity is of the order of the wavelength scale.

1. Introduction and summary of Part 1

The non-equilibrium critical-layer analysis of a system of frequency-detuned resonant-triads in boundary layers with and without mean pressure gradient was obtained in Part 1 (Lee 1998b) [1] . Each resonant-triad is composed of a fundamental plane wave and a pair of subharmonic oblique modes. It is shown that the resonant-triads can nonlinearly interact within the common critical layer when their frequencies are different by a factor whose magnitude is of the order of the growth rates multiplied by the wavenumbers.

If the (fundamental) frequencies of the resonant-triads are sufficiently detuned, the plane and oblique modes of each resonant-triad first nonlinearly interact between themselves. Their growth is not affected by the existence of the other resonant-triads and the growth rates are increased due to the parametric-resonance and self-interaction effects (of a single resonant-triad interaction as shown by Goldstein & Lee 1992). The frequency-detuned resonant-triads start to interact between themselves at the downstream position where the instability growth rates become large enough to be equal to the magnitude of the phase speed differences (of the plane waves). Eventually, as the magnitude of the growth rates approaches that of the wavenumbers, most of the unstable waves whose scaled Strouhal numbers are different by nearly $O(1)$ can nonlinearly interact. In this downstream region, the frequency range in which the resonant-triads can nonlinearly interact expands to cover the entire range of linearly unstable waves.

The results of experimental study by Corke & Gruber (1996) (an extensive survey on

[1] t appeared in parentheses in the last term in (3.1) of Part 1 must be replaced by t_1, $i\bar{\mu}_{cj}Y_{cj}$ in front of the square brackets in (5.6) of Part 1 must be replaced by iY_{cj}, and $\tilde{A}_0^{(0)}$ in (7.60) of Part 1 must be replaced by $\tilde{A}_j^{(0)}$.

resonant-triad interaction can be found in Kachanov 1994) and direct numerical simulations by Liu & Maslowe (1998) in Falkner-Skan boundary layers are in good agreement with the resonant-triad theory of Goldstein & Lee (1992). The parametric-resonance-, self- and mutual-interactions and back-reaction are identified and shown to play major role in the transition process, especially in the adverse-pressure-gradient boundary layer.

The system of partial differential critical-layer equations can be solved both analytically (Goldstein & Choi 1989; Goldstein & Lee 1992, 1993; Wu 1992, 1995; Wu, Lee & Cowley 1993) and numerically (Lee 1997a). In this part of the study, the system of critical-layer equations given in §7 of Part 1 will be solved analytically and the amplitude equations (without the back-reaction term in the plane-wave amplitude equation) will be presented along with numerical solutions. The analytical solutions of the critical-layer equations are obtained in §2. The frequency-detuned non-equilibrium amplitude equations are presented in §3 and their large frequency-detuning limit and asymptotic singular solutions are given in §4 and §5, respectively. The viscous limit of the amplitude equations is obtained in §6. The velocity jumps across the critical layer for the nonlinearly-generated low-frequency modes are given in §7. Numerical solutions of the frequency-detuned quasi-equilibrium (i.e. viscous-limit) amplitude equations are presented in §8. The frequency-detuned non-equilibrium amplitude equations of the oblique modes are numerically solved in §9. The concluding remarks are given in §10.

In the rest of this section we will give a brief summary of Part 1 to allow the reader to follow along without consulting Part 1 too often.

In the non-equilibrium critical layer the mean convection effect balances with the growth and viscous effects. If we introduce the wavenumber parameter σ and the local-

growth-rate parameter σ^r to characterize the small wavenumber and the ratio of the small local growth rate to the wavenumber, respectively, the generalized scaling of Lee (1997a) can be written as (see also (I.2.2) – (I.2.4) where henceforth an I at the beginning of an equation number will indicate an equation given in Part 1), for $-J \leqslant \jmath \leqslant J$,

$$\alpha_\jmath = \sigma[\bar{\alpha}_\jmath + O(\sigma^r)], \quad \ddot{c}_\jmath = \sigma[\bar{\ddot{c}}_\jmath + O(\sigma^r)], \quad c_\jmath = \sigma[\bar{c}_\jmath + O(\sigma^r)], \quad \beta_\jmath = \sigma\bar{\beta}_\jmath, \quad y_{c\jmath} = \sigma Y_{c\jmath}, \tag{1.1}$$

$$x_1 = \sigma^{r+1} x, \tag{1.2}$$

$$\mu = \sigma^{r-1}\bar{\mu} \quad \text{for} \quad 1 \leqslant r \leqslant 3 \quad \text{and} \quad \mu = O(1) \quad \text{for} \quad 0 < r \leqslant 1, \tag{1.3}$$

where $\ddot{c}_\jmath$ and $c_\jmath$ are the (nearly equal) phase velocities of the two-dimensional and oblique modes respectively, $\alpha_\jmath$ is the streamwise wavenumber of the plane wave, $\beta_\jmath$ represents the spanwise wavenumber of the oblique mode, $y_{c\jmath}$ is the critical level where the base mean-flow velocity is equal to the real part of the phase velocity, $\bar{\alpha}_\jmath$, $\bar{\ddot{c}}_\jmath$, $\bar{\beta}_\jmath$ and $Y_{c\jmath}$ are order-one real constants and μ is the normalized mean pressure gradient. The subscript $\jmath$ is used to denote the quantities of the $\jmath$th resonant triad. However, the subscript 0 for the quantities of the 'reference' 0th resonant-triad will be omitted for notational simplicity.

The local-growth-rate exponent r is a function of the streamwise coordinate since the instability growth rates are varying. The frequency-detuned non-equilibrium analysis of this paper is valid for any value of r. Each analysis for a specific value of r covers different stage of the non-equilibrium critical-layer evolution (see table 1 of Lee 1997a). A composite solution could be obtained to cover a series of nonlinear stages.

The $\jmath$th resonant triad is composed of a single two-dimensional mode and a pair of subharmonic oblique modes. The phase speed of the plane wave is assumed to be nearly equal to that of the oblique modes of the same resonant-triad. This resonance condition is

satisfied when the propagation angle of the oblique mode θ defined as (also as (I.5.29))

$$\theta \equiv \cos^{-1}\left(\tfrac{1}{2}\bar{\alpha}/\bar{\gamma}\right) \tag{1.4}$$

is about $\pi/3$.

The nondimensional frequency or unscaled Strouhal number $s_\jmath$ of the fundamental two-dimensional mode of the $\jmath$th resonant-triad is equal to $\alpha_\jmath \bar{c}_\jmath$ and the scaled Strouhal number $\bar{s}_\jmath$ is given by (also by (I.2.5))

$$s_\jmath = \sigma^2 \bar{s}_\jmath = \sigma^2 \bar{\alpha}_\jmath \bar{c}_\jmath. \tag{1.5}$$

The difference between the scaled Strouhal numbers of the $\jmath$th and the 'reference' 0th resonant-triads is given by (also by (I.2.6)) (Lee 1997b, 1998a)

$$\bar{s}_\jmath = \bar{s}(1 + \sigma^r \jmath\chi) \quad \text{or} \quad s_\jmath = s(1 + \jmath\hat{\chi}) \quad \text{for} \quad -J \leqslant \jmath \leqslant J, \tag{1.6}$$

where

$$\hat{\chi} = \sigma^r \chi. \tag{1.7}$$

It was shown by (I.5.22) that the scaled phase velocity of the $\jmath$th resonant-triad, $\bar{c}_\jmath$ is different from that of the 0th resonant-triad, $\bar{c}$ by $O(\sigma^r)$, which is the additional resonance condition that is required for the nonlinear interaction between the frequency-detuned resonant-triads to occur in the common critical layer.

In the non-equilibrium critical-layer analysis, the Reynolds number is scaled as (also as (I.2.8))

$$\lambda \equiv 1/(\sigma^{3r+4} R_\Delta), \tag{1.8}$$

and the amplitudes are scaled as (also as (I.2.9)), for all $\jmath$,

$$\epsilon_{2d} = \sigma^{4r+1}, \quad \delta_{3d} = \delta_{02} = \sigma^{3r+1}, \tag{1.9}$$

where ϵ_{2d}, δ_{3d} and δ_{02} are the amplitude scalings of the plane wave, oblique modes and nonlinearly-generated low-frequency (spanwise-periodic) modes.

The scalings given above are for the long-wavelength small-growth-rate instabilities in boundary layers, for example, in the high-Reynolds-number adverse-pressure-gradient boundary layer or in the downstream non-equilibrium stage of the Blasius boundary layer. Their frequencies are of the order of the wavenumber scaling squared and their critical layers are distinct from the viscous wall layer.

The multi-layer structure for the non-equilibrium critical-layer analysis was given in figure 1 of Part 1. The unsteady flows in the main boundary layer ($y = O(1)$), the inviscid wall layer ($y = O(\sigma)$), and the viscous Stokes layer [2] ($y = O(\sigma^{3r/2+1})$) are governed by linear dynamics. The viscous Stokes-layer effect was included in order to make the analysis valid in the viscous limit. The solutions in the inviscid wall layer become singular at the critical level, therefore, they have to be rescaled in the critical layer. The nonlinear interaction between instability waves of the frequency-detuned resonant-triads first occurs within the common critical layer whose thickness is of $O(\sigma^{r+1})$.

The streamwise velocity in the main boundary layer is given by (also by (I.3.1)) (Lee 1997b, 1998a)

$$u = U + \epsilon_{2d} \sum_{j=-J}^{J} \mathrm{Re}\tilde{B}_j(x_1)\ddot{\Phi}_{jy}(y, x_1)e^{\mathrm{i}X_j} + \delta_{3d} \sum_{j=-J}^{J} \mathrm{Re}2\tilde{A}_j(x_1)\tilde{U}_j(y, x_1)e^{\mathrm{i}X_j/2}\cos Z_j + \delta_{02} \sum_{j} \sum_{\ell} \mathrm{Re}\bar{U}_{0,2;j,\ell}(y, x_1, z, t_1) + \ldots, \qquad (1.10)$$

where

$$X_j \equiv \sigma\bar{\alpha}_j x - \sigma^2 \bar{s}_j t, \quad Z_j \equiv \sigma\bar{\beta}_j z, \qquad (1.11)$$

[2] $y = O(\sigma^{3r/2+1}\lambda^{1/2})$ when $\lambda \ll 1$.

U is the base mean flow velocity, $\tilde{A}_j$ and $\tilde{B}_j$ denote the oblique and plane wave amplitudes, respectively, and t_1 is defined by (I.5.24).

The jump equations are obtained from the requirement that the velocity jumps across the critical layer which are calculated from the critical-layer solutions are equal to those calculated from the external solutions. They must be solved with the system of critical-layer equations to determine the unknown instability amplitudes.

The system of partial differential critical-layer equations along with the transverse boundary conditions and the jump equations are presented in §7 of Part 1. They are normalized in such a way that their nonlinear growth parts are free from any mean-flow-dependent parameter apart from λ. The normalized variables in the critical-layer equations that are relevant to this part of the paper are, as in (I.3.19), (I.5.26) and (I.7.1) – (I.7.4),

$$\bar{x} = \hat{\kappa}\left(\tfrac{1}{2}\tau_w\bar{\alpha}x_1 - x_o\right), \quad \bar{\lambda} = \frac{2\lambda}{\hat{\kappa}^3\tau_w\bar{\alpha}\bar{c}^3}, \quad \bar{\chi} = \frac{1}{\hat{\kappa}\tau_w}\chi, \quad \bar{a}_{1M}^{(2)} = \frac{\pi Y_c\bar{\alpha}}{\hat{\kappa}\tau_w^3\bar{c}}\left[\bar{\mu} - \sigma^{3-r}\left(\tfrac{1}{2}\tau_o Y_c\right)^2\right], \tag{1.12}$$

$$A_j/\mathcal{D}_{1;j}(\bar{x}) \equiv \frac{(Y_cM)^{1/2}}{\hat{\kappa}^3\bar{c}}e^{\mathrm{i}j\tilde{\chi}\bar{\alpha}x_1/4}\tilde{A}_j, \quad B_j/\mathcal{D}_{2;2j}(\bar{x}) \equiv \frac{M}{\hat{\kappa}^4}e^{\mathrm{i}j\tilde{\chi}\bar{\alpha}x_1/2}\tilde{B}_j, \tag{1.13}$$

where $M \equiv 8\pi Y_c\bar{\beta}^2/(\tau_w^3\bar{\alpha}\bar{c}^3)$ as defined by (I.7.5), $\mathcal{D}_{a;j}(\bar{x}) \equiv \exp\left[\frac{1}{2}\mathrm{i}a\left(X_o + \eta_o\bar{x}\right) - \mathrm{i}j\bar{\chi}\bar{x}\right]$ as given by (I.7.6), $\hat{\kappa}$ is a normalization parameter which can be chosen arbitrarily, x_o, X_o and η_o are the coordinate origin shifts (see (I.7.58) and (I.7.62)), τ_o is the scaled Blasius skin friction, τ_w denotes the total wall-shear stress (that is the sum of the Blasius skin friction and the correction due to the mean pressure gradient) as in (I.3.15) and (I.3.16) and $\tilde{\chi} = \chi + O(\sigma)$ as in (I.5.23).

2. Solutions of the critical-layer equations

The analytical solutions of the partial differential critical-layer equations given in §7 of Part 1 will be obtained in this section.

As in the previous studies (Wu *et al.* 1993; Goldstein & Lee 1993; Wu 1995; Lee 1997a), the Fourier transform with respect to η will be used,

$$\hat{Q}(\bar{x},k)=\int_{-\infty}^{\infty}e^{-ik\eta}Q(\bar{x},\eta)d\eta,\quad Q(\bar{x},\eta)=\frac{1}{2\pi}\int_{-\infty}^{\infty}e^{ik\eta}\hat{Q}(\bar{x},k)dk, \tag{2.1}$$

where $\hat{Q}=\mathcal{F}\{Q\}$ is the Fourier transform of Q. The velocity jump across the critical layer can be obtained from the Fourier transform by putting $k=0$,

$$\hat{Q}(\bar{x},k=0)=\int_{-\infty}^{\infty}Q(\bar{x},\eta)d\eta. \tag{2.2}$$

In order to simplify the presentation we will put

$$\zeta_1\equiv\bar{x}-x_1,\quad \zeta_2\equiv x_1-x_2,\quad h_s\equiv\tau\sin^2\theta, \tag{2.3}$$

and

$$\bar{\mathcal{E}}_m^{\pm}(\zeta_1;\zeta_2)\equiv\exp\left[\pm\bar{\lambda}\left(\tfrac{1}{3}m\zeta_1+\zeta_2\right)\zeta_1^2\right]. \tag{2.4}$$

2.1. *The leading-order equation*

The solution of (I.7.8) which satisfies the transverse boundary condition (I.7.9) can be obtained by taking the Fourier transform of (I.7.8), solving the resulting equation and then taking the inverse Fourier transform of $\hat{Q}_j^{(1)}(\bar{x},k)$. The solution is

$$Q_j^{(1)}=e^{-i\bar{x}\eta}I_{0j}(\bar{x},\eta), \tag{2.5}$$

where

$$I_{nj}(\bar{x},\eta)\equiv\int_{-\infty}^{\bar{x}}dx_1e^{i\eta x_1}\bar{\mathcal{E}}_1^{-}(\zeta_1;0)\zeta_1^nA_j(x_1). \tag{2.6}$$

2.2. *The second-order equations*

In order to simplify the presentation we will only show the Fourier transforms of the solutions of (I.7.10), (I.7.11) and (I.7.14) which satisfy the boundary conditions (I.7.20) and (I.7.21). They are

$$\mathcal{F}\left\{W^{(2)}_{0,0;j}\right\}(\bar{x},k) = -\mathrm{i}\pi \sum_{\ell:-1} \int_{-\infty}^{\bar{x}} dx_1 \mathcal{J}_{j,\ell}(\bar{x},x_1,k), \tag{2.7}$$

$$\mathcal{F}\left\{W^{(2)}_{0,2;j,\ell}, U^{(2)}_{0,2;j,\ell\eta}\right\}(\bar{x},k) = \pi \int_{-\infty}^{\bar{x}} dx_1 \left\{\mathrm{i}, -(2\zeta_1 + k)\right\} \left[\mathcal{J}_{j,\ell}(\bar{x},x_1,k) + \mathcal{K}_{j,\ell}(\bar{x},x_1,k)\right], \tag{2.8}$$

$$\mathcal{F}\left\{W^{(2)}_{2,0;j,\ell}, U^{(2)}_{2,0;j,\ell\eta}\right\}(\bar{x},k) = \tfrac{1}{2}\pi e^{\bar{\lambda}k^3/6} \int_k^{\infty} d\tilde{k} \left\{-\mathrm{i}, \tilde{k}\right\} \Big[e^{\bar{\lambda}\tilde{k}^3/6} \tilde{k} H(-\tilde{k}) A_{j-\ell}(\hat{x}_a) A_\ell(\hat{x}_a + \tilde{k})$$
$$-2h_s e^{-\bar{\lambda}\tilde{k}^3/6} \int_{-\infty}^{\infty} dk_1 \int_{-\infty}^{\infty} dk_2 \mathcal{G}_a^-(\tilde{k}) A_{j-\ell}(\hat{x}_a + k_1) A_\ell(\hat{x}_a + k_2)\Big], \tag{2.9}$$

where

$$\mathcal{J}_{j,\ell}(\bar{x},x_1,k) \equiv \tilde{\mathcal{E}}^+_{-1}(k;-\zeta_1) k H(k) A_{j+\ell}(x_1) A^*_\ell(x_1 - k), \tag{2.10}$$

$$\mathcal{K}_{j,\ell}(\bar{x},x_1,k) \equiv 2h_s \tilde{\mathcal{E}}^-_0(k;\zeta_1) \int_{-\infty}^{\infty} dk_1 \int_{-\infty}^{\infty} dk_2 \mathcal{G}^+_a(k) A_{j+\ell}(x_1 + k_1) A^*_\ell(x_1 + k_2), \tag{2.11}$$

$$\mathcal{G}^{\pm}_a(k) \equiv e^{\bar{\lambda}(k_1^3 + k_2^3)/3} H(-k_1) H(-k_2) \delta(k - k_1 \pm k_2), \tag{2.12}$$

$$\hat{x}_a \equiv \bar{x} + (k - \tilde{k})/2, \tag{2.13}$$

the summation notation is defined in (I.6.20) and the asterisk denotes the complex conjugate. The step function $H(k)$ is defined by (Butkov 1968)

$$H(k) = 1 \ \text{ if } \ k > 0; \quad H(k) = 1/2 \ \text{ if } \ k = 0; \quad H(k) = 0 \ \text{ if } \ k < 0, \tag{2.14}$$

and $\delta(k)$ is the delta function (Lighthill 1960; Butkov 1968).

2.3. *The third-order equations for the oblique-mode velocity jump*

In order to obtain the velocity jump across the critical layer for the oblique modes, we need to solve the equations (I.7.22) – (I.7.30) (but only the second part which involves $V^{(n)}_{1,1;\jmath[,\ell,m]}$) with the boundary conditions (I.7.34).

The linear growth term in the oblique-mode amplitude equation can be obtained by solving (I.7.22),

$$\mathcal{F}\left\{V^{(3L)}_{1,1;\jmath\eta\eta}\right\}(\bar{x},k) = 4\mathrm{i}\pi\bar{a}^{(2)}_{1M}e^{\bar{\lambda}k^3/3}H(-k)A_\jmath(\bar{x}+k)\,, \tag{2.15}$$

and the linear velocity jump becomes, by putting $k=0$ (see (2.2)),

$$\mathcal{F}\left\{V^{(3L)}_{1,1;\jmath\eta\eta}\right\}(\bar{x},k=0)\left[=\int_{-\infty}^{\infty}V^{(3L)}_{1,1;\jmath\eta\eta}d\eta\right] = 2\mathrm{i}\pi\bar{a}^{(2)}_{1M}A_\jmath(\bar{x}). \tag{2.16}$$

Using (2.5) and (I.7.13) we can show that the solution of (I.7.23) becomes

$$\mathcal{F}\left\{V^{(3a)}_{1,1;\jmath,\ell\eta\eta}\right\}(\bar{x},k) = -4\pi(\cos^2\theta)\int_k^{\infty}d\tilde{k}e^{\bar{\lambda}(k^3-2\tilde{k}^3)/3}\tilde{k}^2H(\tilde{k})B_\ell(\bar{x}+k-\tilde{k})A^*_{\ell-\jmath}(\bar{x}+k-2\tilde{k}), \tag{2.17}$$

and the velocity jump for the parametric-resonance term is

$$\mathcal{F}\left\{V^{(3a)}_{1,1;\jmath,\ell\eta\eta}\right\}(\bar{x},k=0) = -4\pi(\cos^2\theta)\int_{-\infty}^{\bar{x}}dx_1\tilde{\mathcal{E}}_2^-(\zeta_1;0)\zeta_1^2B_\ell(x_1)A^*_{\ell-\jmath}(2x_1-\bar{x}). \tag{2.18}$$

The nonlinear part of the oblique-mode velocity jump is obtained by solving (I.7.24) to (I.7.30). It is easy to show from (I.7.24) and (I.7.29) that

$$\mathcal{F}\left\{V^{(3b)}_{1,1;\jmath\eta\eta}\right\}(\bar{x},k=0) = \mathcal{F}\left\{V^{(3g)}_{1,1;\jmath,\ell\eta\eta}\right\}(\bar{x},k=0) = 0. \tag{2.19}$$

The solution of (I.7.25) can be obtained by using (2.7) and (I.7.10),

$$\mathcal{F}\left\{V^{(3c)}_{1,1;\jmath,\ell\eta\eta}\right\}(\bar{x},k=0) = \pi\sum_{m:-1}\int_{-\infty}^{\bar{x}}dx_1\int_{-\infty}^{x_1}dx_2K^{(3c)}A_{\jmath-\ell}(x_1)A_{\ell+m}(x_2)A^*_m(x_1+x_2-\bar{x}), \tag{2.20}$$

where

$$K^{(3c)} = \tilde{\mathcal{E}}_2^-(\zeta_1;\zeta_2)\zeta_1^3. \tag{2.21}$$

From (I.7.26) along with (2.5), (2.8) and (I.7.11), we can show that

$$\mathcal{F}\left\{V^{(3d)}_{1,1;j,\ell,m\eta\eta}\right\}(\bar{x},k=0) = \pi\int_{-\infty}^{\bar{x}} dx_1 \int_{-\infty}^{x_1} dx_2 K_I^{(3d)} A_{j-\ell}(x_1)A_{\ell+m}(x_2)A_m^*(x_1+x_2-\bar{x}) + \hat{\mathcal{V}}^{(3d)}, \tag{2.22}$$

where

$$K_I^{(3d)} = \tilde{\mathcal{E}}_2^-(\zeta_1;\zeta_2)\zeta_1\left[(\zeta_1+\zeta_2)\zeta_1 + 2h_s\int_0^{\zeta_2} d\zeta_3 \tilde{\mathcal{E}}_2^-(\zeta_3;\zeta_1)(\zeta_1+\zeta_2-\zeta_3)\right], \tag{2.23}$$

$$\hat{\mathcal{V}}^{(3d)} = -\int_{-\infty}^{\bar{x}} dx_1 \int_{-\infty}^{x_1} dx_2 \int_{-\infty}^{\infty} d\eta \int_{-\infty}^{\infty} dk_3 g_b^- \left[\mathcal{J}_{\ell,m}(x_1,x_2,k_3) + \mathcal{K}_{\ell,m}(x_1,x_2,k_3)\right], \tag{2.24}$$

$$g_b^{\pm} \equiv h_s e^{-\mathrm{i}(\bar{x}\pm k_3)\eta}\tilde{\mathcal{E}}_1^-(\zeta_1;0)\frac{\zeta_1}{k_3}\left[(k_3+2\zeta_2)I_{0(j\pm\ell)}(x_1,\eta) + I_{1(j\pm\ell)}(x_1,\eta)\right], \tag{2.25}$$

with (2.6), (2.10) and (2.11). Integrating by parts and changing the order of integrations using

$$\int_{-\infty}^{\bar{x}} dx_1 \int_{-\infty}^{x_1} dx_2 = \int_{-\infty}^{\bar{x}} dx_2 \int_{x_2}^{\bar{x}} dx_1, \tag{2.26}$$

(2.24) can be rewritten as

$$\hat{\mathcal{V}}^{(3d)} = -2\pi h_s \int_{-\infty}^{\bar{x}} dx_1 \int_{-\infty}^{x_1} dx_2 \left[K_{IIa}^{(3d)} A_{\ell+m}(x_1)A_{j-\ell}(x_2)A_m^*(x_1+x_2-\bar{x}) + K_{IIb}^{(3d)} A_{j-\ell}(x_1)A_{\ell+m}(x_2)A_m^*(x_1+x_2-\bar{x})\right], \tag{2.27}$$

where

$$K_{IIa}^{(3d)} = \mathcal{G}_c(\zeta_1,0,0;1) + \mathcal{G}_d^+(\zeta_1,0,0;1), \quad K_{IIb}^{(3d)} = \mathcal{G}_c(\zeta_1,\zeta_2,0;1) + \mathcal{G}_d^+(\zeta_1,\zeta_2,0;1), \tag{2.28}$$

$$\mathcal{G}_c(\zeta_a,\zeta_b,\zeta_c;\hat{a}) \equiv \int_0^{\zeta_1} d\zeta_3 g_e\left\{\hat{a}\hat{\xi}_a\left[\zeta_a+2\zeta_2+3(\zeta_3-\zeta_c)\right] + \left(1+2\bar{\lambda}\hat{\xi}_a\hat{\xi}_b^2\right)\zeta_2\zeta_c\right\}, \tag{2.29}$$

$$\mathcal{G}_d^{\pm}(\zeta_a,\zeta_b,\zeta_c;\hat{a}) \equiv 2h_s \int_0^{\zeta_1} d\zeta_3 g_e \int_0^{\zeta_b+\zeta_3} d\zeta_4 \left\{ \hat{a}\tilde{\mathcal{E}}_2^{\mp}(\hat{\xi}_c;\hat{\xi}_d)\hat{\xi}_a + \tilde{\mathcal{E}}_2^{\mp}(\zeta_4;\hat{\xi}_d)\hat{\xi}_c \right.$$
$$\left. \left[1 + 2\bar{\lambda}\hat{\xi}_a(\hat{\xi}_b - \zeta_a - \zeta_b)^2\right]\right\}, \tag{2.30}$$

$$g_e \equiv e^{-\bar{\lambda}\left[\left(\frac{2}{3}\zeta_1+\zeta_2\right)\zeta_1^2+\left(\frac{2}{3}\zeta_2+\zeta_1\right)(\zeta_2-\zeta_b)^2+(\zeta_1+\zeta_2-\zeta_b)(\zeta_3+2\zeta_2-2\zeta_b)\zeta_3+\left(\zeta_1+2\zeta_2+\frac{4}{3}\zeta_3\right)\zeta_e^2\right]}, \tag{2.31}$$

$$\hat{\xi}_a \equiv \zeta_1 - \zeta_3, \quad \hat{\xi}_b \equiv \zeta_1 + \zeta_2 + \zeta_3, \quad \hat{\xi}_c \equiv \zeta_b + \zeta_3 - \zeta_4, \quad \hat{\xi}_d \equiv \zeta_a + \zeta_2 - \zeta_b. \tag{2.32}$$

The solutions of (I.7.27) and (I.7.28) can be given as, using (2.5), (2.9) and (I.7.14),

$$\mathcal{F}\left\{V_{1,1;j,\ell,m\eta\eta}^{(3e,3f)}\right\}(\bar{x},k=0) = \pi \int_{-\infty}^{\bar{x}} dx_1 \int_{-\infty}^{x_1} dx_2 \int_{-\infty}^{x_2} dx_3 e^{-\bar{\lambda}\zeta_1^3/3}\zeta_1 A_m(x_3)$$
$$\left[\zeta_3 \mathcal{G}_f^{\mp}(0;1)A_{\ell-m}(x_2)A_{\ell-j}^*(x_2+x_3-\bar{x}) + 2h_s \int_{-\infty}^{x_2} dx_4 e^{-\bar{\lambda}(\zeta_3^3+\hat{\xi}_e^3)/3}\mathcal{G}_f^{\mp}(\hat{\xi}_e;-1)\right.$$
$$\left. A_{\ell-m}(x_4)A_{\ell-j}^*(x_3+x_4-\bar{x})\right], \tag{2.33}$$

where $\zeta_3 \equiv x_2 - x_3$, $\zeta_4 \equiv x_3 - x_4$, the minus superscript in $\mathcal{G}_f^{\mp}$ is for the $(3e)$ component and the plus one is for the $(3f)$ component and we have put

$$\mathcal{G}_f^{\pm}(\zeta_a;\hat{a}) = 2h_s e^{-\bar{\lambda}\left(\hat{a}\hat{\xi}_f^3+\hat{\xi}_g^3+2\hat{\xi}_h^3\right)/6}\left(\hat{\xi}_f\hat{\xi}_h\hat{\xi}_g^{-2} \pm 1\right), \tag{2.34}$$

$$\hat{\xi}_e \equiv \zeta_3 + \zeta_4, \quad \hat{\xi}_f \equiv \zeta_3 + \zeta_a, \quad \hat{\xi}_g \equiv \hat{\xi}_f + 2\zeta_2, \quad \hat{\xi}_h \equiv \hat{\xi}_g + \zeta_1. \tag{2.35}$$

Using (2.26) and integrating by parts, (2.33) can be rewritten as

$$\mathcal{F}\left\{V_{1,1;j,\ell,m\eta\eta}^{(3e,3f)}\right\}(\bar{x},k=0) = 2\pi h_s \int_{-\infty}^{\bar{x}} dx_1 \int_{-\infty}^{x_1} dx_2 \left[K_a^{(3e,3f)}A_m(x_1)A_{\ell-m}(x_2)\right.$$
$$\left. A_{\ell-j}^*(x_1+x_2-\bar{x}) + K_b^{(3e,3f)}A_{\ell-m}(x_1)A_m(x_2)A_{\ell-j}^*(x_1+x_2-\bar{x})\right], \tag{2.36}$$

where

$$K_a^{(3e,3f)} = 2h_s \int_0^{\zeta_1} d\zeta_3 \int_0^{\zeta_3} d\zeta_4 g_g \left[\tilde{\mathcal{E}}_2^{+}(\zeta_4;\zeta_2)(\zeta_3-\zeta_4)\left(1 + 2\bar{\lambda}\hat{\xi}_a\hat{\xi}_b^2\right) \mp \tilde{\mathcal{E}}_2^{+}(\zeta_3-\zeta_4;\zeta_2)\hat{\xi}_a\right], \tag{2.37}$$

$$K_b^{(3e,3f)} = K_a^{(3e,3f)} + \int_0^{\zeta_1} d\zeta_3 g_g \left[\zeta_2\zeta_3\left(1 + 2\bar{\lambda}\hat{\xi}_a\hat{\xi}_b^2\right) \mp \hat{\xi}_a\zeta_2\right], \tag{2.38}$$

$$g_g \equiv e^{-2\bar{\lambda}(\zeta_1+\zeta_2)\zeta_2\zeta_3}\tilde{\mathcal{E}}_2^-(\zeta_1;\zeta_2)\tilde{\mathcal{E}}_2^-(\zeta_2;\zeta_1)\tilde{\mathcal{E}}_4^-(\zeta_3;2\zeta_1+3\zeta_2), \tag{2.39}$$

the $(-)$ and $(+)$ signs of $(\mp)$ in (2.37) and (2.38) are for the (3e) and (3f) components, respectively, and $\hat{\xi}_a$ and $\hat{\xi}_b$ are defined in (2.32).

We can write the velocity jump obtained from (I.7.30), along with (2.5), (2.8) and (I.7.11), as

$$\mathcal{F}\left\{V^{(3h)}_{1,1;j,\ell,m\eta\eta}\right\}(\bar{x}, k=0) = 2\pi h_s \int_{-\infty}^{\bar{x}} dx_1 \int_{-\infty}^{x_1} dx_2 K_I^{(3h)} A_{j+\ell}(x_1) A_m(x_2) A^*_{\ell+m}(x_1+x_2-\bar{x}) + \hat{\mathcal{V}}^{(3h)}, \tag{2.40}$$

where

$$K_I^{(3h)} = \tilde{\mathcal{E}}_2^-(\zeta_1;\zeta_2)\int_0^{\zeta_2} d\zeta_3 \tilde{\mathcal{E}}_2^-(\zeta_3;\zeta_1)\zeta_1(\zeta_2-\zeta_3), \tag{2.41}$$

$$\hat{\mathcal{V}}^{(3h)} = \int_{-\infty}^{\bar{x}} dx_1 \int_{-\infty}^{x_1} dx_2 \int_{-\infty}^{\infty} d\eta \int_{-\infty}^{\infty} dk_3 g_b^+ \mathcal{K}^*_{\ell,m}(x_1,x_2,k_3), \tag{2.42}$$

and $\mathcal{K}_{\ell,m}$ and g_b^+ are defined in (2.11) and (2.25). The above equation (2.42) can be rewritten as, using (2.26) and integrating by parts,

$$\hat{\mathcal{V}}^{(3h)} = -2\pi h_s \int_{-\infty}^{\bar{x}} dx_1 \int_{-\infty}^{x_1} dx_2 \left[K_{IIa}^{(3h)} A_m(x_1) A_{j+\ell}(x_2) A^*_{\ell+m}(x_1+x_2-\bar{x}) + K_{IIb}^{(3h)} A_{j+\ell}(x_1) A_m(x_2) A^*_{\ell+m}(x_1+x_2-\bar{x})\right], \tag{2.43}$$

where

$$K_{IIa}^{(3h)} = \mathcal{G}_d^+(\zeta_1,0,0;-1), \quad K_{IIb}^{(3h)} = \mathcal{G}_d^+(\zeta_1,\zeta_2,0;-1), \tag{2.44}$$

and $\mathcal{G}_d^+$ is defined in (2.30).

2.4. *Other third-order equations*

In order to obtain the mutual-interaction term in the plane-wave amplitude equation, we need to know the following solutions of the other third-order equations.

The solution of the first part of (I.7.23), along with (2.5) and (I.7.13), which satisfies the boundary condition (I.7.34) becomes

$$\mathcal{F}\left\{W^{(3a)}_{1,1;\jmath,\ell}\right\}(\bar{x},k) = -2\pi e^{\bar{\lambda}k^3/3}\left[P^{(3a)}_{1,1;\jmath,\ell}(\bar{x}+k)H(-k) - \mathrm{i}(\cos^2\theta)\int_k^\infty d\tilde{k}e^{-2\bar{\lambda}\tilde{k}^3/3}\tilde{k}H(\tilde{k})\right.$$
$$\left. B_\ell(\bar{x}+k-\tilde{k})A^*_{\ell-\jmath}(\bar{x}+k-2\tilde{k})\right]. \quad (2.45)$$

Equation (I.7.37) subject to (I.7.43) is solved with (2.5) and (I.7.13),

$$\mathcal{F}\left\{W^{(3a)}_{3,1;\jmath,\ell}, V^{(3a)}_{3,1;\jmath,\ell\eta\eta}\right\}(\bar{x},k) = \tfrac{2}{3}\pi(\cos^2\theta)\int_k^\infty d\tilde{k}e^{\bar{\lambda}(k^3+2\tilde{k}^3)/9}\left\{\mathrm{i},2\tilde{k}\right\}\tilde{k}H(-\tilde{k})$$
$$B_\ell(\hat{x}_b)A_{\jmath-\ell}(\hat{x}_b+\tilde{k}), \quad (2.46)$$

where

$$\hat{x}_b = \bar{x} + (k-\tilde{k})/3, \quad (2.47)$$

and we have used the fact $P^{(3a)}_{3,1;\jmath,\ell} = 0$ which is obtained by matching the solution of (I.7.42) with the outer solution.

2.5. *The fourth-order equations for the plane-wave velocity jump*

The velocity jump for the plane wave can be obtained by solving (I.7.44) to (I.7.51) with the transverse boundary condition (I.7.54). The velocity jumps which produce the linear and mutual-interaction terms in the plane-wave amplitude equation will be presented. The back-reaction term in the plane-wave amplitude equation that is quartic in the oblique-mode amplitudes (Wu 1995) will be considered in future.

The linear velocity jump is obtained from (I.7.44),

$$\mathcal{F}\left\{U^{(4L)}_{2,0;j\eta}\right\}(\bar{x},k=0)\left[=\int_{-\infty}^{\infty}U^{(4L)}_{2,0;j\eta}d\eta\right]=2i\pi\bar{a}^{(2)}_{1M}B_j(\bar{x}). \tag{2.48}$$

The mutual-interaction term is determined by considering the components, $U^{(4b)}_{2,0;j,\ell\eta}$ and $U^{(4d)}_{2,0;j,\ell\eta}$ in (I.7.45) and $U^{(4c)}_{2,0;j,\ell,m\eta}$ in (I.7.49). The velocity jump by the $U^{(4b)}_{2,0;j,\ell\eta}$ component becomes, using (2.7), (I.7.10) and (I.7.13),

$$\mathcal{F}\left\{U^{(4b)}_{2,0;j,\ell\eta}\right\}(\bar{x},k=0)=8\pi\sum_{m:-1}\int_{-\infty}^{\bar{x}}dx_1\int_{-\infty}^{x_1}dx_2K^{(4b)}B_{j-\ell}(x_1)A_{\ell+m}(x_2)$$
$$A^*_m(2x_1+x_2-2\bar{x}), \tag{2.49}$$

where

$$K^{(4b)}=e^{-4\bar{\lambda}(\zeta_1+\zeta_2)\zeta_1^2}\zeta_1^3, \tag{2.50}$$

and (I.6.20) is used. With (2.7), (I.7.10) and (I.7.13) it is easy to show that

$$\mathcal{F}\left\{U^{(4d)}_{2,0;j,\ell\eta}\right\}(\bar{x},k=0)=0. \tag{2.51}$$

The jump by the $U^{(4c)}_{2,0;j,\ell,m\eta}$ component, obtained using (2.5), (2.17), (2.45), (2.46), (I.7.31) and (I.7.41), can be written as

$$\mathcal{F}\left\{U^{(4c)}_{2,0;j,\ell,m\eta}\right\}(\bar{x},k=0)=4\pi\int_{-\infty}^{\bar{x}}dx_1\int_{-\infty}^{x_1}dx_2K^{(4c)}_IA_{j-\ell}(x_1)B_m(x_2)A^*_{m-\ell}(x_1+2x_2-2\bar{x})$$
$$+\hat{\mathcal{U}}^{(4c)}_{II}+\hat{\mathcal{U}}^{(4c)}_{III}, \tag{2.52}$$

where

$$K^{(4c)}_I=e^{-\bar{\lambda}\left[4\zeta_1(\zeta_1+\zeta_2)^2+2\zeta_2^3/3\right]}\zeta_1(\zeta_1+\zeta_2)\hat{\xi}_l, \tag{2.53}$$

$$\hat{\mathcal{U}}^{(4c)}_{II}=\tfrac{8}{3}\pi h_s\int_{-\infty}^{\bar{x}}dx_1\int_{-\infty}^{x_1}dx_2\int_{-\infty}^{x_2}dx_3e^{-\bar{\lambda}\left(12\zeta_1^3+3\hat{\xi}_j^3+\hat{\xi}_i^3+2\zeta_3^3\right)/9}\zeta_1\zeta_3\left[1+\zeta_3(2\hat{\xi}_j-\zeta_1)\hat{\xi}_i^{-2}\right]$$
$$B_m(x_2)A_{\ell-m}(x_3)A^*_{\ell-j}(2x_2+x_3-2\bar{x}), \tag{2.54}$$

$$\hat{\mathcal{U}}_{III}^{(4c)} = 8\pi h_s \int_{-\infty}^{\bar{x}} dx_1 \int_{-\infty}^{x_1} dx_2 \int_{-\infty}^{x_1} dx_3 e^{-\bar{\lambda}\left(4\zeta_1^3+\zeta_2^3-\hat{\xi}_l^3+2\hat{\xi}_k^3\right)/3} \hat{\xi}_k \zeta_1 \left[1-(3\zeta_1+2\zeta_2)\hat{\xi}_k\hat{\xi}_l^{-2}\right]$$
$$A_{j-\ell}(x_2)B_m(x_3)A^*_{m-\ell}(x_2+2x_3-2\bar{x}), \quad (2.55)$$

$$\hat{\xi}_i \equiv 3\zeta_2+\zeta_3, \quad \hat{\xi}_j \equiv \hat{\xi}_i+2\zeta_1, \quad \hat{\xi}_k \equiv \hat{\xi}_j-\zeta_2, \quad \hat{\xi}_l \equiv 2\zeta_1+\zeta_2, \quad (2.56)$$

along with $\zeta_3 = x_2 - x_3$. Using (2.26) and integrating by parts, (2.54) and (2.55) can be rewritten as

$$\hat{\mathcal{U}}_{II}^{(4c)} = 4\pi h_s \int_{-\infty}^{\bar{x}} dx_1 \int_{-\infty}^{x_1} dx_2 K_{II}^{(4c)} B_m(x_1)A_{\ell-m}(x_2)A^*_{\ell-j}(2x_1+x_2-2\bar{x}), \quad (2.57)$$

$$\hat{\mathcal{U}}_{III}^{(4c)} = 4\pi h_s \int_{-\infty}^{\bar{x}} dx_1 \int_{-\infty}^{x_1} dx_2 \left[K_{IIIa}^{(4c)} B_m(x_1)A_{j-\ell}(x_2)A^*_{m-\ell}(2x_1+x_2-2\bar{x})\right.$$
$$\left. + K_{IIIb}^{(4c)} A_{j-\ell}(x_1)B_m(x_2)A^*_{m-\ell}(x_1+2x_2-2\bar{x})\right], \quad (2.58)$$

where

$$K_{II}^{(4c)} = \mathcal{G}_h^-(0,\zeta_2,\zeta_3;3,1,1), \quad K_{IIIa}^{(4c)} = \mathcal{G}_h^+(\zeta_1,\zeta_2,0;1,1,1), \quad K_{IIIb}^{(4c)} = \mathcal{G}_h^+(\zeta_1,0,0;1,\tfrac{3}{4},2), \quad (2.59)$$

$$\mathcal{G}_h^{\pm}(\zeta_a,\zeta_b,\zeta_c;\hat{a},\hat{b},\hat{c}) \equiv (2/\hat{a})e^{-(\hat{c}\bar{\lambda}/3)\left[\hat{\xi}_l^3+\left\{2-(-2)^{\hat{c}}\right\}\zeta_1^3+\zeta_b^3\right]}(2\zeta_a+\zeta_2)\left[(\zeta_1/\hat{a})(3\zeta_1+2\hat{b}\zeta_2)\right.$$
$$+\int_0^{\zeta_1} d\zeta_3 \exp\left\{\pm(2\hat{a}\bar{\lambda}/3)\left[(\zeta_3\mp 3\zeta_1)\zeta_3^2+2\zeta_2\zeta_c^2\mp(3/\hat{a})\hat{\xi}_l\zeta_b\zeta_3\right]\right\}\left\{\hat{\xi}_a-(2/\hat{a})(2\zeta_a+\zeta_2)\right.$$
$$\left.\left.\left[1+\bar{\lambda}\hat{\xi}_a(3\zeta_1+2\zeta_b-\zeta_3+4\zeta_c)(2\zeta_1-2\zeta_a+\zeta_b+\zeta_3)\right]\right\}\right], \quad (2.60)$$

and $\hat{\xi}_a$ and $\hat{\xi}_l$ are defined in (2.32) and (2.56).

3. Amplitude equations

The non-equilibrium amplitude equations for the frequency-detuned resonant-triads are derived by substituting the velocity jumps across the critical layer obtained in §2 into the jump equations (I.7.55) and (I.7.56).

By substituting (2.16), (2.18) – (2.20), (2.22), (2.36) and (2.40) along with (2.2) into (I.7.55), we obtain the frequency-detuned amplitude equation for the oblique modes (see also (4.2)), for $-J \leqslant \jmath \leqslant J$,

$$\left(\cos\theta + \frac{1}{\cos\theta}\right)\left[A_{\jmath\bar{x}} + \left\{\tfrac{\mathrm{i}}{2}\left(\jmath\bar{\chi} - \eta_o\right) - \kappa_{ob}\right\} A_\jmath\right] = \frac{\mathrm{i}}{\tau}\int_{-\infty}^{\bar{x}} dx_1 K_1(\bar{x}, x_1) B_\jmath(x_1) A_\jmath^*(2x_1 - \bar{x})$$
$$-\frac{\mathrm{i}}{4\tau}(\sec^2\theta)\sum_{\ell=-J}^{J}\int_{-\infty}^{\bar{x}} dx_1 \int_{-\infty}^{x_1} dx_2 \left[K_2(\bar{x}, x_1, x_2) A_\jmath(x_1) A_\ell(x_2) A_\ell^*(x_1 + x_2 - \bar{x})\right.$$
$$\left. + K_3(\bar{x}, x_1, x_2) A_\ell(x_1) A_\jmath(x_2) A_\ell^*(x_1 + x_2 - \bar{x})\right], \qquad (3.1)$$

where $\bar{x}$ and $\bar{\chi}$ are defined by (1.12). The frequency-detuned plane-wave amplitude equation is similarly obtained by substituting (2.48), (2.49), (2.51) and (2.52) along with (2.2) into (I.7.56), that is (see also (4.3)), for $-J \leqslant \jmath \leqslant J$,

$$B_{\jmath\bar{x}} + \left\{\mathrm{i}\left(\jmath\bar{\chi} - \eta_o\right) - \kappa_{2d}\right\} B_\jmath = -\frac{4\mathrm{i}}{\tau}\sum_{\ell=-J}^{J}\int_{-\infty}^{\bar{x}} dx_1 \int_{-\infty}^{x_1} dx_2 \left[K_4(\bar{x}, x_1, x_2) B_\jmath(x_1) A_\ell(x_2)\right.$$
$$\left. A_\ell^*(2x_1 + x_2 - 2\bar{x}) + K_5(\bar{x}, x_1, x_2) A_\ell(x_1) B_\jmath(x_2) A_\ell^*(x_1 + 2x_2 - 2\bar{x})\right]$$
$$+(\mathrm{back} - \mathrm{reaction} - \mathrm{term}). \qquad (3.2)$$

The oblique-mode amplitude $A_\jmath$ and the plane-wave amplitude $B_\jmath$ are normalized by (1.13). At the leading order, τ ($\equiv \bar{c}/(\tau_w Y_c)$ as defined by (I.7.18)) becomes unity and θ given by (1.4) becomes $\pi/3$. The transverse-coordinate origin shift η_o can be chosen to be zero as in (I.7.58). The analysis allows the value of J in (3.1) and (3.2) to be very large (as long as the magnitude of $J\chi$ in (1.6) is $O(1)$, see also §4). The upper and lower limits of the summations could also be arbitrary (i.e. $\sum_{\ell=J_1}^{J_2}$). The amplitude equations (3.1) and (3.2) (also (4.2) and (4.3)) are valid for any value of the local-growth-rate exponent r in the range $0 < r \leqslant 3$. The analysis can be extended to include higher-order effects in the amplitude equations (3.1) and (3.2) with minor modifications in their coefficients, which may be required for

good comparison with experiments (see Wundrow, Hultgren & Goldstein 1994 for excellent comparison of the linear growth rate).

The kernel functions, K_1 for the parametric-resonance term, K_2 and K_3 for the self-interaction term and K_4 and K_5 for the mutual-interaction term, are given by

$$K_1 = e^{-2\bar{\lambda}(\bar{x}-x_1)^3/3}(\bar{x}-x_1)^2, \tag{3.3}$$

$$K_2 = K^{(3c)} - 2\tau(\sin^2\theta)\left[K_{IIa}^{(3d)} - K_a^{(3e)} - K_b^{(3f)} + K_{IIa}^{(3h)}\right], \tag{3.4}$$

$$K_3 = K_I^{(3d)} - 2\tau(\sin^2\theta)\left[K_{IIb}^{(3d)} - K_b^{(3e)} - K_a^{(3f)} - K_I^{(3h)} + K_{IIb}^{(3h)}\right], \tag{3.5}$$

$$K_4 = 2K^{(4b)} + \tau(\sin^2\theta)\left[K_{II}^{(4c)} + K_{IIIa}^{(4c)}\right], \tag{3.6}$$

$$K_5 = K_I^{(4c)} + \tau(\sin^2\theta)K_{IIIb}^{(4c)}, \tag{3.7}$$

where $\bar{\lambda}$ is defined by (1.12). The $O(1)$-viscosity kernel functions for the self-interaction and mutual-interaction terms, which are obtained by substituting (2.21), (2.23), (2.28), (2.37), (2.38), (2.41) and (2.44) into (3.4) and (3.5) and by substituting (2.50), (2.53) and (2.59) into (3.6) and (3.7), respectively, are given Appendix A. The sum of K_2 in (A 1) and K_3 in (A 2) is the same as the self-interaction kernel function of the single-frequency (or single-resonant-triad) interaction given in Wu *et al.* (1993). The last terms which involve $\zeta_1\zeta_2$ in (A 1) and (A 2) appear with opposite signs in K_2 and K_3.

The oblique modes react back on the plane waves and the corresponding back-reaction term is quartic in the oblique-mode amplitudes (Goldstein & Lee 1992; Wu 1992, 1995). The kernel functions for the back-reaction term will be analyzed in future.

In the inviscid limit ($\bar{\lambda} = 0$), the kernel functions become

$$K_1 = (\bar{x}-x_1)^2, \tag{3.8}$$

$$K_2 = \left(1 - 2\tau \sin^2\theta\right)(\bar{x} - x_1)^3, \tag{3.9}$$

$$K_3 = \left(1 - 2\tau \sin^2\theta\right)(\bar{x} - x_1)(\bar{x} - x_2)\left[\bar{x} - x_1 + 2\tau(\sin^2\theta)(x_1 - x_2)\right], \tag{3.10}$$

$$K_4 = 2\left(1 - \tau \sin^2\theta\right)(\bar{x} - x_1)^3, \tag{3.11}$$

$$K_5 = \left(1 - \tau \sin^2\theta\right)(\bar{x} - x_1)(\bar{x} - x_2)(2\bar{x} - x_1 - x_2). \tag{3.12}$$

The linear growth rates of the oblique and plane waves, κ_{ob} and κ_{2d}, are

$$\kappa_{ob} = \frac{\sec\theta}{4(1 + \cos^2\theta)}\left[\frac{2}{\tau}\bar{a}_{1M}^{(2)} + \xi\left(2\sigma^r\hat{\kappa}\tau_w\bar{\lambda}\right)^{1/2}\right], \quad \kappa_{2d} = \frac{1}{\tau}\bar{a}_{1M}^{(2)} + \frac{\xi}{2}\left(\sigma^r\hat{\kappa}\tau_w\bar{\lambda}\right)^{1/2}, \tag{3.13}$$

where the real constant $\hat{\kappa}$ is a normalization parameter which can be chosen arbitrarily, τ_w is the total wall-shear stress (see (I.3.15) and (I.3.16)), $\bar{a}_{1M}^{(2)}$ is defined by (1.12) and ξ ($\equiv \bar{\alpha}/(\tau_w\bar{c})$ as defined by (I.7.57)) is unity at the leading order. The last terms in (3.13) are due to the viscous Stokes-layer effect. Their magnitude is $O(\sigma^{r/2})$ when the critical layer is governed by the non-equilibrium dynamics, but it becomes $O(1)$ in the viscous limit where $\bar{\lambda} = O(\sigma^{-r})$.

When the upstream flow is composed of a system of resonant-triads of linear instability waves (Goldstein & Lee 1992; Lee 1997a) the upstream boundary condition becomes, as in (I.7.59),

$$A_j \to \tilde{a}_j \exp\left[(\kappa_{ob} - \tfrac{i}{2}j\bar{\chi})\bar{x}\right], \quad B_j \to \tilde{b}_j \exp\left[(\kappa_{2d} - ij\bar{\chi})\bar{x}\right] \quad \text{as} \quad \bar{x} \to -\infty, \tag{3.14}$$

where the complex initial amplitudes $\tilde{a}_j$ and $\tilde{b}_j$ are given by (I.7.60). In the later downstream stage of the critical-layer evolution, the upstream boundary condition for the non-equilibrium amplitude equations in that local streamwise region is obtained by matching with the solutions of the preceding critical layer stage (Wundrow *et al.* 1994; Goldstein 1994; Wu, Leib & Goldstein 1997; Lee 1997a). The amplitude equations (3.1) and (3.2) are

valid for any value of the local-growth-rate exponent r (it was assumed that $0 < r \leqslant 3$ in Part 1).

The streamwise evolution of the instability waves is determined by solving the frequency-detuned amplitude equations (3.1) and (3.2) along with the upstream conditions (3.14). The numerical solutions of these amplitude equations will be given in §9. The frequency-detuned self-interaction term is composed of two summations in this multi-resonant-triad-interaction case. The wavenumber differences between the instability waves of the 0th and jth resonant-triads (that are given by (I.5.21)) produce the terms that involve $j\bar{\chi}$ in (3.1) and (3.2). By putting $J = 0$, we can recover the previously obtained amplitude equations (Goldstein & Lee 1992; Wu 1992, 1995; Wu *et al.* 1993; Lee 1997a). The nonlinear part of the amplitude equations (3.1) and (3.2) includes only one mean-flow-dependent parameter $\bar{\lambda}$.

In the later downstream stage of the non-equilibrium critical-layer evolution, the local-growth-rate exponent r becomes smaller than in the upstream non-equilibrium stage. The mean-boundary-layer flow develops on the long viscous length scale (x_v given by (I.2.1)). The boundary-layer thickness and the mean pressure gradient are nearly unchanged (within the order of approximation) over the region where the nonlinear interaction, or a series of nonlinear interactions, takes place. If we let the local-growth-rate exponent be r_o in the (first) upstream non-equilibrium critical-layer stage, the Reynolds number, mean pressure gradient and frequency detuning are scaled by, from (1.8), (1.3) and (1.7),

$$\frac{1}{R_\Delta} = \sigma^{3r_o+4}\lambda_o, \quad \mu = \sigma^{r_o-1}\bar{\mu}_o, \quad \hat{\chi} = \sigma^{r_o}\chi_o, \tag{3.15}$$

where λ_o, $\bar{\mu}_o$ and χ_o are $O(1)$ (of course they could be smaller). In the downstream region where the local value of r is smaller than r_o (we have only used the first equation in (1.3)

for the simplicity), λ, $\bar{\mu}$ and χ become

$$\lambda = \sigma^{3(r_o - r)}\lambda_o, \quad \bar{\mu} = \sigma^{r_o - r}\bar{\mu}_o, \quad \chi = \sigma^{r_o - r}\chi_o. \tag{3.16}$$

Therefore, the viscosity, mean pressure gradient and frequency detuning become less important in the downstream non-equilibrium region where $r < r_o$ (Wundrow *et al.* 1994).

From (1.12), (3.13) and (3.16), we can show that the linear growth rates κ_{ob} and κ_{2d} become negligibly small when r is smaller than r_o (where $r_o \leqslant 3$). Therefore, in this later non-equilibrium critical-layer stage, the instability wave amplitudes of the frequency-detuned resonant-triads are determined by the integro-differential equations (3.1) and (3.2) with the linear terms omitted and the kernel functions given by their inviscid limits.

4. Large frequency-detuning limit

If we put

$$\bar{\bar{A}}_j = A_j \exp(\tfrac{\mathrm{i}}{2} j\bar{\chi}\bar{x}), \quad \bar{\bar{B}}_j = B_j \exp(\mathrm{i}j\bar{\chi}\bar{x}), \tag{4.1}$$

the non-equilibrium amplitude equations (3.1) and (3.2) can be rewritten as

$$\left(\cos\theta + \frac{1}{\cos\theta}\right)\left\{\bar{\bar{A}}_{j\bar{x}} - \left(\tfrac{\mathrm{i}}{2}\eta_o + \kappa_{ob}\right)\bar{\bar{A}}_j\right\} = \frac{\mathrm{i}}{\tau}\int_{-\infty}^{\bar{x}} dx_1 K_1 \bar{\bar{B}}_j(x_1)\bar{\bar{A}}_j^*(2x_1 - \bar{x})$$
$$-\frac{\mathrm{i}}{4\tau}(\sec^2\theta)\int_{-\infty}^{\bar{x}} dx_1 \int_{-\infty}^{x_1} dx_2 \left[(K_2 + K_3)\bar{\bar{A}}_j(x_1)\bar{\bar{A}}_j(x_2)\bar{\bar{A}}_j^*(x_1 + x_2 - \bar{x}) + \sum_{\ell=-J,\ell\neq j}^{J} \mathcal{M}_s\right], \tag{4.2}$$

$$\bar{\bar{B}}_{j\bar{x}} - (\mathrm{i}\eta_o + \kappa_{2d})\bar{\bar{B}}_j = -\frac{4\mathrm{i}}{\tau}\int_{-\infty}^{\bar{x}} dx_1 \int_{-\infty}^{x_1} dx_2 \left[K_4 \bar{\bar{B}}_j(x_1)\bar{\bar{A}}_j(x_2)\bar{\bar{A}}_j^*(2x_1 + x_2 - 2\bar{x})\right.$$
$$\left. + K_5 \bar{\bar{A}}_j(x_1)\bar{\bar{B}}_j(x_2)\bar{\bar{A}}_j^*(x_1 + 2x_2 - 2\bar{x}) + \sum_{\ell=-J,\ell\neq j}^{J} \mathcal{M}_m\right] + \frac{\mathrm{i}}{\tau}\left(1 - \tau\sin^2\theta\right)\left(\sec^2\theta\right)$$
$$\int_{-\infty}^{\bar{x}} dx_1 \int_{-\infty}^{x_1} dx_2 \int_{-\infty}^{x_2} dx_3 \left[K_6 \bar{\bar{A}}_j(x_1)\bar{\bar{A}}_j(x_2)\bar{\bar{A}}_j(x_3)\bar{\bar{A}}_j^*(x_1 + x_2 + x_3 - 2\bar{x}) + \sum \mathcal{M}_b\right], \tag{4.3}$$

where K_1 - K_5 are given in the previous section and K_6 is given as, in the inviscid limit (see Wu 1995 for finite viscosity one),

$$K_6 = 2\tau\left(\sin^2\theta\right)\zeta_1^2\left[\left(1+2\tau\sin^2\theta\right)(\zeta_1+\zeta_2)^2+(\zeta_1+\zeta_2+\zeta_3)^2\right]+\left(1-2\tau\sin^2\theta\right)\zeta_1$$
$$\left[(2\zeta_1+\zeta_2)^2(3\zeta_1+2\zeta_2+\zeta_3)-2\tau\left(\sin^2\theta\right)\left\{\zeta_1^3+(\zeta_1+\zeta_2)(\zeta_1+\zeta_2+\zeta_3)(\zeta_1-\zeta_3)\right\}\right]. \quad (4.4)$$

We have put $\zeta_3 \equiv x_2 - x_3$ and ζ_1 and ζ_2 are defined in (2.3).

The multi-mode-coupling terms $\mathcal{M}_s$ and $\mathcal{M}_m$ ($\mathcal{M}_b$ is not derived in this paper), between the jth and ℓth resonant-triads, are given by

$$\mathcal{M}_s = e^{\frac{i}{2}\bar{\chi}(j-\ell)(\bar{x}-x_1)}K_2\bar{\bar{A}}_j(x_1)\bar{\bar{A}}_\ell(x_2)\bar{\bar{A}}^*_\ell(x_1+x_2-\bar{x})$$
$$+e^{\frac{i}{2}\bar{\chi}(j-\ell)(\bar{x}-x_2)}K_3\bar{\bar{A}}_\ell(x_1)\bar{\bar{A}}_j(x_2)\bar{\bar{A}}^*_\ell(x_1+x_2-\bar{x}), \quad (4.5)$$

$$\mathcal{M}_m = e^{i\bar{\chi}(j-\ell)(\bar{x}-x_1)}K_4\bar{\bar{B}}_j(x_1)\bar{\bar{A}}_\ell(x_2)\bar{\bar{A}}^*_\ell(2x_1+x_2-2\bar{x})$$
$$+e^{i\bar{\chi}(j-\ell)(\bar{x}-x_2)}K_5\bar{\bar{A}}_\ell(x_1)\bar{\bar{B}}_j(x_2)\bar{\bar{A}}^*_\ell(x_1+2x_2-2\bar{x}), \quad (4.6)$$

When $|\bar{\chi}(j-\ell)|$ is large, we can show that, by integrating by parts in the inviscid case,

$$\int_{-\infty}^{\bar{x}}dx_1\int_{-\infty}^{x_1}dx_2\mathcal{M}_s = \frac{96\,(1-2\tau\sin^2\theta)}{[\bar{\chi}(j-\ell)]^4}\bar{\bar{A}}_j(\bar{x})\int_{-\infty}^{\bar{x}}dx_1|\bar{\bar{A}}_\ell(x_1)|^2+O([\bar{\chi}(j-\ell)]^{-5}), \quad (4.7)$$

$$\int_{-\infty}^{\bar{x}}dx_1\int_{-\infty}^{x_1}dx_2\mathcal{M}_m = \frac{12\,(1-\tau\sin^2\theta)}{[\bar{\chi}(j-\ell)]^4}\bar{\bar{B}}_j(\bar{x})\int_{-\infty}^{\bar{x}}dx_1|\bar{\bar{A}}_\ell(x_1)|^2+O([\bar{\chi}(j-\ell)]^{-5}). \quad (4.8)$$

The effects of the multi-mode-coupling terms, $\mathcal{M}_s$ and $\mathcal{M}_m$ in (4.2) and (4.3), become negligibly small when the frequency difference becomes very large (we assume similar behavior for the $\mathcal{M}_b$ term).

In the real flow, there are infinite instabilities whose frequencies and wavenumbers are continuously varying. The individual critical layers are merged from the beginning

(of nonlinear process). The truncated finite summation in (1.10), (3.1), (3.2), (4.2) and (4.3) is an approximation to the infinite series. The instability waves whose wavenumbers, frequencies and linear growth rates can be scaled as in §1 are only included in the summation. The amplitudes of the other linear modes (i.e. of very high/low frequencies) have been assumed to be too small to play any major role in the nonlinear process. However, it is reasonable to expect that the growth of these other modes will be eventually governed by the frequency-detuned interaction in the downstream region where their nonlinear growth rates become much larger than the linear growth rates (that are different from (3.13)). The amplitude equations (4.2) and (4.3) (also (3.1) and (3.2)), that are obtained when the magnitude of $J\hat{\chi}$ is of $O(\sigma^r)$ (see (1.6)), can still be used, along with (4.7) and (4.8), for larger value of $J\hat{\chi}$ (but $J\hat{\chi}$ still smaller than $O(1)$).

5. The singular solution of the amplitude equation

The solutions of the amplitude equations (3.1) and (3.2) always develop a singularity at a finite downstream position $\bar{x}_s$ as will be shown in §9 and was shown in Goldstein & Lee (1992), Wu (1992) and Lee (1997a) for the single-resonant-triad interaction. Near the singular point where the exponent r is smaller than in the upstream region, the linear terms and the viscosity effect become of higher order as explained in the previous section. The amplitudes are then determined by (3.1) and (3.2) with the inviscid kernel functions (3.8) – (3.12) and with the linear terms neglected. The solutions to these equations can be written as (Goldstein & Choi 1989; Goldstein & Lee 1992; Wu 1992), when $\bar{x} \to \bar{x}_s$,

$$A_j = \bar{a}_j/(\bar{x}_s - \bar{x})^{3+i\psi_j}, \quad B_j = \bar{b}_j/(\bar{x}_s - \bar{x})^{4+2i\psi_j} \quad \text{for} \quad j = -J, \ldots, J, \qquad (5.1)$$

where ψ_j is a real constant and $\bar{a}_j$ and $\bar{b}_j$ are complex constants.

By substituting (5.1) into the inviscid amplitude equations (with the linear terms omitted), we can show that

$$\left(\cos\theta + \frac{1}{\cos\theta}\right)\frac{3+\mathrm{i}\psi_j}{|\bar{a}_j|^2} = \frac{\mathrm{i}}{\tau}\frac{\bar{b}_j}{\bar{a}_j^2}D_p(\psi_j) - \frac{\mathrm{i}(1-2\tau\sin^2\theta)}{4\tau(\cos^2\theta)}\sum_{\ell=-J}^{J}\frac{|\bar{a}_\ell|^2}{|\bar{a}_j|^2}D_s(\psi_j,\psi_\ell), \tag{5.2}$$

$$\frac{4+2\mathrm{i}\psi_j}{|\bar{a}_j|^2} = -\frac{4\mathrm{i}}{\tau}(1-\tau\sin^2\theta)\sum_{\ell=-J}^{J}\frac{|\bar{a}_\ell|^2}{|\bar{a}_j|^2}D_m(\psi_j,\psi_\ell) + (\mathrm{back}-\mathrm{reaction}-\mathrm{term}), \tag{5.3}$$

where the integrals D_p, D_s and D_m are given in Appendix B. The above equations can be solved numerically to determine $|\bar{a}_j|$, $|\bar{b}_j|$, ψ_j and the argument of $\bar{b}_j/\bar{a}_j^2$. As in the single-resonant-triad case (Goldstein & Lee 1992), (5.2) and (5.3) fix only the argument difference $\arg(\bar{b}_j/\bar{a}_j^2)$ and leave the individual arguments $\arg(\bar{a}_j)$ and $\arg(\bar{b}_j)$ undetermined.

From (1.9) and (1.10), we can show that the streamwise velocities of the plane and oblique modes, in the inviscid wall layer, become of the order of the base mean flow in the downstream region where $\bar{x}_s - \bar{x}$ is $O(\sigma^r)$.

From (5.1) along with (1.2) and (1.12), we can show that, as $\bar{x} \to \bar{x}_s$,

$$\frac{A_{jx}}{A_j} = \sigma^{r+1}\frac{\hat{\kappa}\tau_w\bar{\alpha}A_{j\bar{x}}}{2A_j} = \sigma^{r+1}\frac{\hat{\kappa}\tau_w\bar{\alpha}\,(3+\mathrm{i}\psi_j)}{2\,(\bar{x}_s-\bar{x})}, \quad \frac{B_{jx}}{B_j} = \sigma^{r+1}\frac{\hat{\kappa}\tau_w\bar{\alpha}B_{j\bar{x}}}{2B_j} = \sigma^{r+1}\frac{\hat{\kappa}\tau_w\bar{\alpha}\,(4+2\mathrm{i}\psi_j)}{2\,(\bar{x}_s-\bar{x})}. \tag{5.4}$$

Near the singular point, $\bar{x}_s - \bar{x}$ becomes small so that we can put

$$\bar{x}_s - \bar{x} = \sigma^n\,(\hat{x}_s - \hat{x}), \tag{5.5}$$

where the magnitude of $\hat{x}_s - \hat{x}$ is of $O(1)$. If the local growth rates are expressed as $A_{jx}/A_j = O(\sigma^{\hat{r}+1})$ and $B_{jx}/B_j = O(\sigma^{\hat{r}+1})$, then it follows from (5.4) and (5.5) that the local value $\hat{r}$ is given by

$$\hat{r} = r - n, \tag{5.6}$$

which shows that the local-growth-rate exponent $\hat{r}$ becomes smaller as the distance $\bar{x}_s - \bar{x}$ becomes shorter.

Since the critical-layer thickness in the non-equilibrium analysis is of the same order as the growth rate, the critical layer becomes thicker as the singular point is approached. The thicker critical layer leads to a wider range of instability-wave frequencies over which the frequency-detuned nonlinear interaction can occur (see (1.6)). All instability waves whose scaled frequency differences are nearly $O(1)$ can nonlinearly interact right before the scalings of this analysis break down, which occurs at the streamwise position where the critical layer is as thick as the inviscid wall layer and the unscaled distance from the singular point is of the order of the wavelength scale (Goldstein & Lee 1992; Wu *et al.* 1997).

6. Viscous-limit quasi-equilibrium amplitude equation

The quasi-equilibrium amplitude equations for the multi-resonant-triad interaction will be obtained by taking the viscous limit (Wu *et al.* 1993) of the finite-viscosity amplitude equations (3.1) and (3.2). Mankbadi, Wu & Lee (1993) and Wu (1993) derived the quasi-equilibrium amplitude equations for the single-resonant-triad interaction by considering the Tollmien-Schlichting waves in the upper-branch-scaling regime in the Blasius and favorable-pressure-gradient boundary layers, respectively.

In the viscous limit as $\bar{\lambda} \to \infty$, the kernel K_1 given by (3.3) becomes highly concentrated around $\bar{x} = x_1$ and the parametric-resonance term N_p in the oblique-mode amplitude equation (3.1) becomes (Goldstein & Lee 1993)

$$N_p = \frac{\mathrm{i}}{2\tau\bar{\lambda}} B_j(\bar{x}) A_j^*(\bar{x}). \tag{6.1}$$

The viscous limit of the frequency-detuned self-interaction terms shows that the leading-order terms are produced by the second double-integral term (whose kernel function is K_3) in (3.1). Following Wu *et al.* (1993), we can show that the viscous limit of the integral which involves the second term $2h_s \int_0^{\zeta_2} d\zeta_3(\ldots)$ in (A 2) becomes

$$-\frac{\mathrm{i}}{2\bar{\lambda}^{4/3}}(\tan^2\theta)\left(\frac{1}{18}\right)^{1/3}\Gamma(\tfrac{1}{3})\sum_{\ell=-J}^{J}A_\ell(\bar{x})\int_{-\infty}^{\bar{x}}dx_1 A_j(x_1)A_\ell^*(x_1), \tag{6.2}$$

and the viscous limit of the integral which involves the fourth term $\mathcal{F}_a^-(\zeta_1,\zeta_2,\zeta_3|0,\zeta_2)$ in (A 2) becomes

$$\frac{\mathrm{i}\tau}{\bar{\lambda}^{4/3}}(\tan^2\theta\sin^2\theta)\left(\frac{1}{18}\right)^{1/3}\Gamma(\tfrac{1}{3})\sum_{\ell=-J}^{J}A_\ell(\bar{x})\int_{-\infty}^{\bar{x}}dx_1 A_j(x_1)A_\ell^*(x_1), \tag{6.3}$$

where $\Gamma(1/3) = 2.6789$ is the Gamma function. The above two terms in K_3 are originated from $K_I^{(3d)}$, $K_{IIb}^{(3d)}$, $K_I^{(3h)}$ and $K_{IIb}^{(3h)}$ given by (2.23), (2.28), (2.41) and (2.44). The nonlinear interactions of the $U_{0,2;j,\ell}^{(2)}$, $V_{0,2;j,\ell}^{(2)}$ and $W_{0,2;j,\ell}^{(2)}$ components, as given by (I.7.26) and (I.7.30), are responsible for the velocity jumps of the $(3d)$ and $(3h)$ components in (2.22) and (2.40) (Wu *et al.* 1993). This is consistent with the results of the quasi-equilibrium critical-layer analyses by Mankbadi *et al.* (1993) and Wu (1993) who showed that the spanwise-periodic mean-flow distortion is responsible for the velocity jump across the diffusion layer. The magnitude of the viscous limits of the integrals which involve the other terms of K_3 in (A 2) and the kernel K_2 in (A 1) are all of $O(\bar{\lambda}^{-5/3})$ or smaller (Wu *et al.* 1993). The frequency-detuned self-interaction term N_s becomes as $\bar{\lambda}\to\infty$, from (6.2) and (6.3),

$$N_s = -\frac{\mathrm{i}}{2\bar{\lambda}^{4/3}}\left(1-2\tau\sin^2\theta\right)(\tan^2\theta)\left(\frac{1}{18}\right)^{1/3}\Gamma(\tfrac{1}{3})\sum_{\ell=-J}^{J}A_\ell(\bar{x})\int_{-\infty}^{\bar{x}}dx_1 A_j(x_1)A_\ell^*(x_1). \tag{6.4}$$

Similarly, we can show that the mutual-interaction term N_m in the plane-wave ampli-

tude equation (3.2) becomes in the viscous limit,

$$N_m = -\frac{4\mathrm{i}}{\tau\bar{\lambda}^{5/3}} C_m \sum_{\ell=-J}^{J} B_j(\bar{x})|A_\ell(\bar{x})|^2, \tag{6.5}$$

where C_m is a real constant that can be obtained by integrating the kernel functions K_4 and K_5 given by (A 3) and (A 4) with $\bar{\lambda} = 1$ for the exponential terms and with $\mathcal{F}_b^{\pm}$ that is redefined as not to include the last term $\bar{\lambda}(\zeta_1 - \zeta_3)(\ldots)(\ldots)$ in (A 7),

$$C_m = \int_{-\infty}^{\bar{x}} dx_1 \int_{-\infty}^{x_1} dx_2 \left[K_4(\bar{x}, x_1, x_2|\bar{\lambda} = 1; \mathcal{F}_b^{\pm}) + K_5(\bar{x}, x_1, x_2|\bar{\lambda} = 1; \mathcal{F}_b^{+})\right]. \tag{6.6}$$

We can assume, from the back-reaction term in the single-resonant-triad case given by Wu (1995), that the viscous limit of the back-reaction term N_b is

$$N_b = O\left(1/\bar{\lambda}^N\right), \tag{6.7}$$

with N larger than 5/3, which has been indirectly proved by the quasi-equilibrium analyses of Mankbadi *et al.* (1993) and Wu (1993).

With (6.1), (6.4), (6.5) and (6.7), the amplitude equations (3.1) and (3.2) become in the limit as $\bar{\lambda} \to \infty$,

$$\left(\cos\theta + \frac{1}{\cos\theta}\right)\left[A_{j\bar{x}} + \left(\tfrac{\mathrm{i}}{2} j\bar{\chi} - \kappa_{ob}\right) A_j\right] = N_p + N_s, \tag{6.8}$$

$$B_{j\bar{x}} + (\mathrm{i}j\bar{\chi} - \kappa_{2d})\, B_j = 0, \tag{6.9}$$

where κ_{ob} and κ_{2d} are given by (3.13) and we have put $\eta_o = 0$ (see (I.7.58)).

If we rescale the viscosity parameter and the amplitudes as in Lee (1997a),

$$\hat{\lambda} = \sigma^r \bar{\lambda}, \quad \hat{A}_j = \sigma^{2r/3} A_j, \quad \hat{B}_j = \sigma^r A_j, \tag{6.10}$$

the above equations (6.8) and (6.9) can be rewritten as (see also (6.17) and (6.18)), for $\jmath = -J, \ldots, J$,

$$\left(\cos\theta + \frac{1}{\cos\theta}\right)\left[\hat{A}_{\jmath\bar{x}} + \left(\tfrac{\mathrm{i}}{2}\jmath\bar{\chi} - \hat{\kappa}_{ob}\right)\hat{A}_\jmath\right] = \frac{\mathrm{i}}{2\tau\hat{\lambda}}\hat{B}_\jmath(\bar{x})\hat{A}^*_\jmath(\bar{x})$$

$$-\frac{\mathrm{i}}{2\hat{\lambda}^{4/3}}\left(1 - 2\tau\sin^2\theta\right)(\tan^2\theta)\left(\frac{1}{18}\right)^{1/3}\Gamma(\tfrac{1}{3})\sum_{\ell=-J}^{J}\hat{A}_\ell(\bar{x})\int_{-\infty}^{\bar{x}} dx_1\hat{A}_\jmath(x_1)\hat{A}^*_\ell(x_1), \qquad (6.11)$$

$$\hat{B}_{\jmath\bar{x}} + (\mathrm{i}\jmath\bar{\chi} - \hat{\kappa}_{2d})\hat{B}_\jmath = 0, \qquad (6.12)$$

with

$$\hat{\kappa}_{ob} = \frac{\sec\theta}{4(1+\cos^2\theta)}\left[\frac{2}{\tau}\bar{a}^{(2)}_{1M} + \xi\left(2\hat{\kappa}\tau_w\hat{\lambda}\right)^{1/2}\right], \quad \hat{\kappa}_{2d} = \frac{1}{\tau}\bar{a}^{(2)}_{1M} + \frac{\xi}{2}\left(\hat{\kappa}\tau_w\hat{\lambda}\right)^{1/2}, \qquad (6.13)$$

where the normalization parameter $\hat{\kappa}$ can be chosen arbitrarily, τ and ξ (as defined by (I.7.18) and (I.7.57)) are equal to one, $\bar{\chi}$ and $\bar{a}^{(2)}_{1M}$ are given by (1.12) and τ_w is the total wall-shear stress (see (I.3.15) and (I.3.16)). The linear growth rates $\hat{\kappa}_{ob}$ and $\hat{\kappa}_{2d}$ were obtained by substituting (6.10) into (3.13). As we expected, the viscous Stokes-layer effect becomes $O(1)$ in the viscous-limit linear growth rates.

The streamwise evolution of a system of frequency-detuned resonant-triads that are composed of the Tollmien-Schlichting waves is determined by the quasi-equilibrium amplitude equations (6.11) and (6.12). The value of the exponent r is 3 for the Blasius boundary layer and 1 for the favorable-pressure-gradient boundary layer. These amplitude equations (6.11) and (6.12) can also be directly derived from the frequency-detuned quasi-equilibrium critical-layer analysis (Mankbadi *et al.* 1993; Wu 1993). The quasi-equilibrium critical-layer scaling can be obtained by rescaling the non-equilibrium scaling given in §1 using (6.10) (see table 1 of Lee 1997a). The equations (6.11) and (6.12) (also (6.17) and (6.18)) for the frequency-detuned multi-resonant-triads reduce to the amplitude equations of Mankbadi *et al.* (1993) and Wu (1993) if we put $J = 0$.

The plane waves grow linearly, i.e.

$$\hat{B}_J = \hat{b}_J \exp\left[(\hat{\kappa}_{2d} - \mathrm{i}J\bar{\chi})\,\bar{x}\right], \tag{6.14}$$

in the entire quasi-equilibrium region. The streamwise evolution of $\hat{A}_J$ can be obtained by solving (6.11) with the linear upstream condition

$$\hat{A}_J \to \hat{a}_J \exp\left[(\hat{\kappa}_{ob} - \tfrac{\mathrm{i}}{2}J\bar{\chi})\bar{x}\right]. \tag{6.15}$$

The complex constants $\hat{a}_J$ and $\hat{b}_J$ are given by the equations similar to (I.7.60). The results of the numerical computations are presented in §8.

The growth of the frequency-detuned Tollmien-Schlichting waves in the upper-branch-scaling regime is governed by the quasi-equilibrium amplitude equations (6.11) and (6.12). However, this initial quasi-equilibrium stage will be eventually followed by the non-equilibrium critical-layer stage where the amplitudes are determined by the integro-differential equations (3.1) and (3.2) (Goldstein 1994; Wu *et al.* 1997; Lee 1997a).

If we put

$$\hat{\hat{A}}_J = \hat{A}_J \exp(\tfrac{\mathrm{i}}{2}J\bar{\chi}\bar{x}), \quad \hat{\hat{B}}_J = \hat{B}_J \exp(\mathrm{i}J\bar{\chi}\bar{x}), \tag{6.16}$$

the equations (6.11) and (6.12) can be rewritten as

$$\left(\cos\theta + \frac{1}{\cos\theta}\right)\left(\hat{\hat{A}}_{J\bar{x}} - \hat{\kappa}_{ob}\hat{\hat{A}}_J\right) = \frac{\mathrm{i}}{2\tau\hat{\lambda}}\hat{\hat{B}}_J(\bar{x})\hat{\hat{A}}_J^*(\bar{x})$$
$$-\frac{\mathrm{i}}{2\hat{\lambda}^{4/3}}\left(1 - 2\tau\sin^2\theta\right)(\tan^2\theta)\left(\frac{1}{18}\right)^{1/3}\Gamma(\tfrac{1}{3})\left[\hat{\hat{A}}_J(\bar{x})\int_{-\infty}^{\bar{x}} dx_1|\hat{\hat{A}}_J(x_1)|^2 + \sum_{\ell=-J,\ell\neq J}^{J}\mathcal{M}_q\right], \tag{6.17}$$

$$\hat{\hat{B}}_{J\bar{x}} - \hat{\kappa}_{2d}\hat{\hat{B}}_J = 0, \tag{6.18}$$

where

$$\mathcal{M}_q = \hat{\hat{A}}_\ell(\bar{x})\int_{-\infty}^{\bar{x}} dx_1 e^{\frac{\mathrm{i}}{2}\bar{\chi}(J-\ell)(\bar{x}-x_1)}\hat{\hat{A}}_J(x_1)\hat{\hat{A}}_\ell^*(x_1). \tag{6.19}$$

As in §4, we can show that

$$\mathcal{M}_q = \frac{2\mathrm{i}}{\bar{\chi}(\jmath-\ell)}\hat{A}_\jmath(\bar{x})|\hat{A}_\ell(\bar{x})|^2 + O([\bar{\chi}(\jmath-\ell)]^{-2}), \tag{6.20}$$

in the large frequency-detuning limit (when $|\bar{\chi}(\jmath-\ell)|$ is large).

7. Nonlinearly-generated low-frequency modes

Goldstein & Choi (1989), Goldstein & Lee (1992) and Wu (1992) showed that the nonlinear interaction between oblique modes of the same frequency produces a spanwise-periodic mean-flow distortion. However, the nonlinear interaction between the frequency-detuned oblique modes generates low-frequency modes in addition to the spanwise-periodic mean-flow distortion. The frequencies of these nonlinearly-generated modes are equal to the frequency differences between the primary oblique modes, therefore, they are very low (of $O(\sigma^{r+2})$). From (2.8) and (I.7.11) along with (2.2), we can show that

$$\Delta U^{(2)}_{0,2;\jmath,\ell}(\bar{x}) \equiv \int_{-\infty}^{\infty} U^{(2)}_{0,2;\jmath,\ell\eta}d\eta = -4\pi\tau(\sin^2\theta)\int_{-\infty}^{\bar{x}} dx_1\mathcal{H}_1(\bar{x}-x_1)A_{\jmath+\ell}(x_1)A^*_\ell(x_1), \tag{7.1}$$

$$\Delta V^{(2)}_{0,2;\jmath,\ell}(\bar{x}) \equiv \int_{-\infty}^{\infty} V^{(2)}_{0,2;\jmath,\ell\eta}d\eta = 4\mathrm{i}\pi\tau(\sin^2\theta)\int_{-\infty}^{\bar{x}} dx_1\mathcal{H}_0(\bar{x}-x_1)A_{\jmath+\ell}(x_1)A^*_\ell(x_1), \tag{7.2}$$

$$\Delta W^{(2)}_{0,2;\jmath,\ell} \equiv \int_{-\infty}^{\infty} W^{(2)}_{0,2;\jmath,\ell\eta}d\eta = 0, \tag{7.3}$$

where

$$\mathcal{H}_n(\bar{x}) \equiv \int_0^{\bar{x}} d\tilde{x}e^{-2\bar{\lambda}\tilde{x}^3/3}(\bar{x}-\tilde{x})^n, \tag{7.4}$$

θ, $\bar{x}$ and $\bar{\lambda}$ are defined in (1.4) and (1.12), η is defined by (I.7.1) and τ (given in (I.7.18)) is equal to one. We can also show from (7.1) and (7.2) that

$$\Delta V^{(2)}_{0,2;\jmath,\ell}(\bar{x}) = -\mathrm{i}\frac{\partial}{\partial\bar{x}}\left[\Delta U^{(2)}_{0,2;\jmath,\ell}(\bar{x})\right]. \tag{7.5}$$

The streamwise evolution of $A_\jmath$ is determined by solving the frequency-detuned amplitude equations (3.1) and (3.2), therefore, the velocity jumps (7.1) and (7.2) are determined from the nonlinear critical-layer interaction. In order to match with these nonlinearly generated jumps, the low-frequency modes in the inviscid wall layer (where $y = \sigma Y$) must be written as, for $Y \gtrless Y_c$,

$$u_{0,2} = \sigma^{3r+1} \sum_{\jmath=-2J}^{2J} \sum_{\ell:-1} \mathrm{Re}\left\{ \tilde{\tilde{U}}^{(2)\pm}_{0,2;\jmath,\ell}(Y,\bar{x}) e^{\mathrm{i}\jmath(\bar{\chi}\bar{x}-t_1/2)} \right\} \cos\left[2Z + (\jmath+2\ell)z_1\right], \tag{7.6}$$

$$v_{0,2} = \sigma^{4r+3} \sum_{\jmath=-2J}^{2J} \sum_{\ell:-1} \mathrm{Re}\left\{ \mathrm{i}\tilde{\tilde{V}}^{(2)\pm}_{0,2;\jmath,\ell}(Y,\bar{x}) e^{\mathrm{i}\jmath(\bar{\chi}\bar{x}-t_1/2)} \right\} \cos\left[2Z + (\jmath+2\ell)z_1\right], \tag{7.7}$$

along with similar forms for $w_{0,2}$ and $p_{0,2}$, where $t_1 (= \sigma^{r+2}\chi\bar{s}t)$ and $z_1 (= \sigma^{r+1}\sqrt{3}\tilde{\chi}\bar{\alpha}z/4)$ are defined by (I.5.24), $\bar{\chi}$ is defined by (1.12) and $\sum_{\ell:-1}$ denotes $\sum_{\ell=\max(-J,-J-\jmath)}^{\min(J-\jmath,J)}$ as was given in (I.6.20). The spanwise velocity $w_{0,2}$ and the pressure $p_{0,2}$ are continuous across the critical layer (see (7.3) and (I.7.16)). The magnitude of the streamwise component $u_{0,2}$ given by (7.6) is as big as that of the primary oblique mode (see (I.5.30) where $\bar{\tilde{U}}_{0,2;\jmath,\ell} = \tilde{\tilde{U}}^{(2)\pm}_{0,2;\jmath,\ell} e^{\mathrm{i}\jmath\bar{\chi}\bar{x}}$). The nonlinearly-generated low-frequency modes are functions of the slow time t_1 and the magnitude of their frequencies is of $O(\sigma^{r+2})$.

The shape functions $\tilde{\tilde{U}}^{(2)\pm}_{0,2;\jmath,\ell}$ and $\tilde{\tilde{V}}^{(2)\pm}_{0,2;\jmath,\ell}$ are discontinuous at the critical level $Y = Y_c$. We can show from (I.6.5) – (I.6.7), (I.6.14) and (I.B2) that they have to satisfy the following equations

$$\tilde{\tilde{U}}^{(2)+}_{0,2;\jmath,\ell}(Y = Y_c^+) - \tilde{\tilde{U}}^{(2)-}_{0,2;\jmath,\ell}(Y = Y_c^-) = \frac{2\hat{\kappa}^3}{M}(\tan^2\theta)\Delta U^{(2)}_{0,2;\jmath,\ell}, \tag{7.8}$$

$$\tilde{\tilde{V}}^{(2)+}_{0,2;\jmath,\ell}(Y = Y_c^+) - \tilde{\tilde{V}}^{(2)-}_{0,2;\jmath,\ell}(Y = Y_c^-) = -\frac{\hat{\kappa}^4\bar{\alpha}\bar{c}}{M}(\tan^2\theta)\Delta V^{(2)}_{0,2;\jmath,\ell}, \tag{7.9}$$

where $\Delta U^{(2)}_{0,2;\jmath,\ell}$ and $\Delta V^{(2)}_{0,2;\jmath,\ell}$ are given by (7.1) and (7.2), M is given by the phrase below (1.13) (also in (I.7.5)) and $\hat{\kappa}$ is the normalization parameter introduced in (1.12).

In the upstream linear region where A_j is given by (3.14), the critical-layer jump $\Delta U^{(2)}_{0,2;j,\ell}$ in (7.1) becomes, as $\bar{x} \to -\infty$,

$$\Delta U^{(2)}_{0,2;j,\ell} = -\frac{4\pi^2\tau}{(2\bar{\lambda})^{1/3}}(\sin^2\theta)\mathrm{Hi}\left[\frac{-2\kappa_{ob}+\frac{\mathrm{i}}{2}j\bar{\chi}}{(2\bar{\lambda})^{1/3}}\right]\frac{\tilde{a}_{j+\ell}\tilde{a}^*_\ell}{\left(2\kappa_{ob}-\frac{\mathrm{i}}{2}j\bar{\chi}\right)^2}\exp\left[(2\kappa_{ob}-\tfrac{\mathrm{i}}{2}j\bar{\chi})\bar{x}\right], \quad (7.10)$$

where Hi is the Airy function (Abramowitz & Stegun 1965, p.448). In the inviscid limit where $\bar{\lambda} = 0$, (7.10) can be written as

$$\Delta U^{(2)}_{0,2;j,\ell} = -4\pi\tau(\sin^2\theta)\left(2\kappa_{ob}-\tfrac{\mathrm{i}}{2}j\bar{\chi}\right)^{-3}\tilde{a}_{j+\ell}\tilde{a}^*_\ell\exp\left[(2\kappa_{ob}-\tfrac{\mathrm{i}}{2}j\bar{\chi})\bar{x}\right]. \quad (7.11)$$

The transverse velocity jump $\Delta V^{(2)}_{0,2;j,\ell}$ can be obtained by differentiating (7.10) and (7.11) with respect to $\bar{x}$ as shown by (7.5). The streamwise growth rates of $\Delta U^{(2)}_{0,2;j,\ell}$ and $\Delta V^{(2)}_{0,2;j,\ell}$ in the linear region are twice the linear growth rate of the oblique mode.

Near the singular point the viscous effect becomes small and the amplitude is given by (5.1). We can show that the jump (7.1) becomes, when $\bar{x} \to \bar{x}_s$,

$$\Delta U^{(2)}_{0,2;j,\ell} = -\frac{4\pi\tau(\sin^2\theta)\tilde{a}_{j+\ell}\tilde{a}^*_\ell}{(3+\mathrm{i}\Delta\psi_{j,\ell})(4+\mathrm{i}\Delta\psi_{j,\ell})(5+\mathrm{i}\Delta\psi_{j,\ell})}\frac{1}{(\bar{x}_s-\bar{x})^{3+\mathrm{i}\Delta\psi_{j,\ell}}}, \quad (7.12)$$

where we have put $\Delta\psi_{j,\ell} \equiv \psi_{j+\ell} - \psi_\ell$.

The numerical evaluation of the velocity jumps $\Delta U^{(2)}_{0,2;j,\ell}$ and $\Delta V^{(2)}_{0,2;j,\ell}$ will be presented in §9 along with the numerical solutions of the amplitude equations.

The analysis in the critical layer only determines the critical-layer jumps of the streamwise and transverse velocities of the low-frequency (spanwise-periodic) modes. The complete solutions of the nonlinearly-generated low-frequency modes can be obtained from the multi-layer analysis (Wu 1993). When $r = 3$ and λ defined by (1.8) is $O(1)$ in the single-resonant-triad-interaction case (Goldstein & Lee 1992), we need to consider the steady spanwise-periodic (mean-flow-distortion) mode in the potential region where $y = \tilde{y}/\sigma$, the

main boundary layer where $y = O(1)$ and the viscous wall layer where $y = \sigma^3\hat{Y}$ in addition to the inviscid wall layer of $O(\sigma)$ and the critical layer of $O(\sigma^4)$. The viscous wall layer, which is thicker than the viscous Stokes layer for the oblique and plane waves of the resonant-triad, is required in order to satisfy the wall boundary conditions. (The inviscid-wall-layer solutions of the streamwise and spanwise components become singular at the wall.) The three-dimensional boundary-layer equations in the viscous wall layer must be solved with the no-slip boundary conditions at the wall and appropriate boundary conditions on the upper edge of the layer in order to match with the solutions in the inviscid wall layer. The transverse velocity on the upper edge of the viscous wall layer is determined internally by the boundary-layer equations themselves and so its value can not be given as a boundary condition as was done in Wu (1993). It is interesting to note that the streamwise and transverse velocity components in the inviscid wall layer, at leading order, become equal to zero where $Y > Y_c$ but non-zero where $Y < Y_c$ (Lee 1997c). Thus, the nonlinear interaction between oblique modes of the same frequency produces, at the leading order, the spanwise-periodic mean-flow distortion only below the critical layer. The non-zero velocities at $Y = Y_{c-}$ will be determined by matching with the critical-layer jumps.

Since the critical-layer jump of the spanwise-periodic mean-flow distortion is determined from the solutions of the amplitude equations, which become singular at a finite downstream position, the nonlinearly-generated spanwise-periodic mode becomes very large near the singular point. When the value of the local-growth-rate exponent r becomes $9/10$, the streamwise velocity of the mean-flow distortion becomes as big as the base mean flow near the wall. Therefore, the nonlinearly-generated spanwise-periodic mode and the base mean flow start to interact nonlinearly in the nonlinear viscous wall layer whose thickness

is of $O(\sigma^{37/10})$ (Lee 1997c). This nonlinear viscous wall layer will be separated into two layers (inviscid nonlinear layer and the viscous nonlinear layer) in the later downstream region. The details of the evolution of this nonlinearly-generated mode will be presented in a forthcoming paper.

8. Numerical solutions of the quasi-equilibrium amplitude equations

The quasi-equilibrium amplitude equations derived in §6 are solved numerically. The frequency-detuned amplitude equations (6.11) and (6.12) determine the streamwise evolution of a system of frequency-detuned resonant-triads of the Tollmien-Schlichting waves.

A predictor-corrector method (see Gear 1971) is used to solve the oblique-mode amplitude equation (6.11) subject to the upstream condition (6.15), along with the linear plane wave given by (6.14). As in Lee (1997a), the Adams-Bashforth method was used for the predictor step and the Adams-Moulton method was used for the corrector step. The typical streamwise grid size is 0.002 and the streamwise integration starts about $\bar{x} = -20$.

The numerical results in this section are obtained when $\hat{\lambda} = 1$, $\hat{\kappa}_{ob} = 4/5$ and $\hat{\kappa}_{2d} = 1$. The exact linear growth rates can be obtained from (6.13) for the specific problem. We have also put $\theta = \pi/3$ and $\tau = 1$ (see (1.4) and (I.7.18)). The initial amplitudes of the plane and oblique modes are $\hat{b}_j = 1$ and $\hat{a}_j = 0.01\exp(i\pi/4)$ for all j. We have put the argument of the initial oblique-mode amplitude to be $\pi/4$ radian since it gives the most effective parametric-resonance growth of the oblique modes as shown in Lee (1997a).

The general behavior of the solutions of the quasi-equilibrium amplitude equations in this multi-resonant-triad case is the same as in the single-resonant-triad case (Mankbadi *et al.* 1993; Wu 1993; Lee 1997a). The upstream linear growth of the oblique modes is

enhanced due to the parametric-resonance effect when the plane wave amplitudes become sufficiently large. The self-interaction between the frequency-detuned oblique modes causes the oblique-mode amplitudes to become saturated, which then grow linearly with oscillations. Meanwhile, the plane wave continues to grow linearly in the entire region.

Figure 1 shows the results of the nonlinear interaction between two frequency-detuned resonant-triads when $\jmath = 0$ and 1. The solution of the single resonant-triad interaction is plotted as the dotted curve. The linear oblique-mode amplitude is plotted as the dot-dashed curve. Both plane-wave amplitudes $\hat{B}_0$ and $\hat{B}_1$ grow linearly as given by (6.14). In figure 1a, the result when the frequency-detuning factor $\bar{\chi}$ is equal to zero is plotted as the dashed curve ($\hat{A}_0$ and $\hat{A}_1$ are identical). The saturation amplitude is smaller than that of the single resonant-triad interaction because of the doubled self-interaction effect when $\bar{\chi} = 0$. For the non-zero values of $\bar{\chi}$, the saturation amplitude of $\hat{A}_0$ is larger than that of $\hat{A}_1$. The frequency of the 0th resonant-triad is lower than that of the 1st resonant-triad (see (1.6)). When the frequency detuning is very large the multi-mode-coupling term $\mathcal{M}_q$ in (6.17) becomes very small. Thus, the resonant-triads grow almost independently of each other and the amplitudes $\hat{A}_0$ and $\hat{A}_1$ become close to that of the single resonant-triad interaction (within the range of the computation) as shown in figure 1d.

The numerical results of the three and five resonant-triad interactions are given in figures 2 and 3, respectively. The straight lines for the plane wave amplitudes are not plotted. The oblique-mode amplitude for the single resonant-triad interaction is plotted as the dotted curve. Both figures 2 and 3 (and figure 1) show that the saturation amplitude of the oblique mode of lower frequency (i.e. the one that has the lower value of $\jmath$) is larger than that of higher frequency.

Since the effect of the spanwise-wavenumber (or propagation angle) detuning is not included in this analysis, the oblique-mode amplitudes $|\hat{A}_j|$ are the same for all j in the parametric-resonance region. The spanwise-wavenumber detuning can be included by relaxing the condition (I.5.16). The instability waves whose (scaled) spanwise-wavenumbers are detuned by $O(\sigma^r)$ share the same critical layer and, thus, nonlinearly interact.

9. Numerical solutions of the non-equilibrium oblique-mode amplitude equations

The results of the numerical computations of the frequency-detuned oblique-mode amplitude equation (3.1) will be presented in this section. The critical-layer velocity jumps (7.1) and (7.2) of the nonlinearly-generated low-frequency (spanwise-periodic) modes will also be evaluated.

We have observed in the single-resonant-triad-interaction analyses by Goldstein & Lee (1992) and Lee (1997a) that the self-interaction between oblique modes is mostly responsible for the explosive growth of the amplitudes near the singular point. Therefore, we will investigate the effect of the frequency-detuned self-interaction term first. There are, of course, many important shear flows (i.e. compressible free shear layer, supersonic boundary layer and others) where the the oblique mode is the most unstable wave and the self-interaction is the dominant nonlinear interaction.

It is convenient to choose the normalization parameter $\hat{\kappa}$, which was introduced in (1.12) (or (I.7.1)), to be

$$\hat{\kappa} = \frac{2\pi Y_c \bar{\alpha}}{\tau_w^3 \bar{c}} a_{1M}^{(2)}, \tag{9.1}$$

and we have shown in (1.4) and (I.7.18) that

$$\theta = \pi/3, \quad \tau = 1. \tag{9.2}$$

If we put (I.7.58), (1.12), (9.1) and (9.2) along with $B_j = 0$ into (3.1) and (3.13), the frequency-detuned non-equilibrium amplitude equation of the oblique modes can be rewritten as, for $-J \leqslant j \leqslant J$,

$$A_{j\bar{x}} = \left(\tfrac{4}{5} - \tfrac{\mathrm{i}}{2} j\bar{\chi}\right) A_j - \tfrac{2}{5}\mathrm{i} \sum_{\ell=-J}^{J} \int_{-\infty}^{\bar{x}} dx_1 \int_{-\infty}^{x_1} dx_2 \left[K_2(\bar{x}, x_1, x_2) A_j(x_1) A_\ell(x_2) A_\ell^*(x_1 + x_2 - \bar{x}) \right.$$
$$\left. + K_3(\bar{x}, x_1, x_2) A_\ell(x_1) A_j(x_2) A_\ell^*(x_1 + x_2 - \bar{x})\right], \tag{9.3}$$

where the kernel functions K_2 and K_3 are given by (3.9) and (3.10) in the inviscid limit. The above equation (9.3) will be solved with the linear upstream condition (3.14), which can be rewritten as

$$A_j \to \tilde{a}_j \exp\left[(\tfrac{4}{5} - \tfrac{\mathrm{i}}{2} j\bar{\chi})\bar{x}\right] \quad \text{as} \quad \bar{x} \to -\infty. \tag{9.4}$$

The effects of the magnitude of the initial amplitudes $|\tilde{a}_j|$ and the frequency-detuning factor $\bar{\chi}$ on the streamwise evolution of the amplitudes A_j will be shown in the following subsections when $\bar{\lambda} = 0$.

As in before (Goldstein & Lee 1992; Lee 1997a), the Adams-Moulton method (see Gear 1971) is used to advance the solutions downstream from the prescribed upstream linear state. The double-integral term on the right-hand side of (9.3) is computed using the Newton and Cotes' integration formula (see Kopal 1961). The numerical computation starts about $\bar{x} = -15$ and the typical streamwise grid size is 0.01 (or 0.04 in the 51-pair-interaction case).

9.1. *Inviscid two-, three- and five-pair interactions*

The numerical solutions of (9.3) with (9.4) in the inviscid case ($\bar{\lambda} = 0$) are presented when the instability waves are composed of the frequency-detuned two, three and five pairs of oblique modes.

Figure 4 shows the results of nonlinear interaction between two pairs of oblique modes, i.e. $j = 0$ and 1, when the initial amplitudes are the same $\tilde{a}_0 = \tilde{a}_1 = 1$. The solution of the single-pair interaction is also plotted as the dotted curve. When the frequency-detuning factor $\bar{\chi}$ is equal to zero, the 0th and 1st amplitudes A_0 and A_1 become identical as shown in figure 4a. They become singular at earlier streamwise position than in the single-pair-interaction case because of the doubled self-interaction effect. This solution when $\bar{\chi} = 0$ is replotted as the dashed curve in figures 4b, 4c and 4d.

For the nonzero values of $\bar{\chi}$, the initially same linear amplitudes A_0 and A_1 start to diverge when the effects of the frequency-detuned self-interaction become large as shown in figures 4b and 4c for $\bar{\chi} = 2$ and 5, respectively. The multi-mode-coupling term $\mathcal{M}_s$ in (4.2) becomes $O(1)$ and the frequency-detuned oblique pairs start to interact nonlinearly when the local-growth-rate parameter σ^r becomes as large as the scaled Strouhal number difference $\bar{s}_1 - \bar{s}$ (that is equal to $(s_1 - s)/\sigma^2$, see (1.5)). When $\bar{\chi} = 2$ shown in figure 4b, the amplitudes A_0 and A_1 become nonlinearly interactive at earlier streamwise position (or at smaller growth rate) compared to the $\bar{\chi} = 5$ case (figure 4c). In figure 4c, the growth rate of $|A_0|$ in the streamwise region where $1 < \bar{x} < 3.3$ is enhanced mainly due to the self-interaction between the oblique modes of the 0th pair. Similarly, the self-interaction between the oblique modes of the 1st pair is responsible for the enhanced growth of $|A_1|$

there. Since the frequency detuning is relatively large ($\bar{\chi} = 5$), the coupled interaction between two pairs occurs in the later downstream region, $\bar{x} > 3.3$, where the growth rates become sufficiently large. Figures 4b and 4c show that $|A_0|$ is larger than $|A_1|$ (except $1 < \bar{x} < 3.3$ in figure 4c). The frequency of the 0th pair is lower than that of the 1st pair as given by (1.6).

When the frequency difference is very large, the coupled interaction between two oblique pairs does not occur until the growth rates also become very large. The results of $\bar{\chi} = 100$, given in figure 4d, show that $|A_0|$ and $|A_1|$ grow almost identically as in the single-pair-interaction case. The solid curve is not distinguishable from the dotted curve that is the solution of the single-pair interaction.

It can be observed in figure 4 that both amplitudes become singular at the same streamwise position for all values of $\bar{\chi}$. The frequency difference between two pairs delays the singularity.

The streamwise evolution of the oblique-mode amplitudes are plotted in figure 5 for the three-pair interaction when $j = 0$, 1 and 2. The results are independent of the specific value of j of the center frequency, thus, $j = -1$, 0 and 1 instead of the current choice will produce the same results as those in this figure. The initial amplitudes are the same, $\tilde{a}_0 = \tilde{a}_1 = \tilde{a}_2 = 1$, as in the two-pair-interaction case given in figure 4. The solution of the single-pair interaction is plotted as the dotted curve and that of the three-pair interaction with $\bar{\chi} = 0$ is plotted as the dashed curve. Similar to the results in figure 4, the coupled interaction between frequency-detuned pairs occurs at smaller amplitude when $\bar{\chi} = 2$ (figure 5a) than in the $\bar{\chi} = 5$ case (figure 5b). When $\bar{\chi} = 5$ the singularity occurs at later streamwise position compared to the case when $\bar{\chi} = 2$. The magnitude of the 0th amplitude $|A_0|$ (of the

lowest frequency) is the largest and that of the 2nd amplitude $|A_2|$ (of the highest frequency) is the smallest in the frequency-detuned nonlinear-interaction region. The amplitude of the lowest frequency, A_0, is likely to grow monotonically. The growth rate of $|A_2|$ in figure 5a becomes negative in a short period. It is interesting to observe in figure 5b that $|A_0|$ is almost identical to the single-pair solution, but $|A_1|$ and $|A_2|$ are smaller than that. In figure 5b, the singularity occurs at nearly the same position as that of the single-pair solution.

Figure 6 shows the results of the five-pair interaction when $\tilde{a}_0 = \tilde{a}_1 = \tilde{a}_2 = \tilde{a}_3 = \tilde{a}_4 = 1$ with the results of the single-pair interaction (dotted curve) and the five-pair interaction when $\tilde{\chi} = 0$ (dashed curve). The amplitude of the 0th pair $|A_0|$ is larger than the others, however, the highest-frequency amplitude $|A_4|$ is not necessarily the smallest one (cf. figure 5). The amplitude $|A_4|$ still belongs to the group of smaller amplitude in the frequency-detuned-interaction region. Note that when $\tilde{\chi} = 4$, shown in figure 6b, all amplitudes are smaller than the amplitude of the single-pair interaction and the singularity occurs even at later streamwise position than in the single-pair case. The singular point moves closer to that of the single-pair interaction for larger values of $\tilde{\chi}$ (the results are not shown). The solutions of ten-pair interaction show the similar behavior although the results are not presented.

Figure 7 shows the solutions of the two-pair interaction when the initial amplitude of the lower frequency ($\tilde{a}_0 = 1$) is larger than that of the higher frequency ($\tilde{a}_1 = 0.8$ and 0.5 for figures 7a and 7b, respectively) and $\tilde{\chi} = 2$. The single-pair solutions are plotted as the dotted curves for the respective initial amplitudes. (The dotted curve that has the same initial value as the curve (i) in figure 7a, for example, is the single-pair solution with $\tilde{a}_0 = 1$ and the other dotted curve is the single-pair solution with the initial amplitude of

0.8.) The frequency-detuned interaction between two pairs causes the growth rate of the higher-frequency pair to become negative in a short period in both cases. The magnitude of the 0th amplitude $|A_0|$ is always larger than $|A_1|$, but both amplitudes become singular at the same streamwise position.

The oblique-mode amplitudes are plotted in figure 8 when $\tilde{a}_1(=1)$ is larger than $\tilde{a}_0$, which is equal to 0.8 or 0.5, and $\bar{\chi}=2$. Since the frequency-detuned self-interaction between two pairs initially enhances the growth of the lower-frequency amplitude A_0 and reduces that of the higher-frequency amplitude A_1 (as in figure 4), $|A_0|$ becomes larger than $|A_1|$ in the later downstream region when $\tilde{a}_0=0.8$ and $\tilde{a}_1=1$ as shown in figure 8a.

The amplitudes A_0, A_1 and A_2 of the three-pair interaction plotted in figure 9 show that $|A_0|$ is always larger than $|A_2|$ although they have the same initial value ($\tilde{a}_0=\tilde{a}_2=0.7$ and 0.5; $\tilde{a}_1=1$). Figure 9a shows that the initially small 0th amplitude $|A_0|$ becomes larger than the 1st amplitude $|A_1|$ in the downstream region similar to the two-pair-interaction solutions given in figure 8a.

Figure 10 shows the effect of $\bar{\chi}$ on the streamwise evolution of the amplitudes in the three-pair-interaction case when $\tilde{a}_0=\tilde{a}_2=0.7$ and $\tilde{a}_1=1$. The single-pair-interaction solutions with the respective initial amplitudes are plotted as the dotted curves. The onset of the singularity is delayed as $\bar{\chi}$ is increased from 0 to 3 as shown in figure 10a. When $\bar{\chi}=5$, the singularity occurs at earlier streamwise position compared to the case when $\bar{\chi}=3$. The amplitude ratios $|A_0/A_1|$ and $|A_2/A_1|$ remained the same when $\bar{\chi}=0$. Figure 10e shows that the amplitude ratio of the higher-frequency mode $|A_2/A_1|$ is smaller in the downstream region than the upstream value of 0.7 for all $\bar{\chi}$ considered. The ratio $|A_0/A_1|$ for the lower-frequency mode becomes larger than the upstream value when $\bar{\chi}$ is equal

to 1, 2 or 3, but it becomes smaller than 0.7 when $\bar{\chi} = 5$ as shown in figure 10c. The amplitude $|A_2|$ of the higher-frequency pair exhibits more oscillatory behavior than $|A_0|$ of the lower-frequency pair as given in figures 10b and 10d.

9.2. *Inviscid 51-pair interaction*

The system of 51 frequency-detuned amplitude equations (9.3) where $J = 25$, i.e. $\jmath = -25, \ldots, 0, \ldots, 25$, are numerically solved when $\bar{\lambda} = 0$. As we mentioned before the specific value of $\jmath$ of the center pair (0 in this case) does not affect the results. The initial amplitudes $\tilde{a}_\jmath$ in (9.4) is given by the Gaussian function as

$$\tilde{a}_\jmath = \tfrac{9}{10} \exp\left[-(\jmath - n_1)^2/50\right] + \tfrac{1}{10} \quad \text{for} \quad -25 \leqslant \jmath \leqslant 25, \tag{9.5}$$

in the single-peak cases (figures 11 and 12). The second Gaussian function

$$\tilde{a}_\jmath = \tfrac{9}{10} C_2 \exp\left[-(\jmath - n_2)^2/50\right] + \tfrac{1}{10}, \tag{9.6}$$

is superimposed on top of (9.5) for the initial amplitudes in the double-peak cases presented in figures 13 to 15.

The Strouhal number difference between the $\jmath$th and the 0th pairs of oblique modes is, from (1.6) and (1.12),

$$\bar{s}_\jmath - \bar{s} = \sigma^r \jmath \bar{\chi} \hat{\kappa} \tau_w \bar{s}, \tag{9.7}$$

where $\hat{\kappa}$ is given by (9.1).

Figure 11 shows the numerical solutions when $\bar{\chi}$ is 0.2 and n_1 in (9.5) is zero. The magnitude of the amplitudes $|A_\jmath|$ versus $\jmath$ at different streamwise positions are plotted in figure 11a. The streamwise evolution of the magnitude of the -20th, -10th, 0th, 10th and 20th amplitudes, $|A_{(-20)}|$, $|A_{(-10)}|$, $|A_0|$, $|A_{10}|$ and $|A_{20}|$, respectively, is plotted in figure 11b.

Figures 11a and 11b show that the amplitudes of the instability waves, especially those of the lower-frequency modes (i.e. with smaller j), are greatly enhanced due to the frequency-detuned self-interaction. The initially very small amplitudes of the -25th to -15th pairs become large as the instability waves evolve downstream. The ratio $|A_{(-15)}/A_{(-25)}|$, which is nearly equal to one in the upstream region, becomes large in the downstream region. The initial symmetric shape of the Gaussian function becomes asymmetric and the maximum amplitude occurs at lower frequency (at $j = -2$ when $\bar{x} \geqslant 1$) in the downstream region. In the upstream positions, up to about $\bar{x} = 0.5$, the magnitude of the -20th amplitude is nearly equal to that of the 20th pair as shown in figure 11b. However, at later downstream positions (for example, at $\bar{x} = 2.52$ and 2.96), $|A_{(-20)}|$ becomes much larger than $|A_{20}|$ as well as $|A_{(-10)}|$ becomes larger than $|A_{10}|$ as given in figure 11a. The amplitude $|A_{20}|$ is still larger than the linear one at these two downstream positions (figure 11b). All amplitudes become singular at the same finite downstream position.

The effect of larger frequency-detuning factor is shown in figure 12 when $\bar{\chi} = 0.5$ and $n_1 = 0$. Because of the larger detuning, the frequency-detuned nonlinear interaction occurs at later downstream position in figure 12b compared to the previous $\bar{\chi} = 0.2$ case given in figure 11b. Figure 12a shows that the frequency-detuned interactions enhance the growth of the lower-frequency pairs more than that of the higher-frequency pairs similar to the previous results. The frequency where the maximum amplitude occurs becomes lower as the oblique modes evolve downstream. The amplitudes become singular at later downstream position compared to the smaller frequency-detuning-factor case given in figure 11.

Figure 13 shows the evolution of the double-peak initial amplitudes when $\bar{\chi} = 0.2$, $n_1 = 5$, $n_2 = -5$ and $C_2 = 1$. The amplitude $|A_{(-5)}|$ is equal to $|A_5|$ in the upstream

region, but the former becomes larger than the latter in the downstream region. The amplitude of the -6th pair is the largest at $\bar{x} = 2.8$. Figure 14 shows the results when the higher-frequency maximum of the initial amplitude, $\tilde{a}_5$, is larger than the lower-frequency one, $\tilde{a}_0$, and $\bar{\chi} = 0.2$, $n_1 = 5$, $n_2 = 0$ and $C_2 = 0.8$. Although the 0th amplitude is smaller than the 5th amplitude in the upstream region, $|A_0|$ eventually becomes larger than $|A_5|$ in the later stage as was also observed in figure 8 in the two-pair interaction. Figure 15, which are the numerical results when $\bar{\chi} = 0.2$, $n_1 = 0$, $n_2 = 5$ and $C_2 = 0.8$, shows that the initially small higher-frequency peak (at $j = 5$) becomes less and less noticeable as the instability modes evolve downstream. The results in figures 13 to 15 also exhibit the enhanced growth of the lower-frequency pairs.

The results of these frequency-detuned multi-pair interactions show that all instability modes become singular at the same finite downstream position. However, as we all know, the flow does not support extremely large instability waves. Near the singular point (where $x_s - x = O(\sigma^{-1})$), the amplitudes of the instability modes become as large as the base mean flow in the inviscid wall layer (see (I.5.30) and (5.1)). The next stage will be the triple-deck stage as shown by Goldstein & Lee (1992) and Wu *et al.* (1997). The flow in this stage is governed by the equations which are elliptic in the streamwise direction. The flow may enter the triple-deck stage before we can fully observe the explosive growth of the instability modes predicted by the frequency-detuned non-equilibrium amplitude equations of this analysis. The explosive growth occurs in a very short streamwise distance as the numerical results indicate.

9.3. *Critical-layer jumps of the nonlinearly-generated low-frequency modes*

When $\bar{\lambda} = 0$, the velocity jumps across the critical layer of the low-frequency modes, (7.1) and (7.2) can be rewritten as

$$\Delta U^{(2)}_{0,2;\jmath,\ell} = -\tfrac{3}{2}\pi \int_{-\infty}^{\bar{x}} dx_1 (\bar{x} - x_1)^2 A_{\jmath+\ell}(x_1) A^*_\ell(x_1), \tag{9.8}$$

$$\Delta V^{(2)}_{0,2;\jmath,\ell} = 3\mathrm{i}\pi \int_{-\infty}^{\bar{x}} dx_1 (\bar{x} - x_1) A_{\jmath+\ell}(x_1) A^*_\ell(x_1), \tag{9.9}$$

where we have used (9.2). The jumps $\Delta U^{(2)}_{0,2;\jmath,\ell}$ and $\Delta V^{(2)}_{0,2;\jmath,\ell}$ are obtained by integrating (9.8) and (9.9) using the numerically calculated oblique-mode amplitudes $A_\jmath$.

Figure 16 shows the numerical results of the single-pair interaction when $\tilde{a}_0 = 1$. The nonlinear interaction between a pair of oblique modes of the same frequency produces the steady spanwise-periodic mode. The oblique mode amplitude A_0 that was plotted as the dotted curve in figure 4 is replotted as the same dotted curve. The streamwise growth rates of $\Delta U^{(2)}_{0,2;0,0}$ and $\Delta V^{(2)}_{0,2;0,0}$ are twice that of the oblique mode in the linear upstream region as given by (7.11). Both streamwise and transverse jumps of the spanwise-periodic mean-flow distortion become singular at the same singular point of the oblique-mode amplitude.

The nonlinear interaction in the critical layer between three frequency-detuned pairs of oblique modes produces nine low-frequency (spanwise-periodic) modes. The numerical results of the three-pair interaction when $\tilde{a}_0 = \tilde{a}_1 = \tilde{a}_2 = 1$ are given in figure 17 for $\bar{\chi} = 2$ and in figure 18 for $\bar{\chi} = 5$. The streamwise evolution of the amplitudes was plotted in figure 5. If we put the subscripts $\jmath$ of $A_\jmath$ to be 0, 1 and 2, we can show from (7.6) and (7.7) that the subscripts $(\jmath, \ell)$ of the non-zero $\Delta U^{(2)}_{0,2;\jmath,\ell}$ and $\Delta V^{(2)}_{0,2;\jmath,\ell}$ are (-2,2), (-1,1), (-1,2), (0,0), (0,1), (0,2), (1,0), (1,1) and (2,0). Figures 17 and 18 show that $|\Delta U^{(2)}_{0,2;\jmath,\ell}|$ and $|\Delta V^{(2)}_{0,2;\jmath,\ell}|$ with larger value of $|\jmath|$ are smaller than those with smaller $|\jmath|$ in the linear upstream region

as was predicted by (7.11). The mode with $\jmath = \ell = 0$ is steady and its critical-layer jump is larger than the other components in most of the region. As in figure 5 the results in these figures are independent of the specific value of $\jmath$ of the center frequency.

10. Concluding remarks

A system of resonant-triads can interact nonlinearly between themselves in the common critical layer if their frequencies (of the fundamental plane waves) are different by a factor whose magnitude is of the order of the growth rate multiplied by the wavenumber of the instability waves. The long-wavelength small-growth-rate instability modes in boundary layers with and without mean pressure gradient are analyzed using the generalized scaling of Lee (1997a).

In this part of the study, the system of partial differential critical-layer equations along with the jump equations given in §7 of Part 1 is solved analytically to obtain the frequency-detuned amplitude equations. The amplitude equations are similar to those obtained by Goldstein & Lee (1992) and Wu (1992) for the single resonant-triad interaction. However, in the multi-resonant-triad-interaction case, the frequency-detuned self-interaction term in the oblique-mode amplitude equation and the frequency-detuned mutual-interaction term in the plane-wave amplitude equation are composed of $2(2J+1)$ terms (see (3.1) and (3.2)). The kernel functions for the self-interaction terms are divided into two parts.

When the scaled-Strouhal-number difference between resonant-triads is larger than the local-growth-rate parameter σ^r, the multi-mode-coupling terms $\mathcal{M}_s$, $\mathcal{M}_m$ and $\mathcal{M}_b$ in (4.2) and (4.3) become negligibly small (see (4.7) and (4.8)) and the instability waves of an individual resonant-triad grow independently of the other resonant-triads.

The effect of the self-interaction between frequency-detuned pairs of oblique modes was investigated by solving the non-equilibrium oblique-mode amplitude equations in the inviscid limit. As given in the previous section, the growth of the lower-frequency oblique mode is more enhanced than that of the higher-frequency in most cases. It is shown that all amplitudes become singular at the same finite downstream position regardless of their initial values. The frequency-detuning effect delays the occurrence of the singularity. The singularity in an appropriately frequency-detuned multi-pair interaction occurs even at later downstream position than in the single-pair interaction although the sum of the initial amplitudes in the former case is much larger than in the latter case.

Though the analysis was carried out with the non-equilibrium critical-layer scalings, the frequency-detuned quasi-equilibrium amplitude equations can be obtained by taking the viscous limit of the $O(1)$-viscosity non-equilibrium amplitude equations. The numerical computation of the quasi-equilibrium equations shows that the saturation amplitude of the oblique mode of lower frequency is larger than that of higher frequency. The frequency-detuned resonant-triads of the Tollmien-Schlichting waves in the initial critical-layer stage is governed by the quasi-equilibrium amplitude equations, however, the later downstream stage will be eventually governed by the non-equilibrium dynamics as shown by Goldstein (1994), Wu *et al.* (1997) and Lee (1997a).

Corke & Gruber (1996) and Liu & Maslowe (1998) show that the resonant-triad theory of Goldstein & Lee (1992) is in good agreement with their experimental and numerical results in adverse-pressure-gradient boundary layers. Corke & Gruber (1996) show that faster linear growth of the plane wave accelerates the parametric-resonance growth of the subharmonic oblique modes and induces larger saturation amplitudes of the oblique modes

compared to the Blasius case given in Corke & Mangano (1989). Using the parameters in Corke & Gruber (1996), we can show that the parametric-resonance effect is already much larger than the linear-growth effect (in the oblique-mode amplitude equation) at their first measured streamwise position. Faster (than linear) growth of the oblique modes at the beginning was observed in the experiments and also confirmed by the numerical simulations of Liu & Maslowe (1998).

The numerical solutions of the non-equilibrium amplitude equations show that the explosive growth of the instabilities occurs in a very short streamwise period near the singular point. Therefore, in most flow conditions for the resonant-triad interaction, the explosive growth may not be clearly distinguishable before the scalings of this analysis break down as the experimental (Corke & Gruber 1996) and numerical (Liu & Maslowe 1998) results indicate. However, the enhanced growth of the plane wave, especially in Figure 10b of Corke & Gruber (1996), proves that the oblique modes are large enough to produce the mutual-interaction and back-reaction effects on the plane wave, thus, there exists self-interaction effect. The explosive growth is the downstream asymptotic behavior of the self-interaction (or fully-coupled interaction) effect. In fact, as the finite-viscosity numerical solutions of Lee (1997a) (for example, his Figures 3 and 4) show, the fully-coupled interaction initially, in a very short period, reduces the growth rates of the oblique modes, which is more apparent when the viscous effect is large. The self-interaction effect can also be identified by the spanwise-periodic wall shear stress and the generation of the spanwise-periodic mean-flow distortion and nonlinear (very) low-frequency modes. The saturation of amplitudes, shown both experimentally (Corke & Gruber 1996) and numerically (Liu & Maslowe 1998), will be governed by subsequent nonlinear dynamics but the frequency-detuned self-interaction

between saturating/saturated oblique modes and neighboring frequencies (of small amplitudes) may still be active there to accelerate the growth of the latter.

The present analysis is more focused on the frequency-detuned self-interaction and the summation does not appear in the parametric-resonance term in the oblique-mode amplitude equation (3.1). We can extend the analysis, by relaxing the condition (I.5.16), to include the spanwise-wavenumber detuning. It can be shown that the parametric-resonance interaction between a band of fundamental plane waves ($\omega \pm \Delta\omega_f$) and a band of subharmonic oblique modes ($\omega/2 \pm \Delta\omega_s$) can accelerate the growth of the oblique modes whose frequencies are within $\omega/2 \pm (\Delta\omega_f + \Delta\omega_s)$. The growth of a wide frequency range of oblique modes will be enhanced by subsequent interactions, for example, between the plane waves and the oblique modes of $\omega/2 \pm (\Delta\omega_f + \Delta\omega_s)$. Kachanov & Levchenko (1984) (also in the review by Kachanov 1994) showed that the (subharmonic) resonance is very wide in the frequency spectrum and it can amplify even (quasi-)subharmonic modes whose frequency detuning is close to one half the subharmonic frequency.

In an incompressible boundary layer, the plane wave is the most unstable mode. However, three-dimensional modes of small propagation angles are more unstable than the plane wave off the most unstable frequency (see (3.13)). Therefore, in a natural flow, the linear upstream flow may be dominated by an oblique mode whose propagation angle is relatively small. The resonant-triad analysis of this paper (also of Goldstein & Lee 1992, Wu 1992 and Lee 1997a) can be generalized for three (pairs of) oblique modes instead of the usual fundamental plane wave and a pair of subharmonic oblique modes. The three (pairs of) oblique modes, whose streamwise and spanwise wavenumbers are $\alpha_\imath/2$ and $\beta_\imath$, respectively, share the same critical layer, provided $(\alpha_\imath/2)^2 + \beta_\imath^2$ are the same for all $\imath = 1, 2$ and

3. If we put the propagation angle of the first mode to be θ_1 ($\equiv \tan^{-1}(2\beta_1/\alpha_1)$), where $0 \leqslant \theta_1 < \pi/6$, the second and third ones must be $\theta_2 = \pi/3 - \theta_1$ and $\theta_3 = \pi/3 + \theta_1$ in order for the resonance-interaction to occur. When θ_1 is equal to zero, θ_2 and θ_3 become $\pi/3$ and the three-oblique-pair resonant-triad reduces to the traditional resonant-triad. The role of the first oblique mode is similar to that of the plane wave. When the amplitude of the first mode becomes $O(\sigma^{4r+1})$, the (generalized-)parametric-resonance interaction enhances the growth of the second and third modes as in the subharmonic-resonance analysis of this paper. The frequency difference between the second and third modes becomes larger as the propagation angle of the first mode θ_1 is increased. (This phenomenon may be very useful to prove the existence of the critical-layer dynamics in boundary layers and free shear flows.) When there exist three pairs of oblique modes of different frequencies in a natural flow, a clear Λ-shaped structure is hard to be observed as many unexcited flow-visualization experiments report.

The (generalized-)parametric-resonance growth of the second and third oblique modes allows the phase-locked interaction of Wu & Stewart (1996) to occur when their amplitudes become $O(\sigma^{7r/2+1})$. The phase-locked interaction can take place between the second (or third) mode and any other lower-frequency oblique modes of the same phase speed. The analysis of Wu & Stewart (1996) indicate that the higher-frequency mode (i.e. the 2nd or 3rd mode) can accelerate the growth of the lower-frequency ones. This phase-locked interaction occurs earlier than the self-interaction. Both in parametric-resonance and phase-locked stages, the first mode grows linearly. When the second and third modes become sufficiently large, i.e. $O(\sigma^{3r+1})$, due to the continuous parametric-resonance interaction with the first mode, the frequency-detuned self-interaction of this analysis becomes important and all

oblique modes become singular at a finite downstream position.

It is shown in Appendix C that higher spanwise-harmonics ($\Delta U_{1,3}^{(3)}$), higher spanwise-periodic mean-flow distortion ($\Delta U_{0,4}^{(4)}$) and nonlinear mean flow ($\Delta U_{0,0}^{(4)}$), which do not exist in the upstream region, are nonlinearly generated by the critical-layer interaction and they grow very rapidly to become as large as the base mean flow in the inviscid wall layer at the downstream position where the distance from the singularity $\bar{x}_s - \bar{x}$ is of $O(\sigma^r)$. The mean flow jump across the critical layer was found by Haberman (1972). It is also possible to show that the nonlinear interaction in the critical layer generates the critical-layer jumps of all higher harmonics and they also become of $O(\sigma)$ very fast in the inviscid wall layer (cf. Smith & Bodonyi 1982).

The present critical-layer analysis shows that (i) a band of (or bands of a couple of) two-dimensional (or small-propagation-angle oblique) modes, which dominate the upstream region of a boundary-layer-transition process especially when environmental disturbances are relatively small, (ii) bands of oblique modes, whose growth is accelerated by subharmonic-parametric-resonance, generalized-parametric-resonance and phase-locked interactions, (iii) nonlinearly-generated low-frequency modes, which includes the spanwise-periodic mean-flow distortion, (iv) nonlinear mean flow and (v) bands of higher harmonics become very large as the instabilities evolve downstream. The growth of these linear and nonlinear modes are still governed by the parabolic-type (in the streamwise direction) equations of this analysis. The frequency-detuning interaction allows wider bands of modes to interact.

Near the singularity where $\bar{x}_s - \bar{x}$ is of $O(\sigma^r)$, or $x_s - x$ is of $O(\sigma^{-1})$, all these instabilities become as large as the base mean flow in the inviscid wall layer. The flow in the inviscid wall layer will then be fully nonlinear. Goldstein & Lee (1992) and Wu *et al.* (1997) showed

that the flow in the next stage will be governed by the unsteady, inviscid, three-dimensional triple-deck equations.

This work was supported by the Acoustics Branch at NASA Lewis Research Center, contract number NAS3-98008.

Appendix A. The $O(1)$-viscosity kernel functions K_2, K_3, K_4 and K_5

$$K_2 = e^{-\bar{\lambda}(2\zeta_1/3+\zeta_2)\zeta_1^2}\left[\zeta_1^3 - 2h_s\int_0^{\zeta_1} d\zeta_3\left\{e^{-\bar{\lambda}\left[(\zeta_1+2\zeta_2/3)\zeta_2^2+(\zeta_1+\zeta_2)(2\zeta_2+\zeta_3)\zeta_3\right]}\left(\hat{g}_a(\zeta_1,\zeta_2,\zeta_3)\right.\right.\right.$$
$$\left.\left.\left.+\mathcal{F}_a^-(\zeta_1,\zeta_2,\zeta_3|0,0)\right) - \hat{g}_c(\zeta_1,\zeta_2,\zeta_3)\left(\hat{g}_b(\zeta_1,\zeta_2,\zeta_3)+\mathcal{F}_a^+(\zeta_1,\zeta_2,\zeta_3|\zeta_1,0)+\zeta_1\zeta_2\right)\right\}\right], \quad \text{(A 1)}$$

$$K_3 = e^{-\bar{\lambda}(2\zeta_1/3+\zeta_2)\zeta_1^2}\left[(\zeta_1+\zeta_2)\,\zeta_1^2 + 2h_s\int_0^{\zeta_2} d\zeta_3 e^{-\bar{\lambda}(2\zeta_3/3+\zeta_1)\zeta_3^2}\zeta_1\,(\zeta_1+2\zeta_2-2\zeta_3)\right.$$
$$-2h_s\int_0^{\zeta_1} d\zeta_3\left\{e^{-\bar{\lambda}\zeta_1\zeta_3^2}\left(\hat{g}_a(\zeta_1,\zeta_2,\zeta_3)+\mathcal{F}_a^-(\zeta_1,\zeta_2,\zeta_3|0,\zeta_2)\right) - \hat{g}_c(\zeta_1,\zeta_2,\zeta_3)\left(\hat{g}_b(\zeta_1,\zeta_2,\zeta_3)\right.\right.$$
$$\left.\left.\left.+\mathcal{F}_a^+(\zeta_1,\zeta_2,\zeta_3|\zeta_1,0)+2\zeta_2\zeta_3-\zeta_1\zeta_2\right)\right\}\right], \quad \text{(A 2)}$$

$$K_4 = e^{-4\bar{\lambda}(\zeta_1+\zeta_2)\zeta_1^2}\left[2\zeta_1^3 + h_s e^{-2\bar{\lambda}(\zeta_1+\zeta_2/3)\zeta_2^2}\left\{\tfrac{4}{9}\zeta_1\,(3\zeta_1+2\zeta_2)\,(9\zeta_1+5\zeta_2)\right.\right.$$
$$\left.\left.+\tfrac{2}{3}\zeta_2\mathcal{F}_b^-(\zeta_1,\zeta_2,\zeta_3|0,\zeta_2,\zeta_3;3)+2\,(2\zeta_1+\zeta_2)\,\mathcal{F}_b^+(\zeta_1,\zeta_2,\zeta_3|\zeta_1,\zeta_2,0;1)\right\}\right], \quad \text{(A 3)}$$

$$K_5 = e^{-(2/3)\bar{\lambda}\left[(2\zeta_1+\zeta_2)^3-2\zeta_1^3\right]}(2\zeta_1+\zeta_2)\left[\zeta_1\,(\zeta_1+\zeta_2)+h_s\left\{3\zeta_1\,(2\zeta_1+\zeta_2)\right.\right.$$
$$\left.\left.+2\mathcal{F}_b^+(\zeta_1,\zeta_2,\zeta_3|\zeta_1,0,0;1)\right\}\right], \quad \text{(A 4)}$$

where we have put, as in (2.3),

$$\zeta_1 \equiv \bar{x} - x_1, \quad \zeta_2 \equiv x_1 - x_2, \quad h_s \equiv \tau\sin^2\theta, \quad \text{(A 5)}$$

with

$$\mathcal{F}_a^{\pm}(\zeta_1,\zeta_2,\zeta_3|\zeta_a,\zeta_b) \equiv 4h_s \int_0^{\zeta_3+\zeta_b} d\zeta_4 e^{\pm\bar{\lambda}(2\zeta_4/3+\zeta_1+\zeta_2-\zeta_a-\zeta_b)\zeta_4^2} (\zeta_b+\zeta_3-\zeta_4) \left[1+2\bar{\lambda}(\zeta_1-\zeta_3)(\zeta_2+\zeta_3+\zeta_a-\zeta_b)^2\right], \quad \text{(A 6)}$$

$$\mathcal{F}_b^{\pm}(\zeta_1,\zeta_2,\zeta_3|\zeta_a,\zeta_b,\zeta_c;\hat{a}) \equiv \int_0^{\zeta_1} d\zeta_3 e^{\pm 2\hat{a}\bar{\lambda}/3\left[(\zeta_3\mp 3\zeta_1)\zeta_3^2+2\zeta_2\zeta_c^2\mp(3/\hat{a})(2\zeta_1+\zeta_2)\zeta_b\zeta_3\right]} \left[\zeta_1-\zeta_3 - \frac{2}{\hat{a}}(2\zeta_a+\zeta_2)\left\{1+\bar{\lambda}(\zeta_1-\zeta_3)(3\zeta_1+2\zeta_b-\zeta_3+4\zeta_c)(2\zeta_1-2\zeta_a+\zeta_b+\zeta_3)\right\}\right], \quad \text{(A 7)}$$

$$\hat{g}_a \equiv (\zeta_1-\zeta_3)(\zeta_1+2\zeta_2+3\zeta_3), \quad \text{(A 8)}$$

$$\hat{g}_b \equiv 2\bar{\lambda}\zeta_2\zeta_3(\zeta_1-\zeta_3)(\zeta_1+\zeta_2+\zeta_3)^2, \quad \text{(A 9)}$$

$$\hat{g}_c \equiv \exp\left[-\bar{\lambda}\left\{(\zeta_1+2\zeta_2/3)\zeta_2^2+(2\zeta_1+3\zeta_2+4\zeta_3/3)\zeta_3^2+2(\zeta_1+\zeta_2)\zeta_2\zeta_3\right\}\right]. \quad \text{(A 10)}$$

Appendix B. The integrals D_p, D_s and D_m in (5.2) and (5.3)

$$D_p = \int_1^{\infty} dx_1 (x_1-1)^2 (x_1)^{-4-2\mathrm{i}\psi_j} (2x_1-1)^{-3+\mathrm{i}\psi_j}, \quad \text{(B 1)}$$

$$D_s = \int_1^{\infty} dx_1 \int_{x_1}^{\infty} dx_2 (x_1-1)(x_1+x_2-1)^{-3+\mathrm{i}\psi_\ell} \left[(x_1-1)^2 (x_1)^{-3-\mathrm{i}\psi_j} (x_2)^{-3-\mathrm{i}\psi_\ell} + (x_2-1)\left\{x_1-1-2\tau(\sin^2\theta)(x_1-x_2)\right\}(x_1)^{-3-\mathrm{i}\psi_\ell}(x_2)^{-3-\mathrm{i}\psi_j}\right], \quad \text{(B 2)}$$

$$D_m = \int_1^{\infty} dx_1 \int_{x_1}^{\infty} dx_2 (x_1-1)\left[2(x_1-1)^2 (x_1)^{-4-2\mathrm{i}\psi_j}(x_2)^{-3-\mathrm{i}\psi_\ell}(2x_1+x_2-2)^{-3+\mathrm{i}\psi_\ell} + (x_2-1)(x_1+x_2-2)(x_1)^{-3-\mathrm{i}\psi_\ell}(x_2)^{-4-2\mathrm{i}\psi_j}(x_1+2x_2-2)^{-3+\mathrm{i}\psi_\ell}\right]. \quad \text{(B 3)}$$

Appendix C. Critical-layer jumps of higher-order nonlinear modes

Nonlinear critical-layer equation (I.6.3) indicates that the third-order nonlinear mode $\mathrm{Re}\,\tilde{U}_{1,3}^{(3)} e^{\mathrm{i}(X/2\pm 3Z)}$ appears in the expansion (I.6.15) and the fourth-order ones $\mathrm{Re}\,\tilde{U}_{0,0}^{(4)}$ and

$\mathrm{Re}\tilde{U}^{(4)}_{0,4}e^{i4Z}$, among many others, also appear in (I.6.16) (also in equation (6.12) in Lee 1997a). Here we only consider the single-resonant-triad interaction case ($J = \bar{\chi} = 0$ and $\eta_o = 0$) and A_j will be replaced by A.

From the critical-layer analysis, we can show that

$$\Delta U^{(3)}_{1,3}(\bar{x}) \equiv \int_{-\infty}^{\infty} U^{(3)}_{1,3\eta} d\eta = \pi \int_{-\infty}^{\bar{x}} dx_1 \int_{-\infty}^{x_1} dx_2 A(x_1)A(x_2)A^*(x_1+x_2-\bar{x}) \\ e^{-\bar{\lambda}\zeta_1^2(2\zeta_1/3+\zeta_2)}\left[\zeta_1^2(2\zeta_1+\zeta_2) + (\sin^2\theta)(\ldots) + (\sin^4\theta)(\ldots)\right], \qquad (C\,1)$$

$$\Delta U^{(4)}_{0,0}(\bar{x}) \equiv \int_{-\infty}^{\infty} U^{(4)}_{0,0\eta} d\eta = \pi \int_{-\infty}^{\bar{x}} dx_1 |A(x_1)|^2 \left[1 - \tau(\sin^2\theta)e^{-2\bar{\lambda}\zeta_1^3/3}\right], \qquad (C\,2)$$

$$\Delta U^{(4)}_{0,4}(\bar{x}) \equiv \int_{-\infty}^{\infty} U^{(4)}_{0,4\eta} d\eta = -16\pi \int_{-\infty}^{\bar{x}} dx_1 \int_{-\infty}^{x_1} dx_2 \int_{-\infty}^{x_2} dx_3 \int_{-\infty}^{x_3} dx_4 \\ \left[A^*(x_2)A(x_3)A(x_4)A^*(x_3+x_4-x_2)(\zeta_1\zeta_3^2+\ldots)+\ldots\right], \qquad (C\,3)$$

where

$$U^{(3)}_{1,3} = \frac{\bar{\beta}H}{\hat{\kappa}\tau_w\bar{\gamma}}\left(\frac{2\pi\bar{\alpha}}{\tau_w\bar{c}}\right)^{1/2}\tilde{U}^{(3)}_{1,3}e^{iX_o/2}, \quad U^{(4)}_{0,0} = \frac{H}{2\hat{\kappa}^2\tau_w^2}\tilde{U}^{(4)}_{0,0}, \quad U^{(4)}_{0,4} = \hat{\kappa}\tau_w\bar{c}H^2\tilde{U}^{(4)}_{0,4}, \qquad (C\,4)$$

$$H \equiv 2\pi Y_c\bar{\alpha}/(\hat{\kappa}\tau_w\bar{c})^3, \qquad (C\,5)$$

$$\zeta_3 \equiv x_2 - x_3, \qquad (C\,6)$$

ζ_1 and ζ_2 are defined in (2.3) and M is defined in (I.7.5).

The nonlinear modes $\sigma^{4r+1}\mathrm{Re}\bar{U}^{(3)}_{1,3}e^{iX/2}\cos 3Z$, $\sigma^{5r+1}\bar{U}^{(4)}_{0,0}$ and $\sigma^{5r+1}\bar{U}^{(4)}_{0,4}\cos 4Z$ should be included in the streamwise velocity expansion (1.10) in order to match with these critical-layer jumps. Near the singular point, the amplitude A is given by (5.1). Thus, these higher-order velocities become as large as the base mean flow, which is $O(\sigma)$, in the inviscid wall layer when $\bar{x}_s - \bar{x}$ is $O(\sigma^r)$.

References

[1] ABRAMOWITZ, M. & STEGUN, I.A. 1965 *Handbook of Mathematical Functions with Formulas, Graphs, and Mathematical Tables.* Dover Publications, Inc.

[2] BUTKOV, E. 1968 *Mathematical Physics.* Addison-Wesley Publishing Company.

[3] CORKE, T.C. & GRUBER, S. 1996 Resonant growth of three-dimensional modes in Falkner-Skan boundary layers with adverse pressure gradients. *J. Fluid Mech.* **320**, 211-233.

[4] CORKE, T.C. & MANGANO, R.A. 1989 Resonant growth of three-dimensional modes in transitioning Blasius boundary layers. *J. Fluid Mech.* **209**, 93-150.

[5] GEAR, C.W. 1971 *Numerical Initial Value Problems in Ordinary Differential Equations.* Prentice-Hall.

[6] GOLDSTEIN, M.E. 1994 Nonlinear interactions between oblique instability waves on nearly parallel shear flows. *Phys. Fluids* **6**, 724-735.

[7] GOLDSTEIN, M.E. & CHOI, S.W. 1989 Nonlinear evolution of interacting oblique waves on two–dimensional shear layers. *J. Fluid Mech.* **207**, 97-120. Also Corrigendum, *J. Fluid Mech.* **216**, 659-663.

[8] GOLDSTEIN, M.E. & LEE, S.S. 1992 Fully coupled resonant-triad interaction in an adverse-pressure-gradient boundary layer. *J. Fluid Mech.* **245**, 523-551.

[9] GOLDSTEIN, M.E. & LEE, S.S. 1993 Oblique instability waves in nearly parallel shear flows, in *Nonlinear Waves and Weak Turbulence with Applications in Oceanography*

and Condensed Matter Physics, (eds. Fitzmaurice, N., Gurarie, D., McCaughan, F. & Woyczynski, W.), Birkhauser, 159-177.

[10] HABERMAN, R. 1972 Critical layers in parallel flows. *Stud. Appl. Math.* **51**, 139-161.

[11] KACHANOV, Y.S. 1994 Physical mechanisms of laminar-boundary-layer transition. *Annu. Rev. Fluid Mech.* **26**, 411-482.

[12] KACHANOV, Y.S. & LEVCHENKO, V.Y. 1984 The resonant interaction of disturbances at laminar-turbulent transition in a boundary layer. *J. Fluid Mech.* **138**, 209-247.

[13] KOPAL, Z. 1961 *Numerical Analysis*, 2nd edn. Chapman & Hall.

[14] LEE, S. S. 1997a Generalized critical-layer analysis of fully coupled resonant-triad interactions in boundary layers. *J. Fluid Mech.* **347**, 71-103.

[15] LEE, S. S. 1997b Generalized critical-layer analysis of instability waves in boundary layers. *Bulletin of the American Physical Society, Series II*, **42**, 2121.

[16] LEE, S. S. 1997c Spanwise periodic mean flow generated by nonlinear interaction between oblique instability waves. *Bulletin of the American Physical Society, Series II*, **42**, 2155.

[17] LEE, S. S. 1998a Nonlinear evolution of instability waves in boundary layers. *AIAA Paper*, AIAA-98-2862.

[18] LEE, S. S. 1998b Nonlinear interaction of detuned instability waves in boundary-layer transition: 1. Resonant-triad interaction. *NASA/CR 1998-207938.*

[19] LIGHTHILL, M.J. 1960 *Introduction to Fourier Analysis and Generalized Functions.* Cambridge University Press.

[20] LIU, C. & MASLOWE, S.A. 1998 A numerical investigation of resonant interactions in adverse pressure gradient boundary layers. *Submitted to J. Fluid Mech.*.

[21] MANKBADI, R.R., WU, X. & LEE, S.S. 1993 A critical-layer analysis of the resonant triad in boundary-layer transition: nonlinear interactions. *J. Fluid Mech.* **256**, 85-106.

[22] SMITH, F.T. & BODONYI, R.J. 1982 Nonlinear critical layers and their development in streaming-flow stability. *J. Fluid Mech.* **118**, 165-185.

[23] WU, X 1992 The nonlinear evolution of high-frequency resonant-triad waves in an oscillatory Stokes layer at high Reynolds number. *J. Fluid Mech.* **245**, 553-597.

[24] WU, X 1993 On critical-layer and diffusion-layer nonlinearity in the three-dimensional stage of boundary-layer transition. *Proc. R. Soc. Lond. A* **443**, 95-106.

[25] WU, X 1995 Viscous effects on fully coupled resonant-triad interactions: an analytical approach. *J. Fluid Mech.* **292**, 377-407.

[26] WU, X., LEE, S.S. & COWLEY, S.J. 1993 On the weakly nonlinear three-dimensional instability of shear layers to pairs of oblique waves: the Stokes layer as a paradigm. *J. Fluid Mech.* **253**, 681-721.

[27] WU, X., LEIB, S.J. & GOLDSTEIN, M.E. 1997 On the nonlinear evolution of a pair of oblique Tollmien-Schlichting waves in boundary layers. *J. Fluid Mech.* **340**, 361-394.

[28] WU, X. & STEWART, P.A. 1996 Interaction of phase-locked modes: a new mechanism for the rapid growth of three-dimensional disturbances. *J. Fluid Mech.* **316**, 335-372.

[29] WUNDROW, D.W, HULTGREN, L.S. & GOLDSTEIN, M.E. 1994 Interaction of oblique instability waves with a nonlinear plane wave. *J. Fluid Mech.* **264**, 343-372.

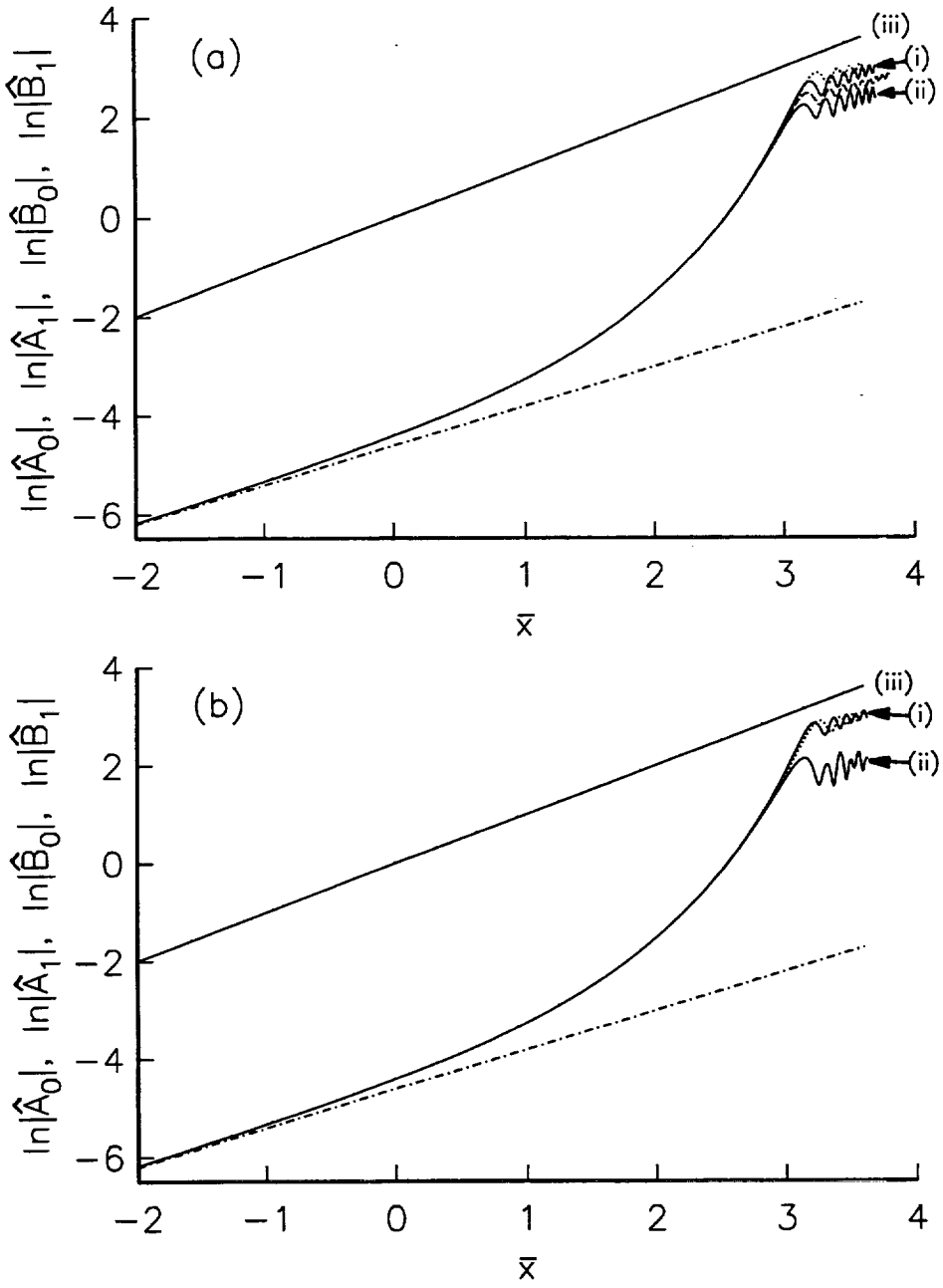

Fig. 1 Quasi-equilibrium interaction between two resonant-triads: $\ln|\hat{A}_0|$, $\ln|\hat{A}_1|$ and $\ln|\hat{B}_0| = \ln|\hat{B}_1|$ *vs.* $\bar{x}$, curves (i), (ii) and (iii) respectively, when $\hat{a}_0 = \hat{a}_1 = 0.01\exp(\mathrm{i}\pi/4)$, $\hat{b}_0 = \hat{b}_1 = 1$, $\hat{\lambda} = 1$, $\hat{\kappa}_{ob} = 4/5$, $\hat{\kappa}_{2d} = 1$ and (a) $\bar{\chi} = 5$, (b) $\bar{\chi} = 10$, (c) $\bar{\chi} = 50$ and (d) $\bar{\chi} = 500$ (dotted, single resonant-triad interaction; dashed, two resonant-triad interaction with $\bar{\chi} = 0$; dot-dashed, linear oblique-mode amplitude).

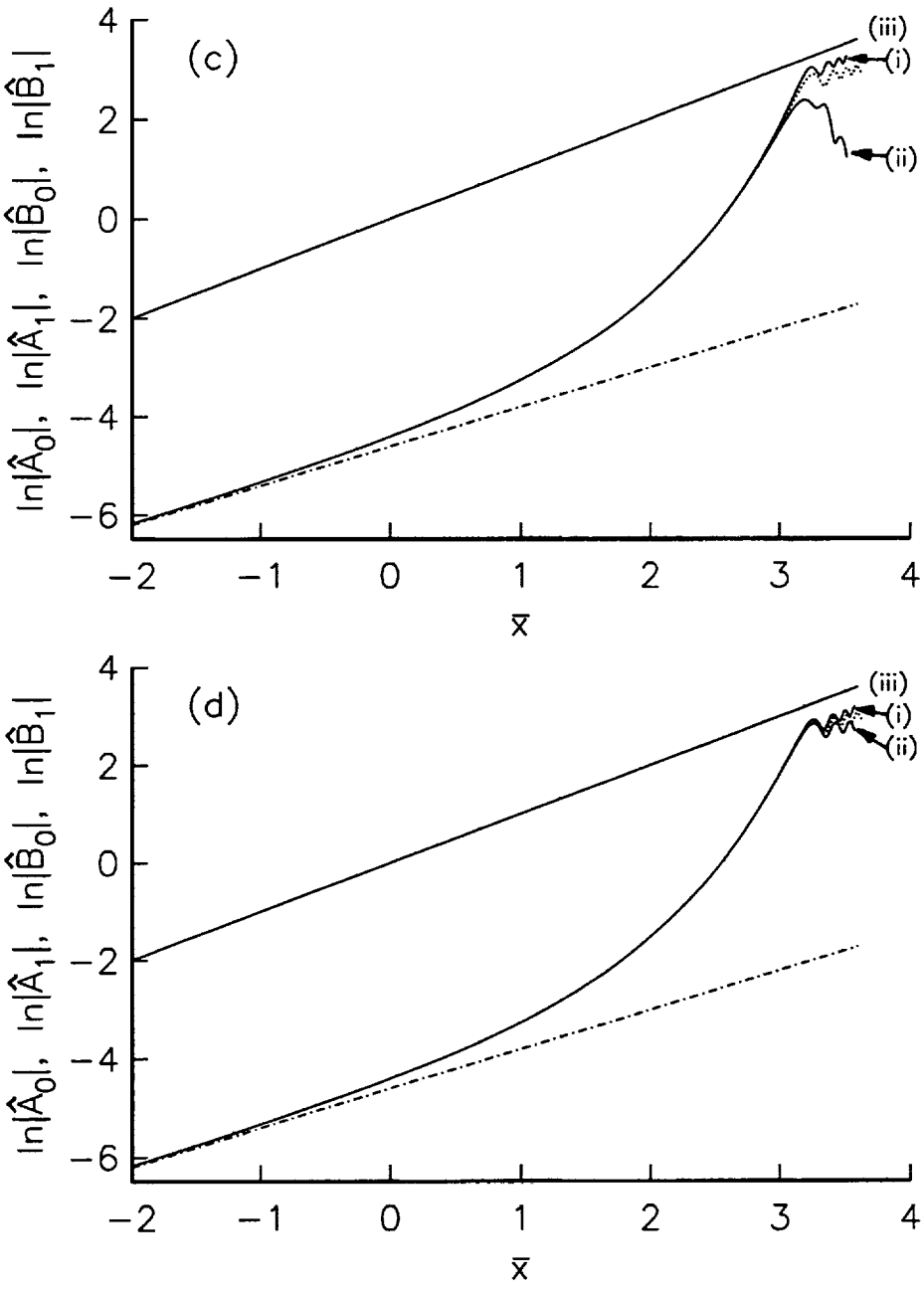

Fig. 1 (c) and (d). See previous page for captions.

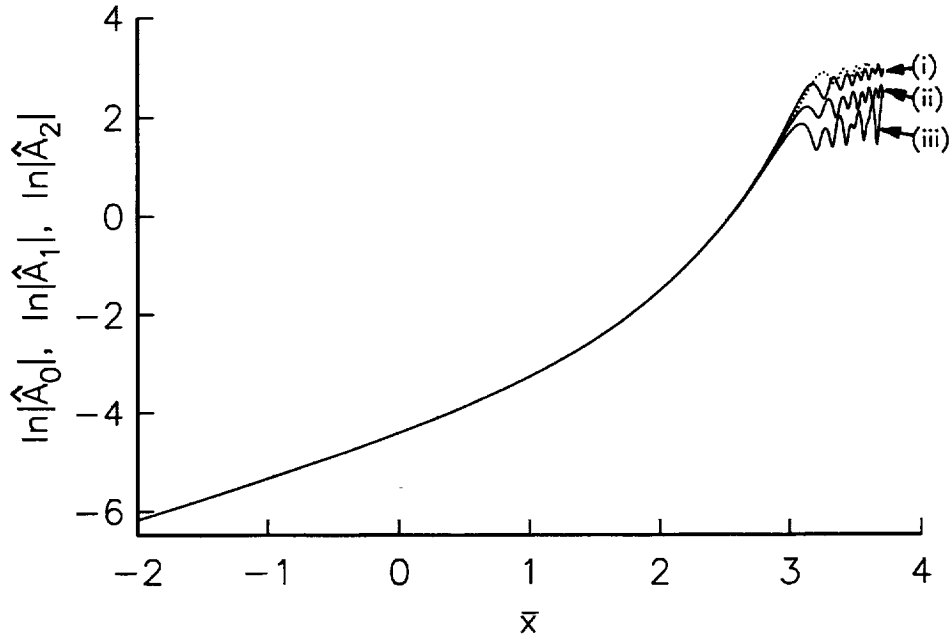

Fig. 2 Quasi-equilibrium interaction between three resonant-triads: $\ln|\hat{A}_0|$, $\ln|\hat{A}_1|$ and $\ln|\hat{A}_2|$ *vs.* $\bar{x}$, curves (i), (ii) and (iii) respectively, when $\bar{\chi} = 5$, $\hat{a}_0 = \hat{a}_1 = \hat{a}_2 = 0.01\exp(i\pi/4)$, $\hat{b}_0 = \hat{b}_1 = \hat{b}_2 = 1$, $\hat{\lambda} = 1$, $\hat{\kappa}_{ob} = 4/5$ and $\hat{\kappa}_{2d} = 1$ (dotted, single resonant-triad interaction)

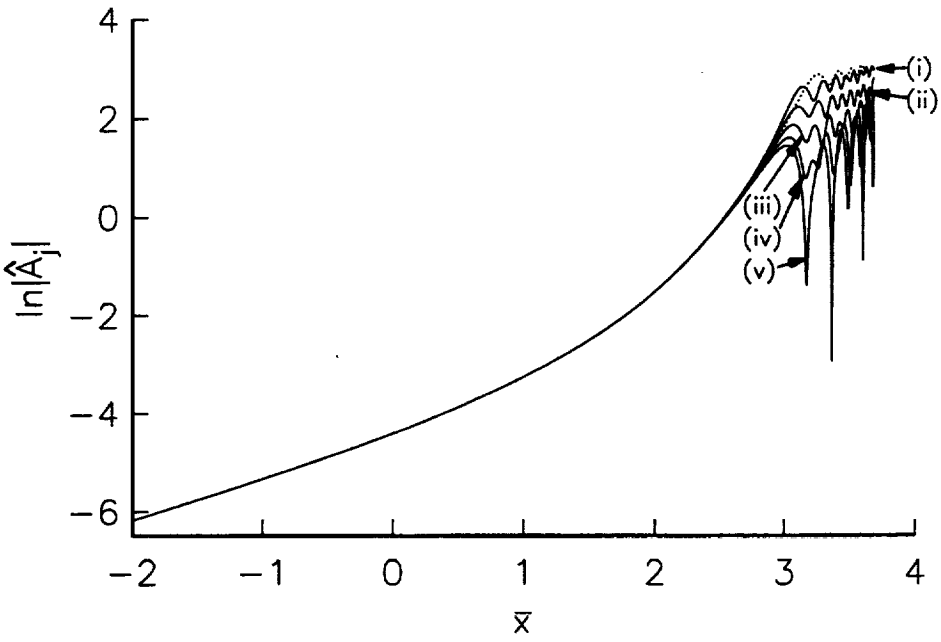

Fig. 3 Quasi-equilibrium interaction between five resonant-triads: $\ln|\hat{A}_0|$, $\ln|\hat{A}_1|$, $\ln|\hat{A}_2|$, $\ln|\hat{A}_3|$ and $\ln|\hat{A}_4|$ *vs.* $\bar{x}$, curves (i) – (v) respectively, when $\bar{\chi} = 5$, $\hat{a}_0 = \hat{a}_1 = \hat{a}_2 = \hat{a}_3 = \hat{a}_4 = 0.01\exp(i\pi/4)$, $\hat{b}_0 = \hat{b}_1 = \hat{b}_2 = \hat{b}_3 = \hat{b}_4 = 1$, $\hat{\lambda} = 1$, $\hat{\kappa}_{ob} = 4/5$ and $\hat{\kappa}_{2d} = 1$ (dotted, single resonant-triad interaction)

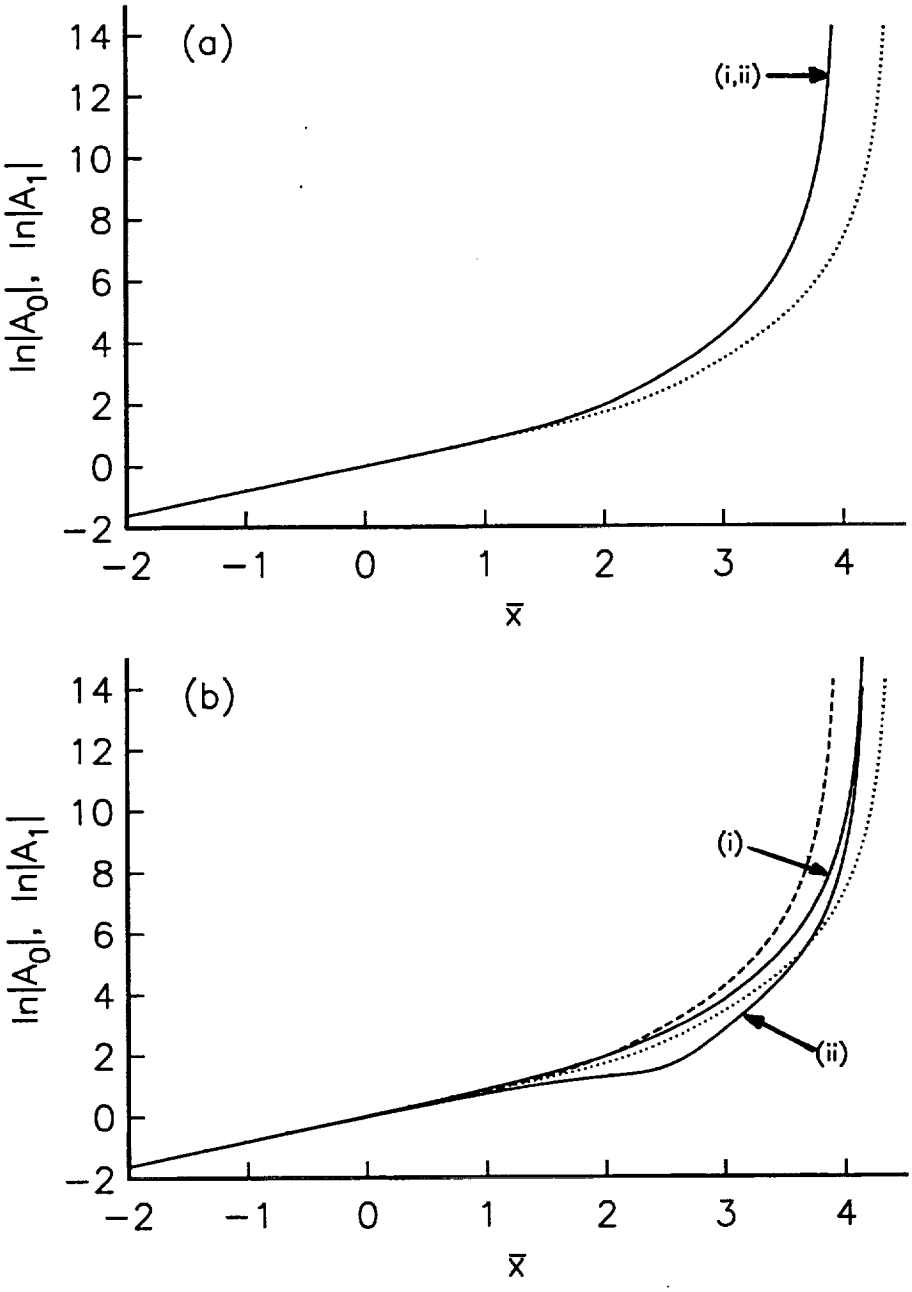

Fig. 4 Non-equilibrium interaction between two pairs of oblique modes: $\ln|A_0|$ and $\ln|A_1|$ *vs.* $\bar{x}$, curves (i) and (ii) respectively, when $\tilde{a}_0 = \tilde{a}_1 = 1$, $\bar{\lambda} = 0$ and (a) $\bar{\chi} = 0$, (b) $\bar{\chi} = 2$, (c) $\bar{\chi} = 5$ and (d) $\bar{\chi} = 100$ (dotted, single-pair interaction; dashed, two-pair interaction with $\bar{\chi} = 0$).

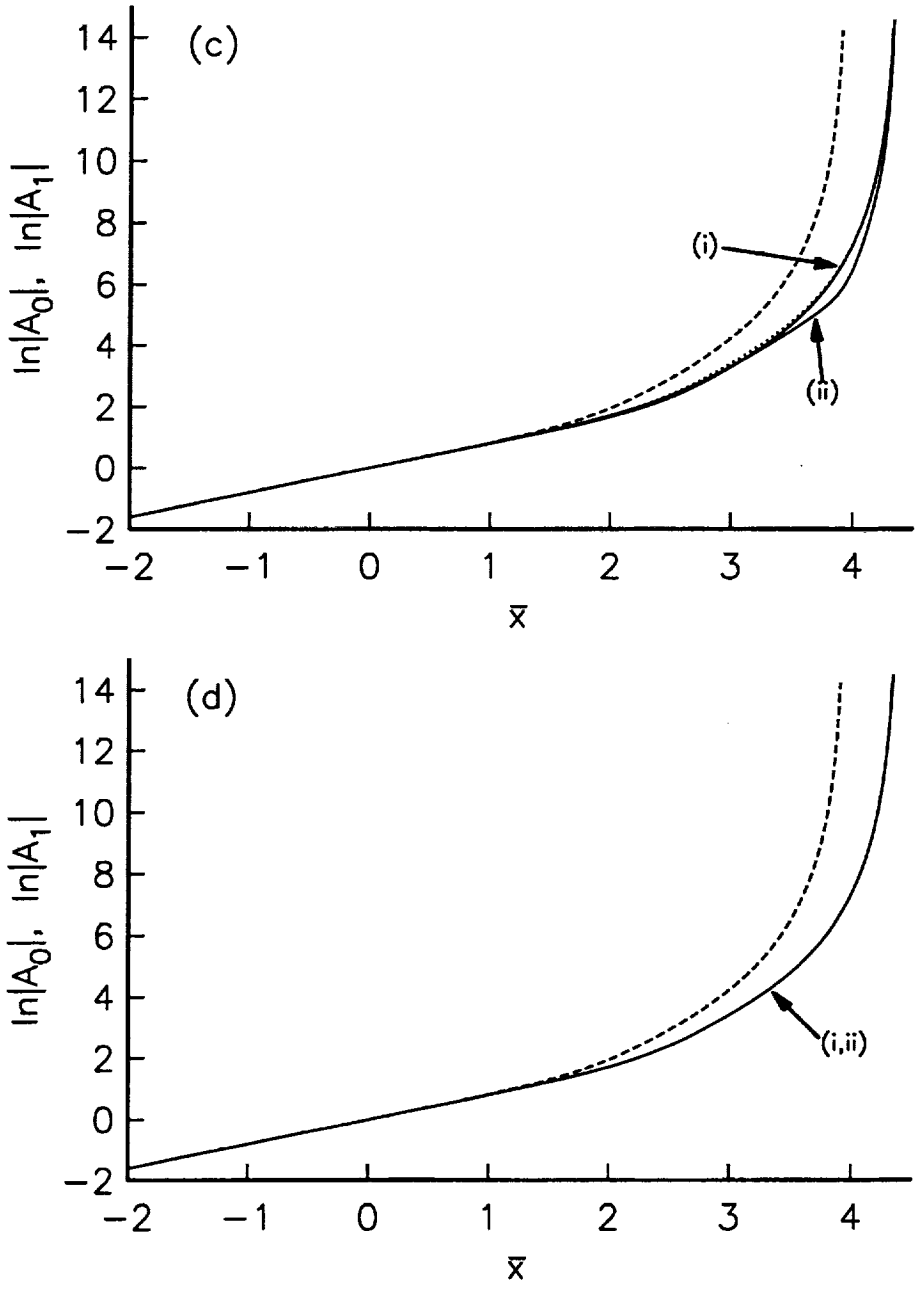

Fig. 4 (c) and (d). See previous page for captions.

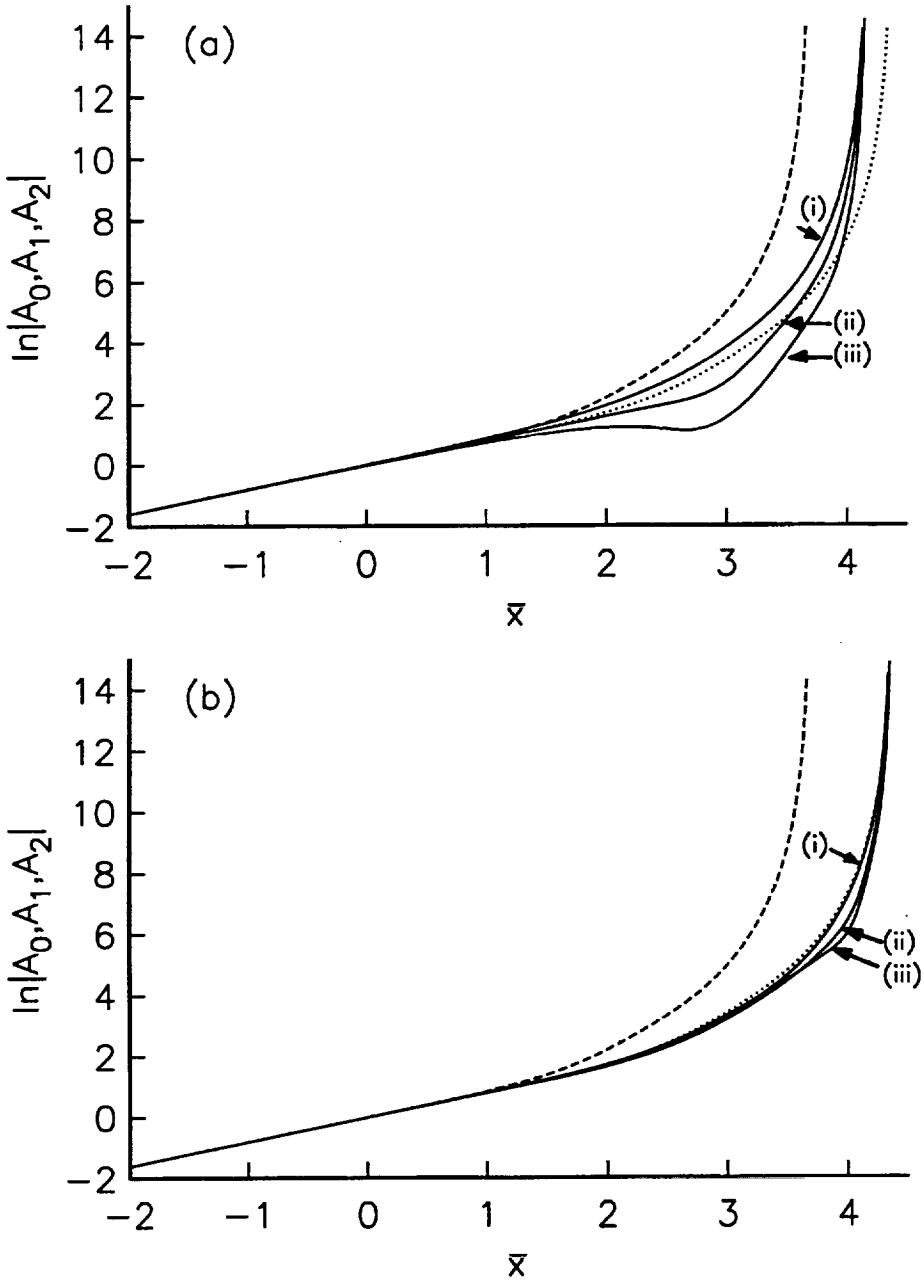

Fig. 5 Non-equilibrium interaction between three pairs of oblique modes: $\ln|A_0|$, $\ln|A_1|$ and $\ln|A_2|$ *vs.* $\bar{x}$, curves (i), (ii) and (iii) respectively, when $\tilde{a}_0 = \tilde{a}_1 = \tilde{a}_2 = 1$, $\bar{\lambda} = 0$ and (a) $\bar{\chi} = 2$ and (b) $\bar{\chi} = 5$ (dotted, single-pair interaction; dashed, three-pair interaction with $\bar{\chi} = 0$).

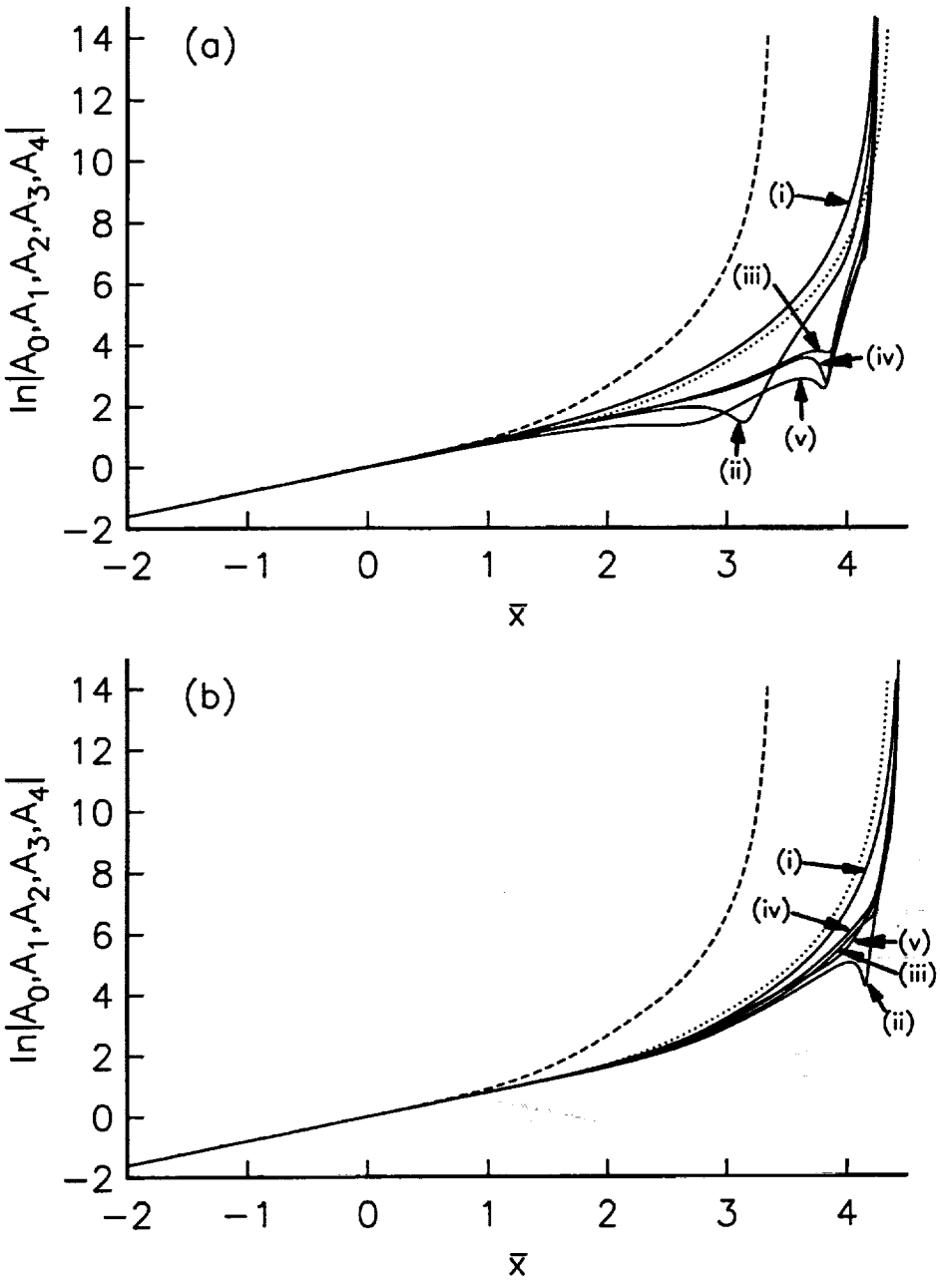

Fig. 6 Non-equilibrium interaction between five pairs of oblique modes: $\ln|A_0|$, $\ln|A_1|$, $\ln|A_2|$, $\ln|A_3|$ and $\ln|A_4|$ *vs.* $\bar{x}$, curves (i) – (v) respectively, when $\tilde{a}_0 = \tilde{a}_1 = \tilde{a}_2 = \tilde{a}_3 = \tilde{a}_4 = 1$, $\bar{\lambda} = 0$ and (a) $\bar{\chi} = 2$ and (b) $\bar{\chi} = 4$ (dotted, single-pair interaction; dashed, five-pair interaction with $\bar{\chi} = 0$).

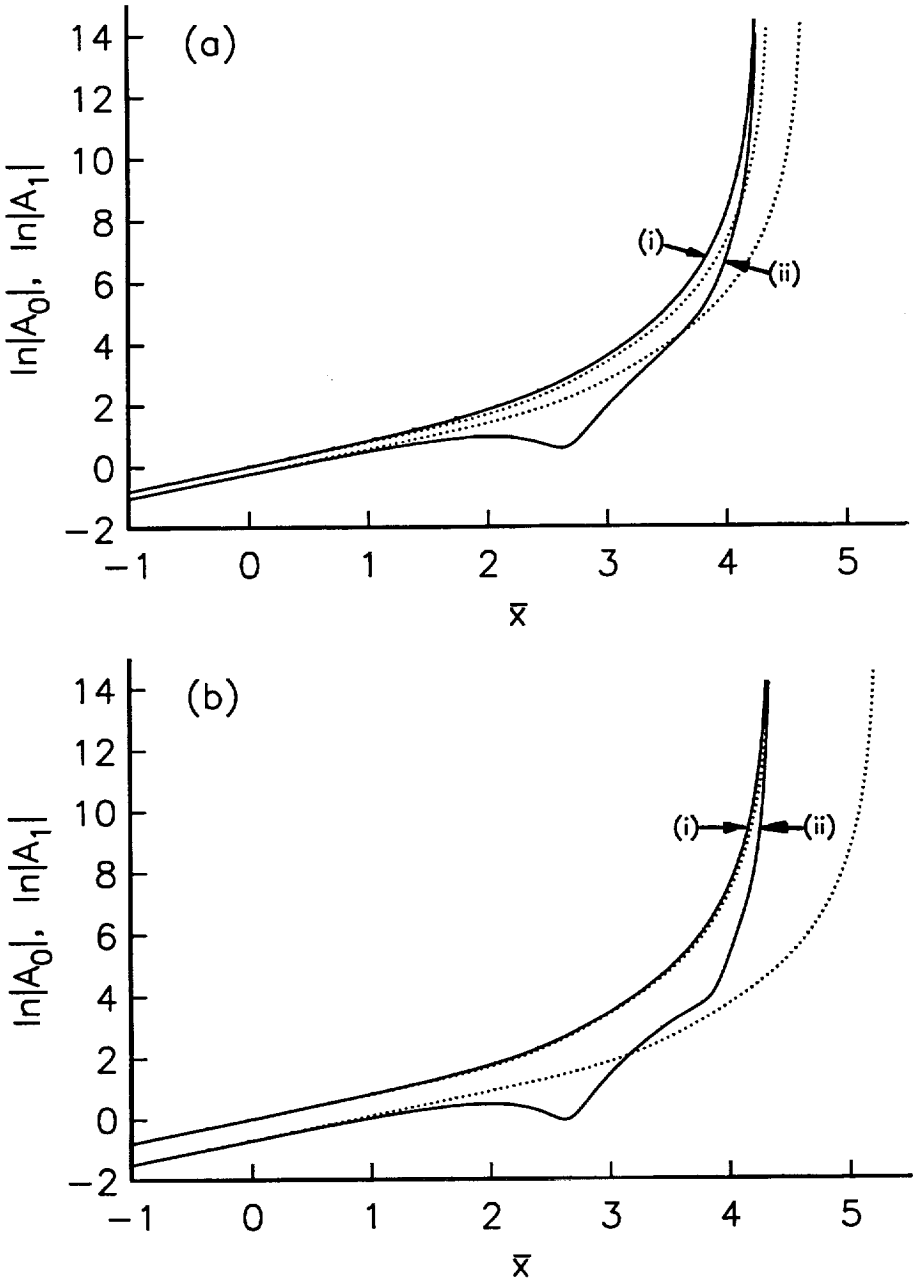

Fig. 7 Non-equilibrium interaction between two pairs of oblique modes: $\ln|A_0|$ and $\ln|A_1|$ *vs.* $\bar{x}$, curves (i) and (ii) respectively, when $\bar{\chi} = 2$, $\bar{\lambda} = 0$, $\tilde{a}_0 = 1$ and (a) $\tilde{a}_1 = 0.8$ and (b) $\tilde{a}_1 = 0.5$ (dotted, single-pair interaction).

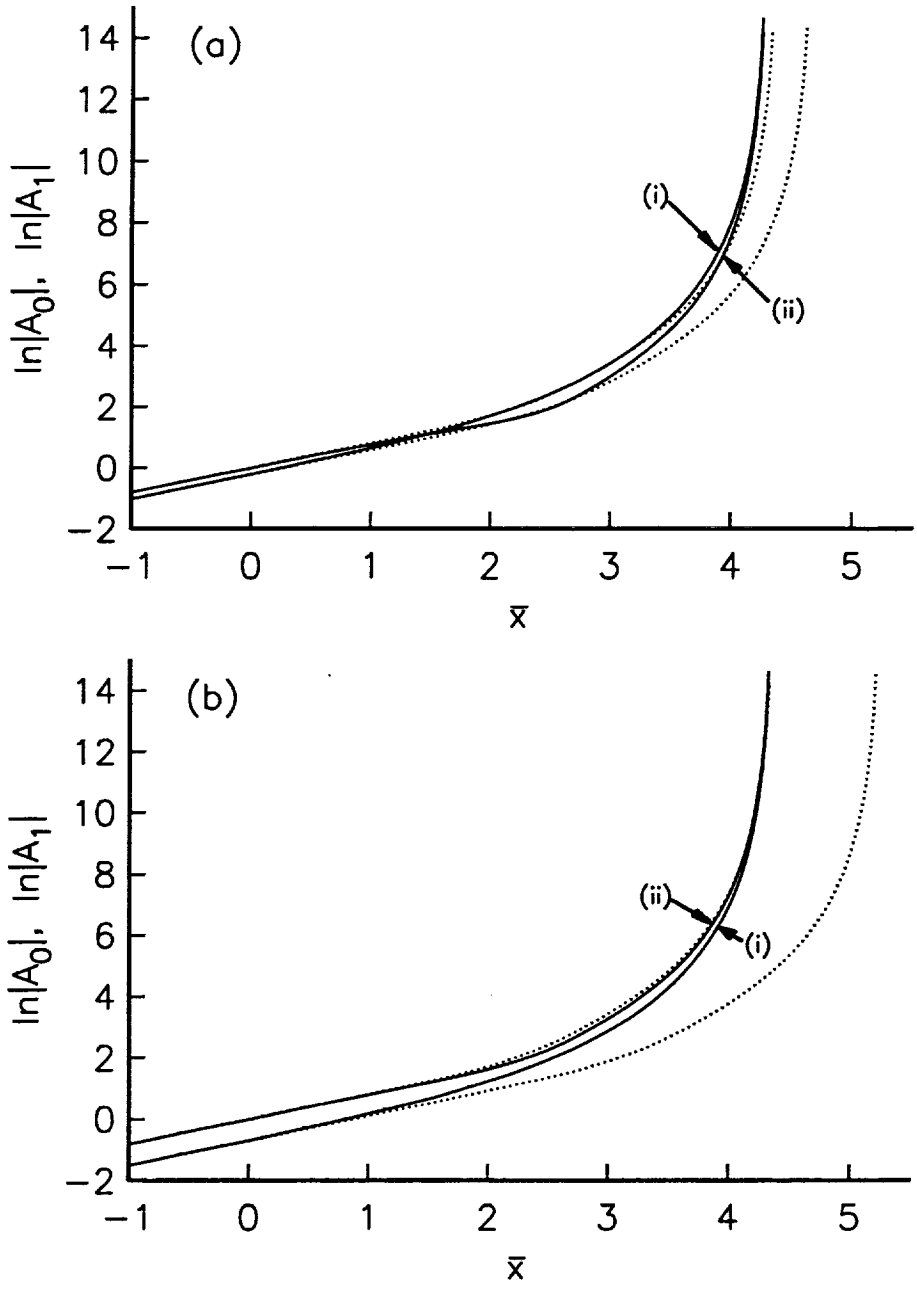

Fig. 8 Non-equilibrium interaction between two pairs of oblique modes: $\ln|A_0|$ and $\ln|A_1|$ *vs.* $\bar{x}$, curves (i) and (ii) respectively, when $\bar{\chi} = 2$, $\bar{\lambda} = 0$, $\tilde{a}_1 = 1$ and (a) $\tilde{a}_0 = 0.8$ and (b) $\tilde{a}_0 = 0.5$ (dotted, single-pair interaction).

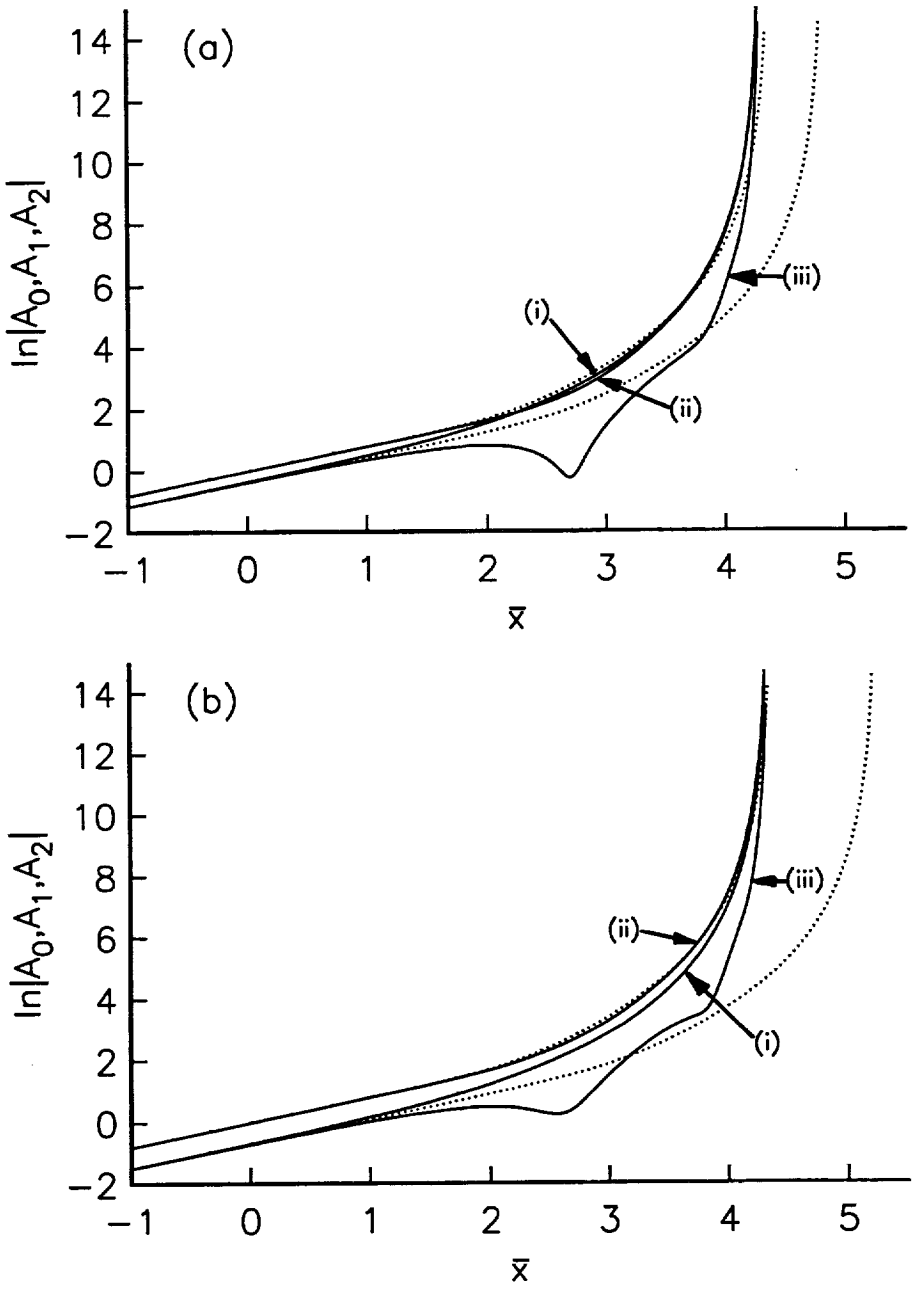

Fig. 9 Non-equilibrium interaction between three pairs of oblique modes: $\ln|A_0|$, $\ln|A_1|$ and $\ln|A_2|$ *vs.* $\bar{x}$, curves (i), (ii) and (iii) respectively, when $\bar{\chi} = 2$, $\bar{\lambda} = 0$, $\tilde{a}_1 = 1$ and (a) $\tilde{a}_0 = \tilde{a}_2 = 0.7$ and (b) $\tilde{a}_0 = \tilde{a}_2 = 0.5$ (dotted, single-pair interaction).

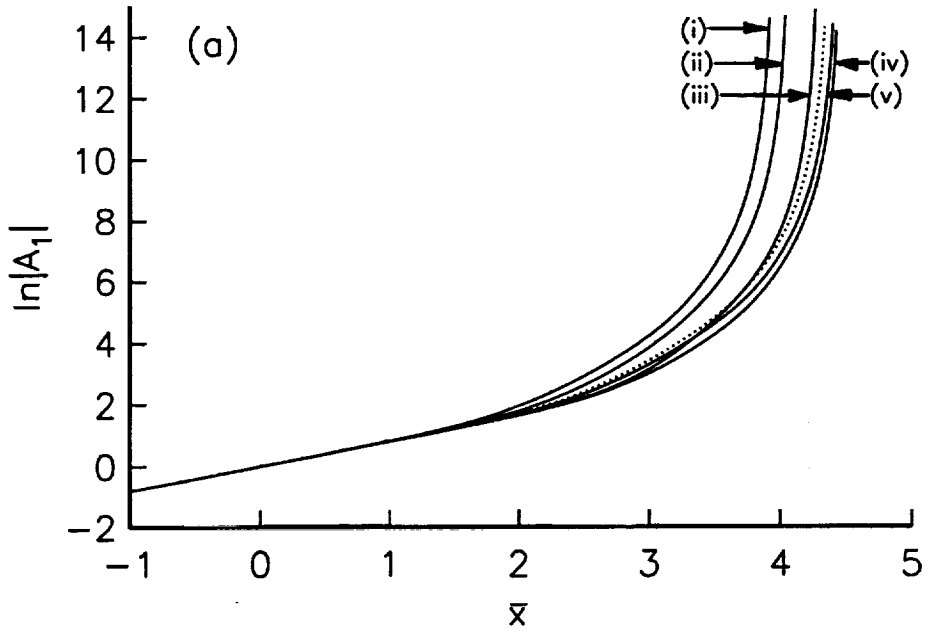

Fig. 10 Non-equilibrium interaction between three pairs of oblique modes: (a) $\ln|A_1|$, (b) $\ln|A_0|$, (c) $|A_0/A_1|$, (d) $\ln|A_2|$ and (e) $|A_2/A_1|$ *vs.* $\bar{x}$ when $\tilde{a}_1 = 1$, $\tilde{a}_0 = \tilde{a}_2 = 0.7$, $\bar{\lambda} = 0$ and $\bar{\chi} = 0$, 1, 2, 3 and 5, curves (i) – (v) respectively (dotted, single-pair interaction).

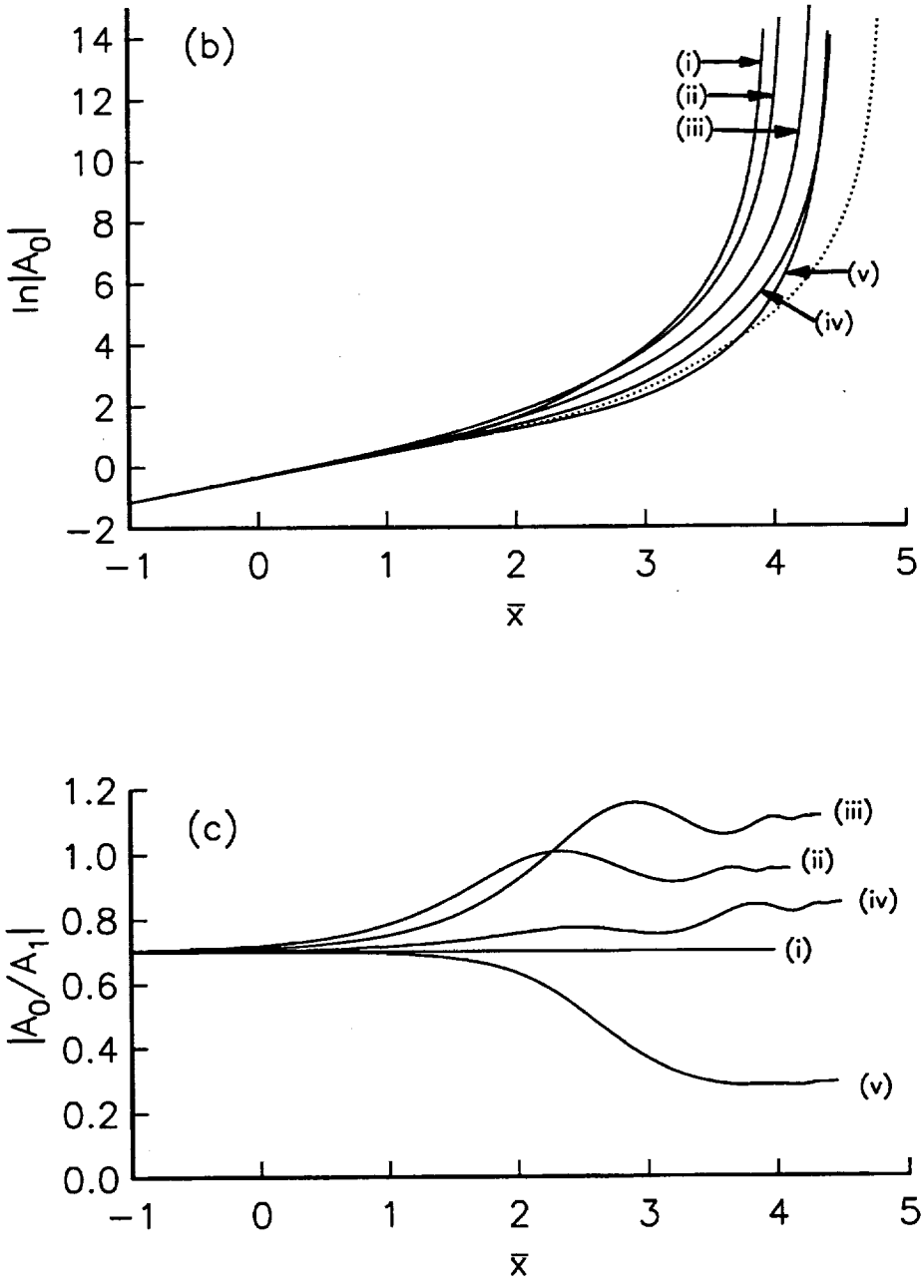

Fig. 10 (b) and (c). See previous page for captions.

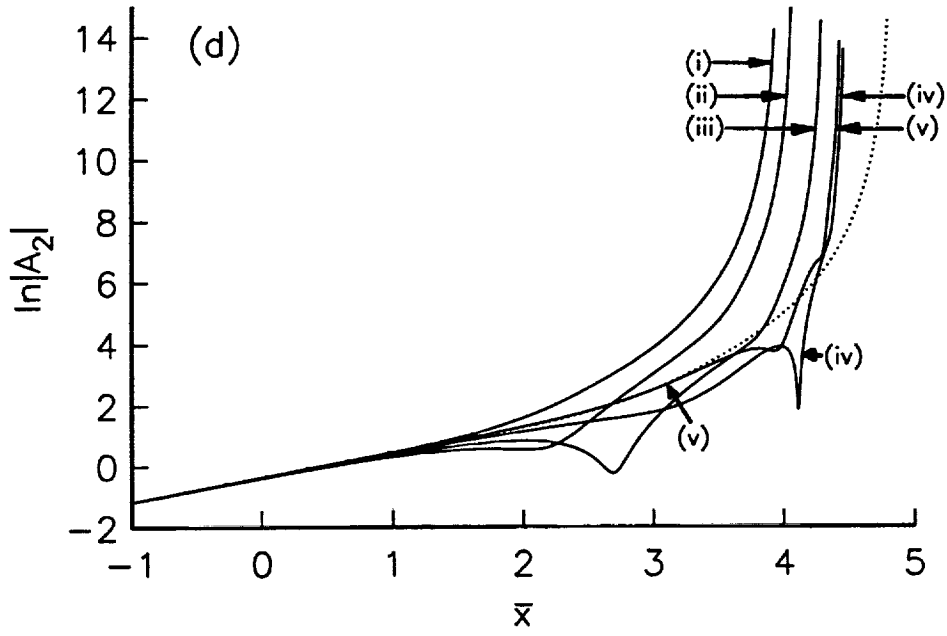

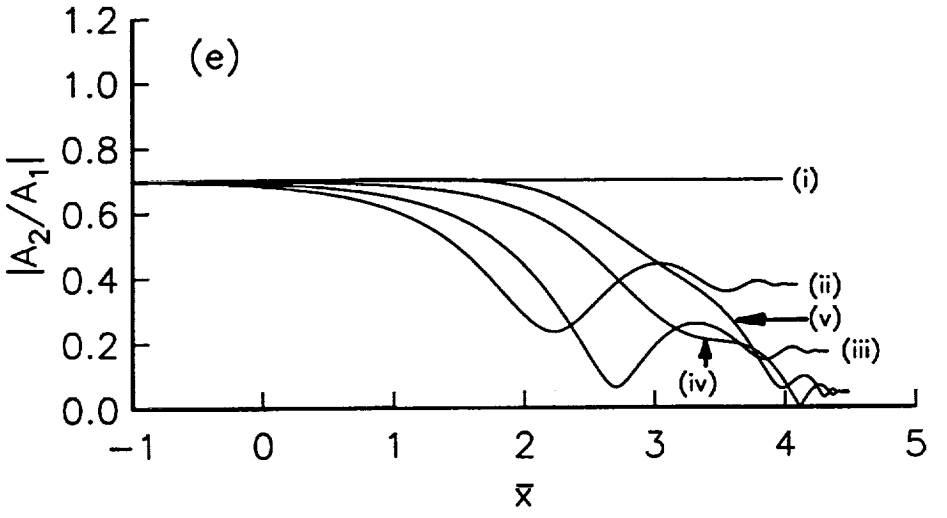

Fig. 10 (d) and (e). See p.70 for captions.

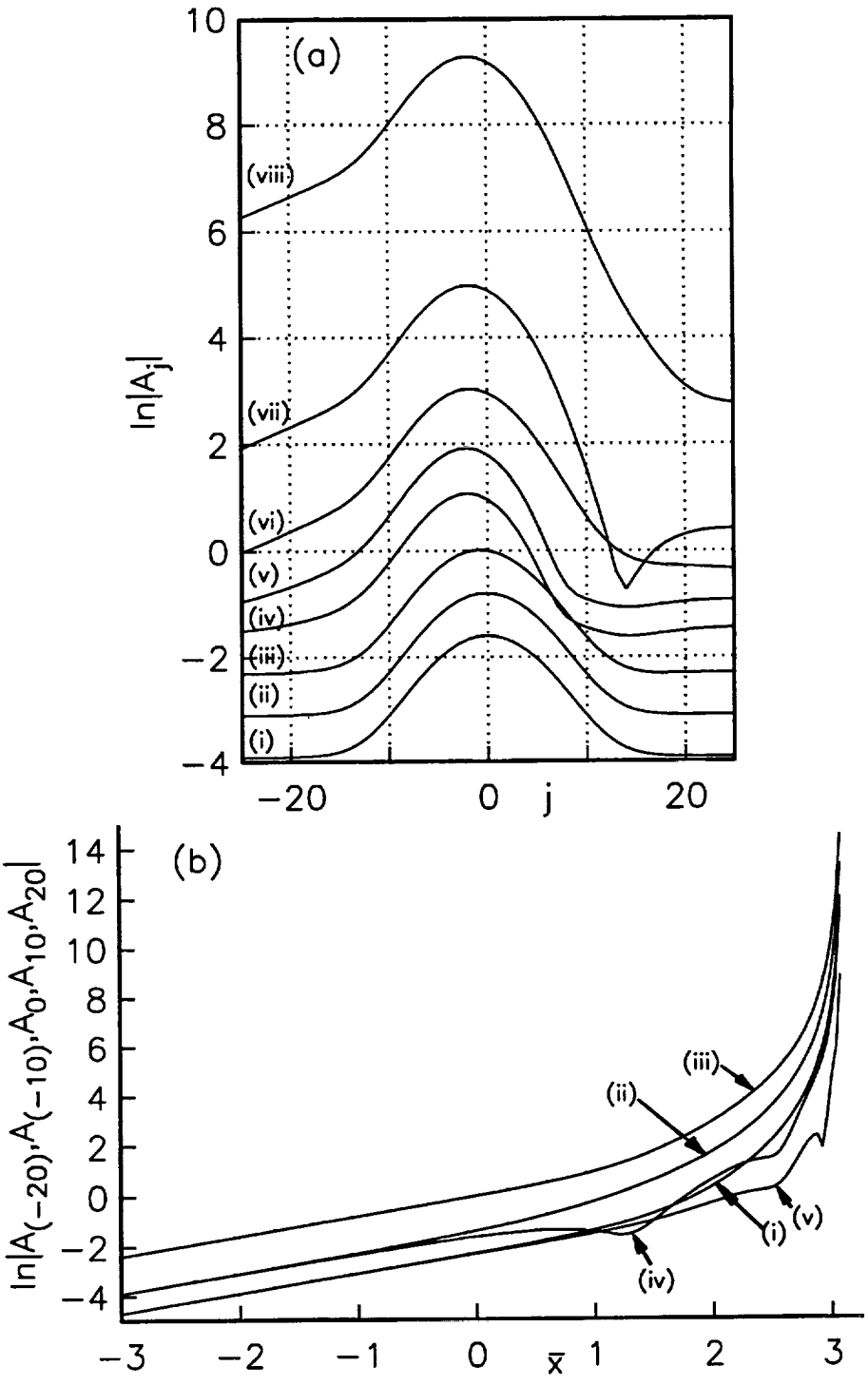

Fig. 11 Non-equilibrium interaction between 51 pairs of oblique modes: (a) $\ln|A_j|$ *vs.* j at $\bar{x} = -2$, -1, 0, 1, 1.52, 2, 2.52 and 2.96, curves (i) – (viii) respectively, and (b) $\ln|A_{(-20)}|$, $\ln|A_{(-10)}|$, $\ln|A_0|$, $\ln|A_{10}|$ and $\ln|A_{20}|$ *vs.* $\bar{x}$, curves (i) – (v), when $\bar{\chi} = 0.2$, $n_1 = 0$ and $\bar{\lambda} = 0$.

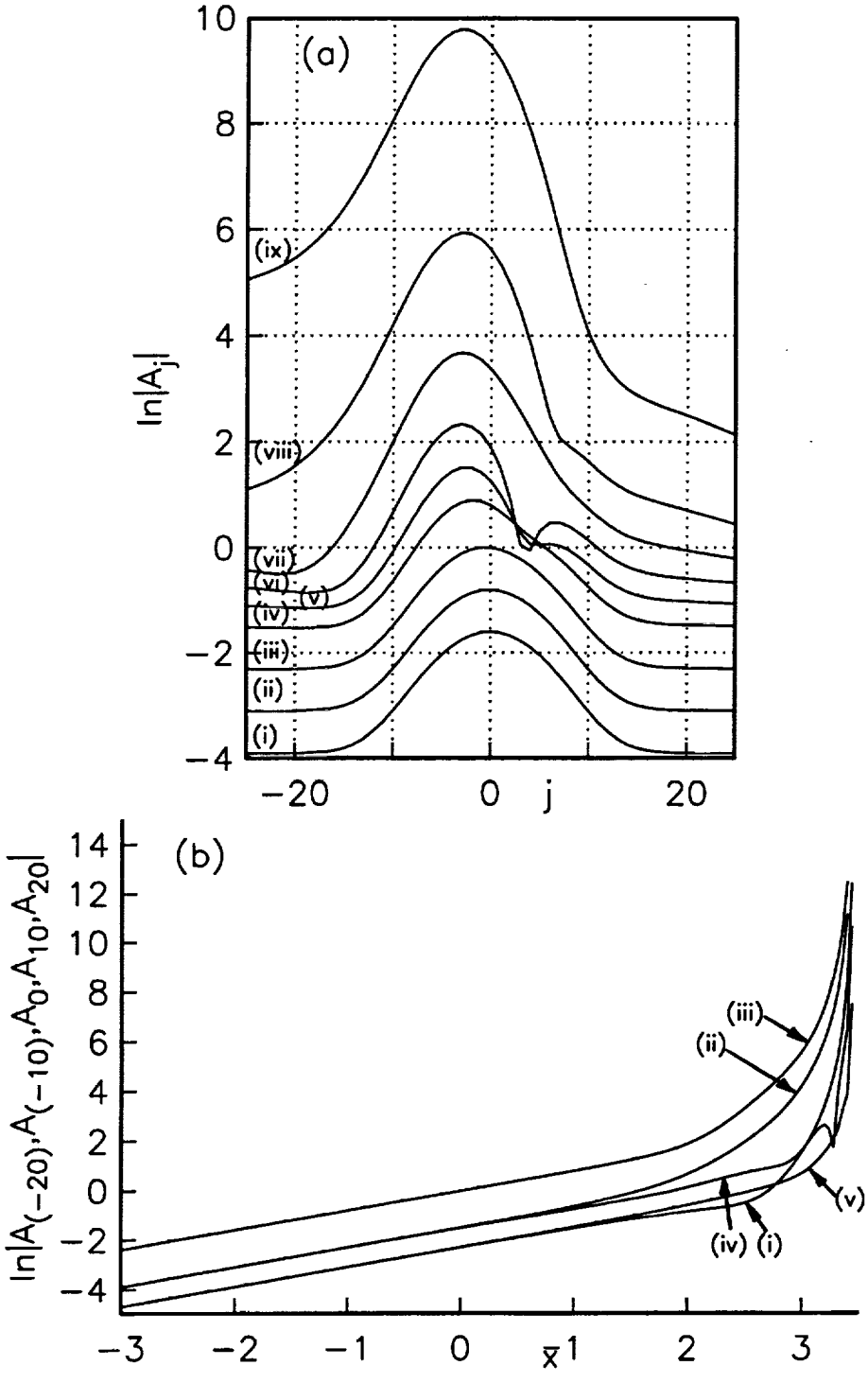

Fig. 12 Non-equilibrium interaction between 51 pairs of oblique modes: (a) $\ln|A_j|$ *vs.* j at $\bar{x} = -2$, -1, 0, 1, 1.52, 2, 2.52, 3 and 3.32, curves (i) – (ix) respectively, and (b) $\ln|A_{(-20)}|$, $\ln|A_{(-10)}|$, $\ln|A_0|$, $\ln|A_{10}|$ and $\ln|A_{20}|$ *vs.* $\bar{x}$, curves (i) – (v), when $\bar{\chi} = 0.5$, $n_1 = 0$ and $\bar{\lambda} = 0$.

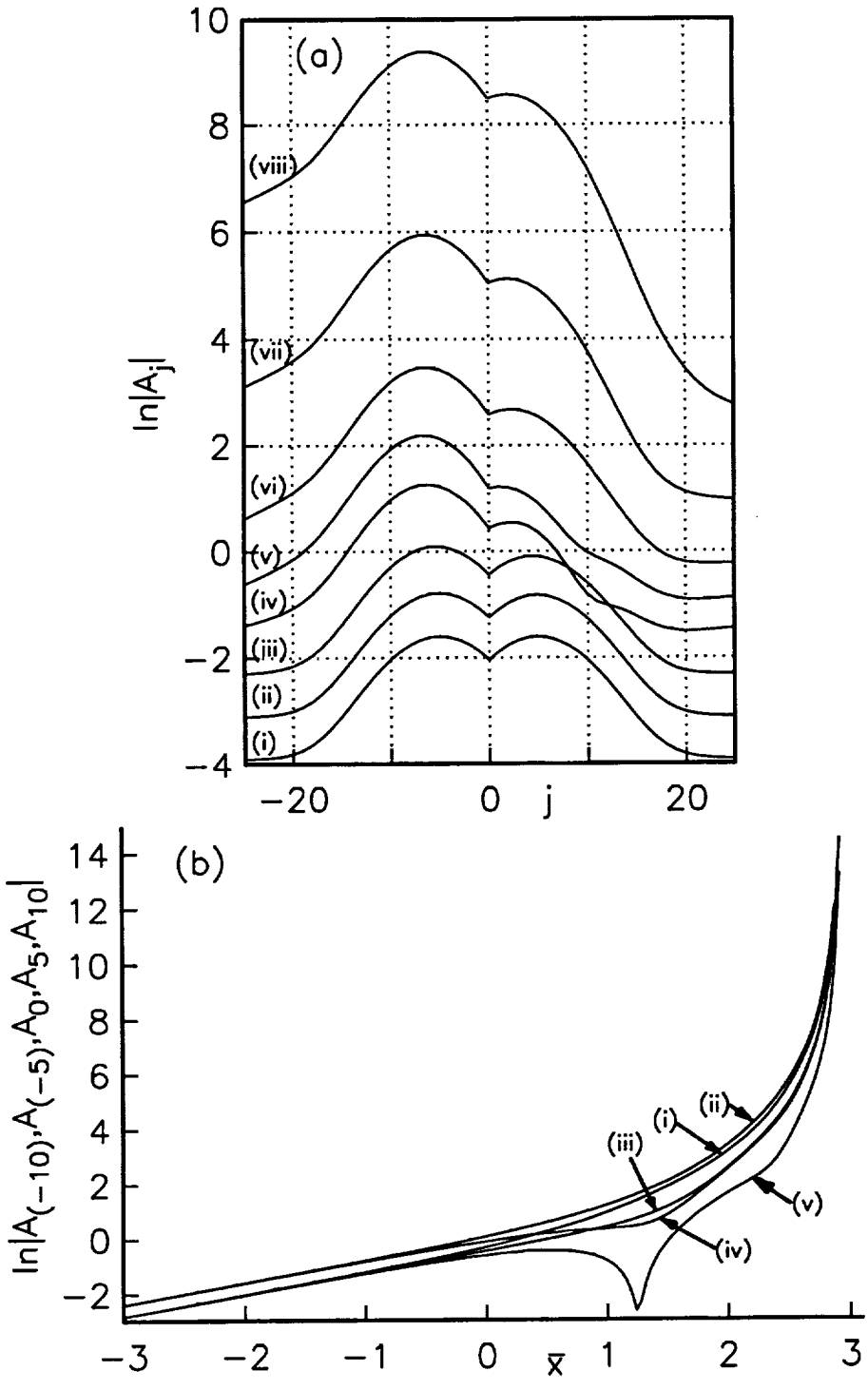

Fig. 13 Non-equilibrium interaction between 51 pairs of oblique modes: (a) $\ln|A_j|$ *vs.* j at $\bar{x} = -2$, -1, 0, 1, 1.52, 2, 2.52 and 2.8, curves (i) – (viii), and (b) $\ln|A_{(-10)}|$, $\ln|A_{(-5)}|$, $\ln|A_0|$, $\ln|A_5|$ and $\ln|A_{10}|$ *vs.* $\bar{x}$, curves (i) – (v), when $\bar{\chi} = 0.2$, $n_1 = 5$, $n_2 = -5$, $C_2 = 1$ and $\bar{\lambda} = 0$.

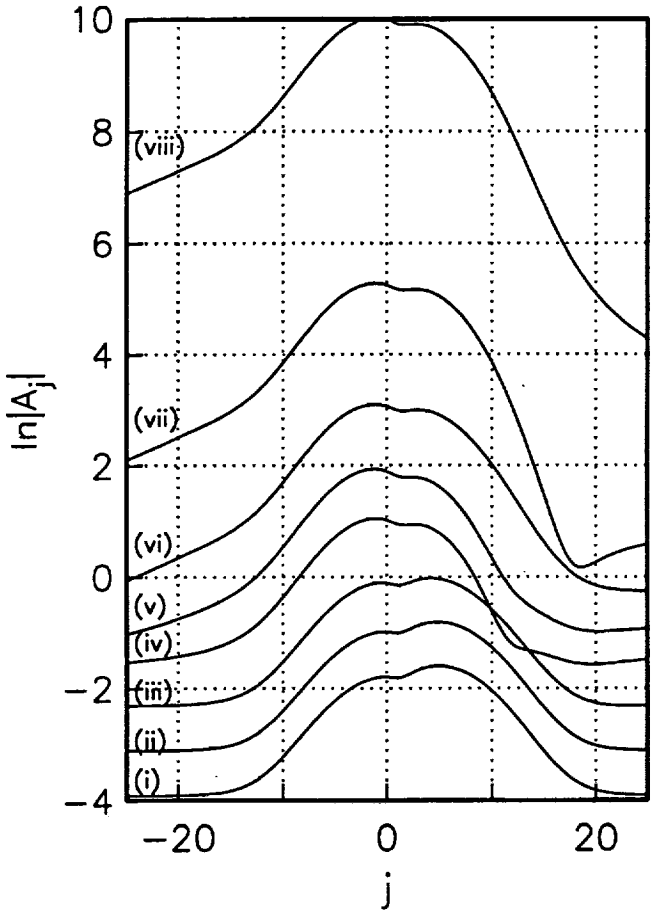

Fig. 14 Non-equilibrium interaction between 51 pairs of oblique modes: $\ln|A_j|$ *vs.* j at $\bar{x} = -2$, -1, 0, 1, 1.52, 2, 2.52 and 2.92, curves (i) – (viii) respectively, when $\bar{\chi} = 0.2$, $n_1 = 5$, $n_2 = 0$, $C_2 = 0.8$ and $\bar{\lambda} = 0$.

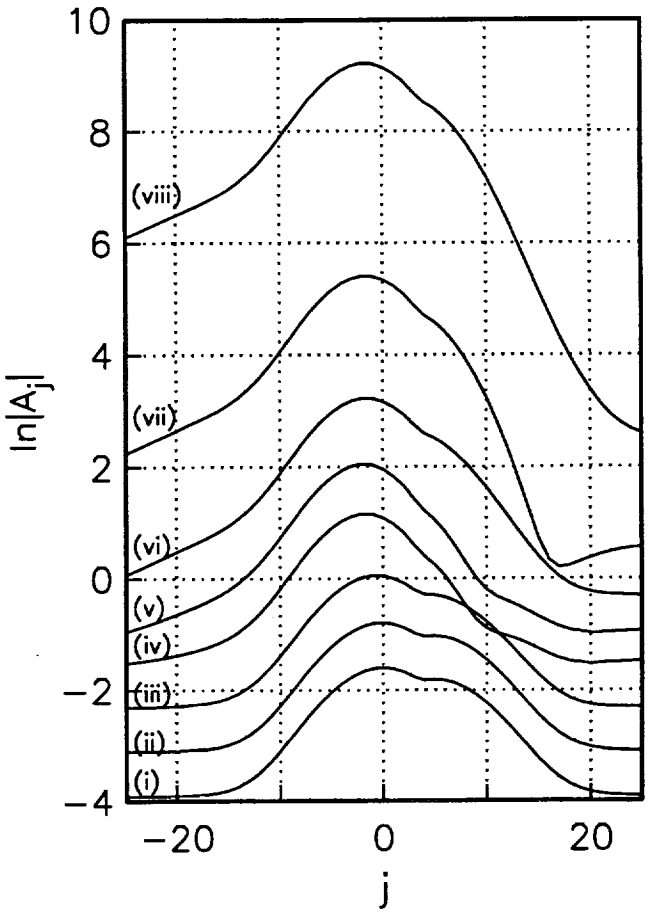

Fig. 15 Non-equilibrium interaction between 51 pairs of oblique modes: $\ln|A_j|$ *vs.* j at $\bar{x} = -2$, -1, 0, 1, 1.52, 2, 2.52 and 2.88, curves (i) – (viii) respectively, when $\bar{\chi} = 0.2$, $n_1 = 0$, $n_2 = 5$, $C_2 = 0.8$ and $\bar{\lambda} = 0$.

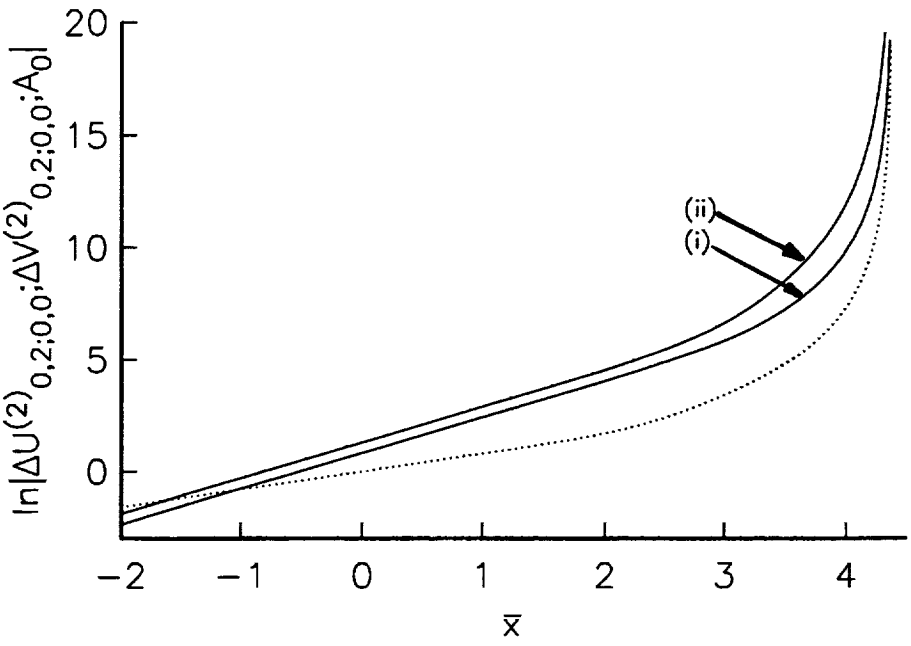

Fig. 16 Non-equilibrium interaction between single pair of oblique modes: $\ln|\Delta U^{(2)}_{0,2;0,0}|$ and $\ln|\Delta V^{(2)}_{0,2;0,0}|$ *vs.* $\bar{x}$, curves (i) and (ii) respectively, when $\tilde{a}_0 = 1$ and $\bar{\lambda} = 0$. (dotted, $\ln|A_0|$).

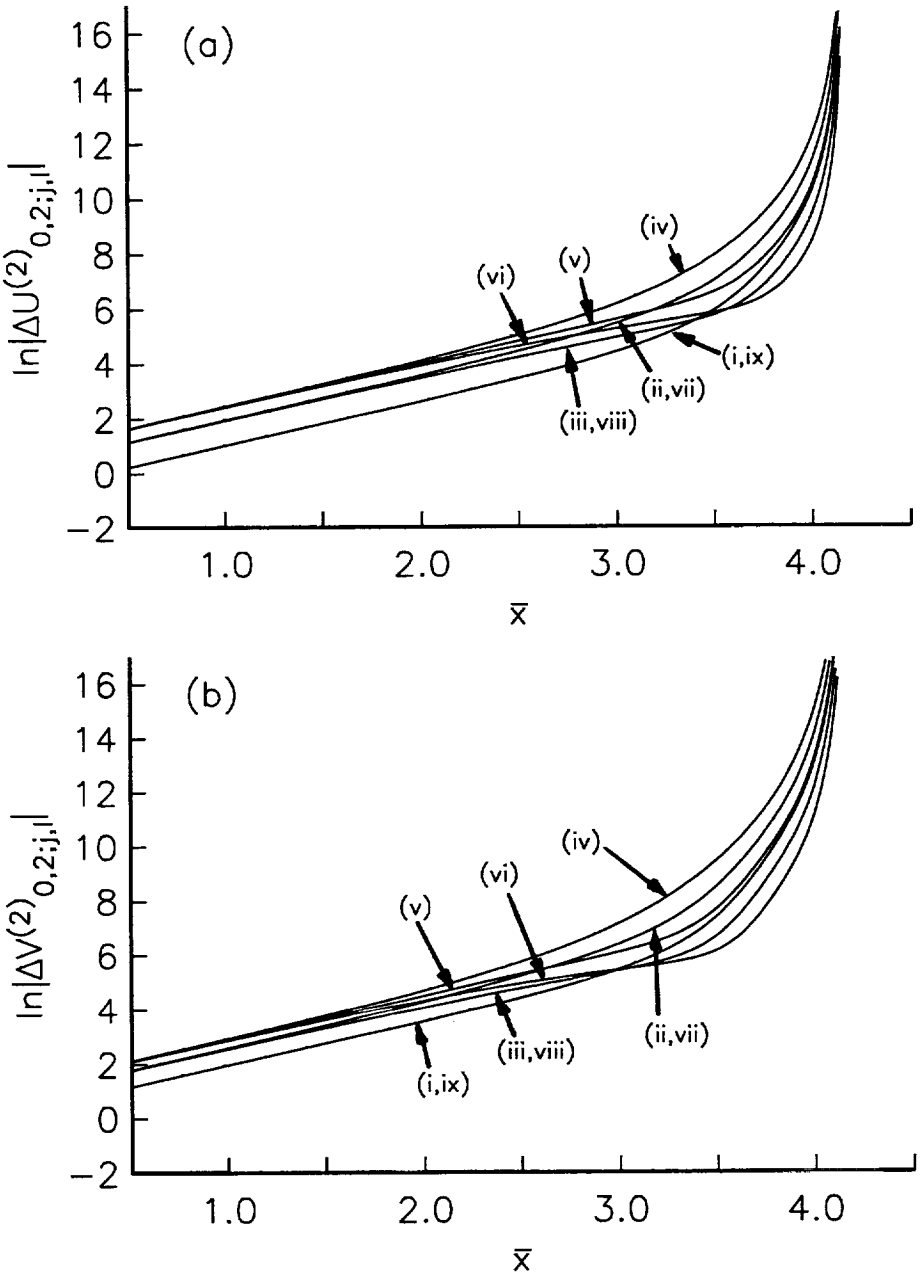

Fig. 17 Non-equilibrium interaction between three pairs of oblique modes: (a) $\ln|\Delta U^{(2)}_{0,2;j,\ell}|$ and (b) $\ln|\Delta V^{(2)}_{0,2;j,\ell}|$ *vs.* $\bar{x}$ when $\tilde{a}_0 = \tilde{a}_1 = \tilde{a}_2 = 1$, $\bar{\lambda} = 0$ and $\bar{\chi} = 2$. (j,ℓ) = (-2,2), (-1,1), (-1,2), (0,0), (0,1), (0,2), (1,0), (1,1) and (2,0), curves (i) - (ix) respectively.

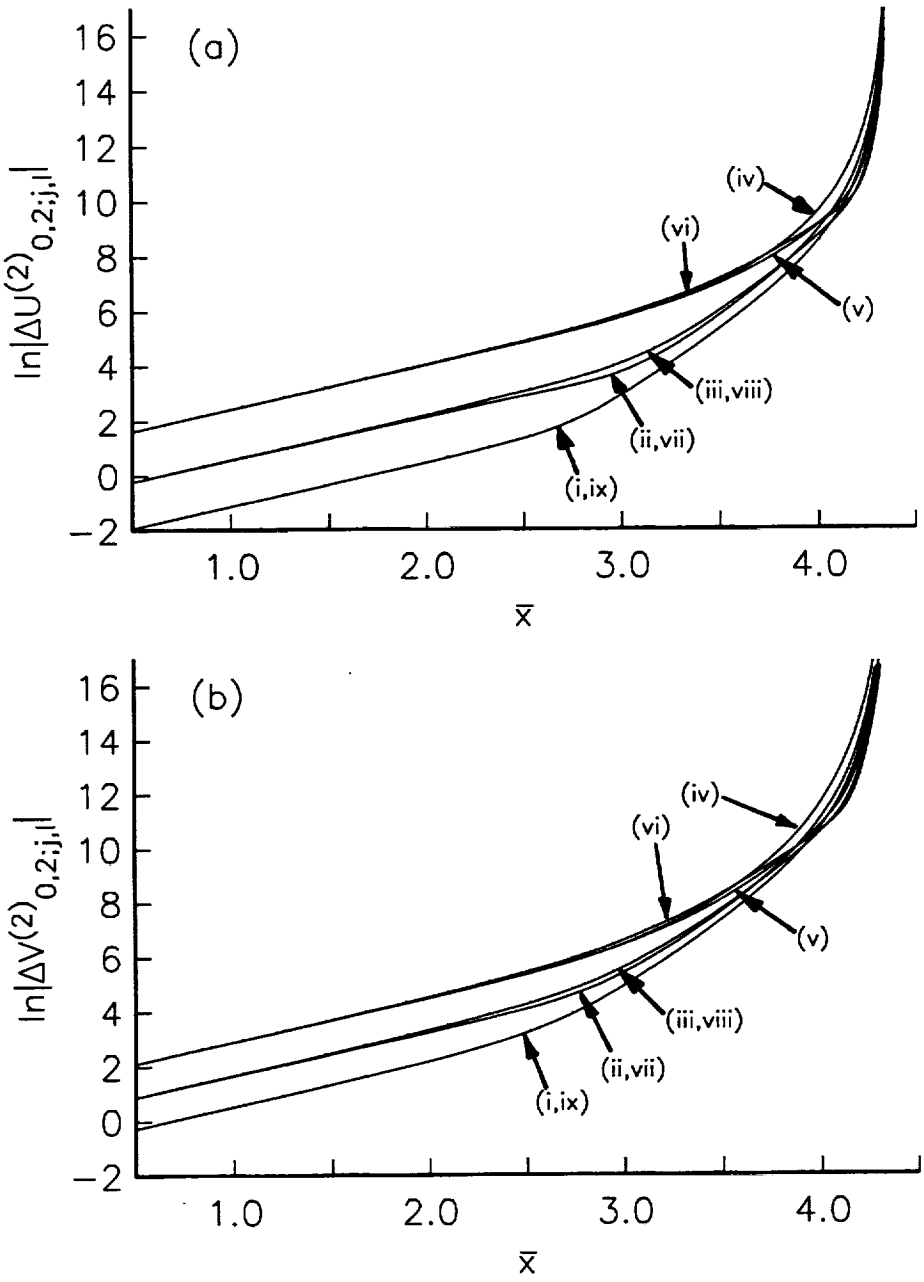

Fig. 18 Non-equilibrium interaction between three pairs of oblique modes: (a) $\ln|\Delta U^{(2)}_{0,2;j,\ell}|$ and (b) $\ln|\Delta V^{(2)}_{0,2;j,\ell}|$ *vs.* $\bar{x}$ when $\tilde{a}_0 = \tilde{a}_1 = \tilde{a}_2 = 1$, $\bar{\lambda} = 0$ and $\bar{\chi} = 5$. (j,ℓ) = (-2,2), (-1,1), (-1,2), (0,0), (0,1), (0,2), (1,0), (1,1) and (2,0), curves (i) – (ix) respectively.

REPORT DOCUMENTATION PAGE

Form Approved
OMB No. 0704-0188

1. AGENCY USE ONLY (*Leave blank*)	2. REPORT DATE	3. REPORT TYPE AND DATES COVERED
	October 1998	Final Contractor Report

4. TITLE AND SUBTITLE

Nonlinear Interaction of Detuned Instability Waves in Boundary–Layer Transition Amplitude Equations

5. FUNDING NUMBERS

WU–538–03–11–00
NAS3–98008

6. AUTHOR(S)

Sang Soo Lee

7. PERFORMING ORGANIZATION NAME(S) AND ADDRESS(ES)

Dynacs Engineering Company, Inc.
2001 Aerospace Parkway
Brook Park, Ohio 44142

8. PERFORMING ORGANIZATION REPORT NUMBER

E–11416

9. SPONSORING/MONITORING AGENCY NAME(S) AND ADDRESS(ES)

National Aeronautics and Space Administration
Lewis Research Center
Cleveland, Ohio 44135–3191

10. SPONSORING/MONITORING AGENCY REPORT NUMBER

NASA CR—1998-208679

11. SUPPLEMENTARY NOTES

Project manager, Dennis L. Huff, Structures and Acoustics Division, NASA Lewis Research Center, organization code 5940, (216) 433–3913.

12a. DISTRIBUTION/AVAILABILITY STATEMENT

Unclassified - Unlimited
Subject Category: 71 Distribution: Nonstandard

This publication is available from the NASA Center for AeroSpace Information, (301) 621–0390.

12b. DISTRIBUTION CODE

13. ABSTRACT (*Maximum 200 words*)

The non-equilibrium critical-layer analysis of a system of frequency-detuned resonant-triads is presented. In this part of the analysis, the system of partial differential critical-layer equations derived in Part 1 is solved analytically to yield the amplitude equations which are analyzed using a combination of asymptotic and numerical methods. Numerical solutions of the inviscid non-equilibrium oblique-mode amplitude equations show that the frequency-detuned self-interaction enhances the growth of the lower-frequency oblique modes more than the higher-frequency ones. All amplitudes become singular at the same finite downstream position. The frequency detuning delays the occurrence of the singularity. The spanwise-periodic mean-flow distortion and low-frequency nonlinear modes are generated by the critical-layer interaction between frequency-detuned oblique modes. The nonlinear mean flow and higher harmonics as well as the primary instabilities become as large as the base mean flow in the inviscid wall layer in the downstream region where the distance from the singularity is of the order of the wavelength scale.

14. SUBJECT TERMS

Nonlinear instability; Boundary layer; Transition; Resonant–triad

15. NUMBER OF PAGES

86

16. PRICE CODE

A05

17. SECURITY CLASSIFICATION OF REPORT	18. SECURITY CLASSIFICATION OF THIS PAGE	19. SECURITY CLASSIFICATION OF ABSTRACT	20. LIMITATION OF ABSTRACT
Unclassified	Unclassified	Unclassified	